Electronic and Transport Signatures of SnTe Nanowires

A thesis submitted to the Delft University of Technology in partial fulfillment of the requirements for the degree of Master of Science in Applied Physics

Author:
Thomas Bredewoud
Student number:
4924673

Supervisors
Dr. Michael Wimmer
Sebastian Miles

Committee members
Dr. Michael Wimmer
Dr. Anton Akhmerov
Dr. Maximilian Rimbach-Russ

June 15, 2025

TU Delft

Quantum Tinkerer

Abstract

Topological crystalline insulators (TCI's) are materials that host robust gapless states protected by crystalline symmetries. In this thesis, SnTe is studied using a tight-binding model. We focus on the electronic and transport properties of nanowires with (100) and (110) surface terminations, in the mesoscopic regime. In these configurations, gapless states are characterized as robust (against finite-size effects, step edges, and hinge rounding) spin-polarized surface and hinge states with corner charge, demonstrating intrinsic higher-order-topological behavior. We also investigate a mixed nanowire configuration having both (001) and (101) surface terminations, which displays extrinsic topological behavior.

Transport simulations reveal distinct conductance signatures for each surface termination. Nanowires with (100) terminations host surface states extending along the nanowire's perimeter, showing Aharonov-Bohm oscillations in longitudinal transport. Nanowires with a (110) terminations host confined surface states, giving rise to resonant tunneling conductance signatures for transverse transport.

These findings contribute to the general understanding of TCI nanowires, specifically the relationship between surface termination, gapless states, and transport signatures, providing valuable insights for the future design of TCI-based electronic devices.

Acknowledgments

I would like to express my gratitude to the entire Quantum Tinkerer group for giving me this opportunity. Their supportive environment greatly contributed to the thesis. Especially, my thesis supervisor Michael Wimmer, for guiding me throughout this research. I also want to thank my daily supervisor, Sebastian Miles, who always helped me with my questions. I would like to thank Dániel Varjas for his valuable insights, without which this thesis would have looked differently. Finally, I would like to thank my family and friends for all their support throughout my studies.

Contents

Acronyms

SnTe	Tin telluride
PbTe	Lead telluride
FCC	Face-centered cubic
TB	Tight-binding
TI	Topological insulator
TCI	Topological crystalline insulator
HOTI	Higher-order topological insulator
BZ	Brillouin zone
1DBZ	One-dimensional Brillouin zone
2DBZ	Two-dimensional Brillouin zone
3DBZ	Three-dimensional Brillouin zone
AB	Aharonov–Bohm
HSP	High-symmetry point
TR	Time-reversal
TRIM	Time-reversal invariant momenta
SOC	Spin–orbit coupling
DOF	Degrees of freedom
DOS	Density of states

1 Introduction

In the last decades, topological materials have emerged as a frontier in condensed matter physics, driven by their unique electronic properties. These unique properties give rise to promising applications in quantum computing, spintronics and low-power electronics [1].

Topological insulators are a subclass of topological materials, characterized by an insulating bulk and robust conductive surface states, protected by the topology of the material. Among these, topological crystalline insulators (TCI's) rely on crystalline symmetries protecting the topology [2]. SnTe, which is narrow-gap IV–VI semiconductor, is the first material realization of a TCI predicted [3] and experimentally observed [4]. SnTe has also been proposed as a higher-order topological insulator (HOTI) [5], in which gapless surface states lose there two-dimensional character, becoming one-dimensional hinge states, localized at the edges of the nanowire. A recent study confirmed SnTe nanowires host these hinge states, while also hosting confined and extended Dirac surface states [6], depending on the wire's surface termination.

The experimental interest for SnTe is mostly because combining a SnTe nanowire with superconductivity, gives rise to Majorana modes at the ends of the nanowire [7]. These modes can be used to create a topologically protected qubit. An advantage of this type of qubit, is its robustness and fault tolerance, which are necessary when scaling the number of qubits in quantum computing.

This thesis aims to contribute to the theoretical understanding of SnTe nanowires, which is an important step towards realizing these applications. We focus on how the electronic and transport properties of hinge and surface states depend on the nanowire geometry and surface termination.

A tight-binding approach will be used to model SnTe for different nanowire configurations. We investigate how properties of surface and hinge states in cross sections of a TCI (specifically SnTe) depend on surface termination. We analyze their band structures, the emergence of gapless states, the flux response, the influence of strain, spin polarization and corner charge. Imperfections like step edges and hinge rounding will also be discussed.

We also explore quantum transport in these nanowire structures, which is a novel topic, not addressed in literature. We examine transport in both the longitudinal direction (along the nanowire axis) and the transverse direction (perpendicular to the nanowire axis). By threading the nanowires with a magnetic flux, we examine the presence of Aharonov-Bohm oscillations. We aim to identify distinct transport signatures of the gapless states propagating in these structures.

The thesis is structured as follows: Chapter 2 provides theoretical background, Chapter 3 describes the methodology, including the tight-binding model and its validation against bulk and slab geometries. Chapter 4 covers the electronic properties of the nanowire configurations. Chapter 5 presents the quantum transport results in the longitudinal and transverse directions. Chapter 6 gives the conclusion and Chapter 7 the outlook discussing future research directions.

2 Theory

In this section, we present the theoretical background necessary to describe the electronic and transport properties of SnTe nanowires. We begin by outlining the crystal structure and reciprocal space of SnTe, followed by a discussion of the tight-binding (TB) model used to capture its electronic behavior. Next, we introduce some basic concepts in topology, including the notion of a topological crystalline insulator, the role of symmetries, and bulk-boundary correspondence. Finally, we discuss the scattering matrix formalism, which plays a central role in our quantum transport calculations.

2.1 Crystal structures

This section covers the mathematical description of crystal structures. We demonstrate that the physics of a crystal can be described using its band structure, which can be numerically evaluated using the tight-binding approach.

2.1.1 Band structures

A crystal can be described by a set of repeated points, known as a lattice. In real space the full lattice is described by $\mathbf{R} = n_1\mathbf{a_1} + n_2\mathbf{a_2} + n_3\mathbf{a_3}$, where $\{\mathbf{a}_1, \mathbf{a}_2, \mathbf{a}_3\}$ are the primitive lattice vectors constructing the unit cell (n_1, n_2, $n_3 \in \mathbb{N}$). This is known as a Bravais lattice, which is generated by a set of discrete translation operations. SnTe has a rock-salt crystal structure, consisting of two interpenetrating face-centered cubic (FCC) lattices, depicted in Figure 2.1 (a). The primitive lattice vectors $\{\mathbf{a}_1, \mathbf{a}_2, \mathbf{a}_3\}$ for an FCC lattice are:

$$\mathbf{a_1} = \frac{a}{2}(0,1,1), \quad \mathbf{a_2} = \frac{a}{2}(1,0,1), \quad \mathbf{a_3} = \frac{a}{2}(1,1,0)$$

where $a = 6.31$ Å is the length of the unit cell, such that the bond length between Sn-Te atoms is $a/2$.

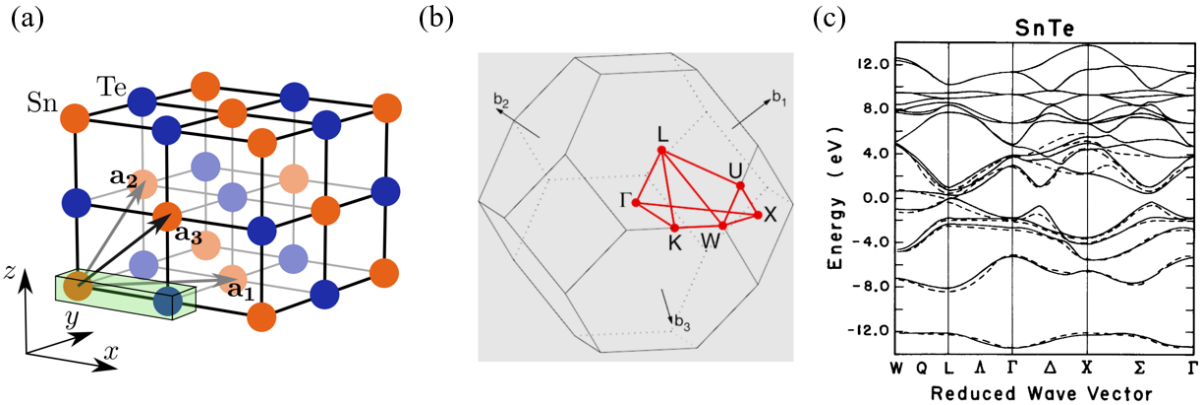

Figure 2.1: (a) Rock salt crystal structure SnTe. The unit cell (green box) consists of Sn and Te, the Bravais lattice vectors $\{\mathbf{a}_1, \mathbf{a}_2, \mathbf{a}_3\}$ span the FCC lattice [8]. (b) Bulk BZ of SnTe. (c) Bulk band structure of SnTe, taken from [9].

The electronic wave functions in a crystal can be described by utilizing the periodicity of the crystal. Bloch's theorem states that the solutions of the Schrödinger equation in a periodic potential can be expressed as a Bloch states

$$\psi_{n,\mathbf{k}}(\mathbf{r}) = e^{i\mathbf{k}\cdot\mathbf{r}} u_{n,\mathbf{k}}(\mathbf{r}) \tag{2.1}$$

where $u_{n,\mathbf{k}}(\mathbf{r})$ is a function that shares the same periodicity as the crystal. Each Bloch state is labeled by a (discrete) band index n and the wave vector $\mathbf{k}$.

The reciprocal lattice vectors $\{\mathbf{b}_1, \mathbf{b}_2, \mathbf{b}_3\}$ can be directly computed from the primitive lattice vectors using $\mathbf{a}_i \cdot \mathbf{b}_j = 2\pi\delta_{ij}$, with δ_{ij} the Kronecker delta. Using the reciprocal lattice vectors, reciprocal space can be constructed.
Adding a reciprocal lattice vector to the wave vector $\mathbf{k}$ does not change the wave function $\psi_{n,\mathbf{k}}(\mathbf{r})$. Therefore, all unique $\mathbf{k}$-vectors can be restricted to the Wigner–Seitz cell of the reciprocal space, known as the (first) Brillouin zone (BZ).
For bulk (3D) SnTe, the BZ has the shape of a truncated octahedron, shown in Figure 2.1 (b). It contains several high-symmetry points (HSP's) such as $\Gamma : (0,0,0)$, $X : \left(\frac{1}{2}, 0, 0\right)$, and $L : \left(\frac{1}{2}, \frac{1}{2}, \frac{1}{2}\right)$, given in the reduced coordinates relative to the reciprocal lattice vectors.

Each $\mathbf{k}$-point in reciprocal space corresponds to a distinct Bloch state, characterized by an energy E and wave function $\psi_{n,\mathbf{k}}(\mathbf{r})$. Since computing the band structure across the entire 3DBZ is computationally intensive, it is common practice to evaluate the band structure along a path connecting these HSP's, which is known as a high-symmetry path.
The band structure of bulk SnTe is shown in Figure 2.1. The L-point is of special interest, as the energy gap between the valence and conduction band is smallest there, placing SnTe among the IV–VI narrow-gap semiconductors.

Two important quantities that can be extracted from the band structure $E(k)$ are the group velocity and the effective mass.

$$v_g = \frac{1}{\hbar}\frac{dE}{dk} \tag{2.2}$$

$$m^* = \hbar^2 \left(\frac{d^2E}{dk^2}\right)^{-1} \tag{2.3}$$

The group velocity v_g determines how fast an electron wave packet moves through the crystal, determined by the slope of the energy band. The effective mass m^* describes how the electron responds to external forces (such as an electric field) and is related to the curvature of the band. A linear dispersion (e.g. near a Dirac cone) has zero curvature, resulting in an effective mass of $m^* = 0$.

When considering lower-dimensional geometries, such as slabs (2D) or nanowires (1D), the BZ also reduces its dimension. For example, in a slab geometry, translational symmetry is preserved only in the in-plane directions (as these have periodic boundary conditions), while broken in the out-of-plane direction (which has an open boundary condition). The momentum in the out-of-plane direction becomes discrete such that the 3DBZ is projected to a 2DBZ.
Since this is quite abstract, we make it more concrete by considering the following example. A nanowire with translational invariance along the z-axis, has a 1DBZ, characterized by a single momentum k_z. To relate this to a higher-dimensional BZ, for instance the 2DBZ (k_y, k_z) of a (100) slab, we notice that the difference between the slab and the nanowire is the replacement from a periodic boundary condition in the y-direction to an open boundary condition. In reciprocal space, this results in the formerly continuous momentum k_y becoming discrete, with allowed values $k_y = n \cdot 2\pi/L_y$, where L_y are the number of unit cells along the y-direction and $n \in \mathbb{N}$. The 2DBZ becomes effectively a set of 1DBZ cuts projected onto each other, labeled with continuous k_z and discrete k_y values.

2.1.2 Tight-binding approach

A widely used approximation for computing electronic band structures is the tight-binding (TB) approach. In this model, we assume that the electrons are primarily localized on individual atomic sites, but can also move (hop) in between sites due to some orbital overlap.

With this picture in mind, we can for example write the Hamiltonian of a simple 1D chain of atoms with nearest neighbor hopping:

$$H = \sum_n \epsilon_n |n\rangle\langle n| + \sum_{n \neq m} t_{nm} |n\rangle\langle m| \tag{2.4}$$

where $|n\rangle$ represents the orbital at site n. ϵ_n is the onsite energy of the orbital and t_{nm} the hopping between orbitals of neighboring sites n and m.

Solving the Schrödinger equation $H\psi = E\psi$ comes down to diagonalizing the Hamiltonian matrix. The eigenvalues correspond to the allowed energies E, while the eigenvectors ψ describe the associated wave functions.

Obviously this strategy raises problems when there is a translational invariant direction, as such systems contain an infinite number of sites. However, this translational symmetry can be exploited by performing a Fourier transform

$$|\mathbf{k}\rangle = \frac{1}{\sqrt{N}} \sum_n e^{i\mathbf{k}\cdot\mathbf{R}_n} |n\rangle, \tag{2.5}$$

where $\mathbf{R}_n$ denotes the position of the n-th site and N is the total number of sites.

Using these momentum states we can find the energy dispersion by diagonalizing the Hamiltonian. Its matrix elements read

$$H(\mathbf{k}) = \langle \mathbf{k}|H|\mathbf{k}\rangle = \frac{1}{N} \sum_{m,n} e^{-i\mathbf{k}\cdot\mathbf{R}_m} \langle m|H|n\rangle e^{i\mathbf{k}\cdot\mathbf{R}_n} = \epsilon_0 + \frac{1}{N} \sum_{\mathbf{R}\neq 0} t(\mathbf{R}) e^{i\mathbf{k}\cdot\mathbf{R}}, \tag{2.6}$$

where ϵ_0 is the onsite energy, $t(\mathbf{R})$ the hopping between sites separated by $\mathbf{R} = \mathbf{R}_n - \mathbf{R}_m$.
This shows how a translational invariance replaces the infinite number of sites in the Hamiltonian matrix by the wave vector $\mathbf{k}$.

Peierls substitution

Magnetic fields can be included into TB models using the Peierls substitution, which modifies the hopping amplitudes by attaching a phase factor $t_{nm} \to t_{nm} e^{i\varphi_{nm}}$, where φ_{nm} is the phase acquired by an electron hopping from site $\mathbf{r}_n$ to $\mathbf{r}_m$. This phase is given by

$$\varphi_{nm} = \frac{e}{\hbar} \int_{\mathbf{r}_n}^{\mathbf{r}_m} \mathbf{A} \cdot d\mathbf{l}, \tag{2.7}$$

where $\mathbf{A}$ is the vector potential associated with the magnetic field $\mathbf{B} = \nabla \times \mathbf{A}$, and $d\mathbf{l}$ is an infinitesimal line element along the hopping path. This substitution ensures gauge invariance and captures the influence of an external magnetic field [6].

2.2 Symmetries

Crystal structures are inherently highly symmetric. They are invariant under a set of point group symmetries, such as mirror reflections, rotations and inversion. These symmetries are not just aesthetic, they are deeply embedded in the physics of the system. In particular, they are present in the Hamiltonian that governs the electronic properties of the crystal.

In general, a symmetry is represented by an operator S. If the system is symmetric under this operation, the symmetry operator commutes with the Hamiltonian:

$$[H, S] = 0.$$

This implies that the symmetry imposes constraints on the energy eigenstates and eigenvalues of the system.

Symmetries have important consequences for the BZ as well. They reduce the number of unique points that need to be considered, because symmetry-related points in the BZ are physically equivalent. As a result, we can focus on a reduced BZ, which contains all the physical information.

We take a closer look at two key symmetries relevant to our study: time-reversal (TR) symmetry and crystalline mirror symmetries. We will explore how these symmetries act on the Hamiltonian, influence the structure of the BZ, and shape the band structure of the material.

2.2.1 Kramer's pairs

A system is TR symmetric if the system looks exactly the same if time would be reversed ($t \mapsto -t$). Under TR both momentum and spin are reversed $\mathbf{k} \mapsto -\mathbf{k}$ and $\boldsymbol{\sigma} \mapsto -\boldsymbol{\sigma}$.

This symmetry ensures that the energy bands $E(\boldsymbol{\sigma}, \mathbf{k}) = E(-\boldsymbol{\sigma}, -\mathbf{k})$, forming a so called Kramers pair at TR-invariant momenta (TRIM) such as $\mathbf{k} = 0$.

A system is inversion (I) symmetric if the system looks exactly the same if positions would be inverted ($\mathbf{r} \mapsto -\mathbf{r}$), such that $E(\boldsymbol{\sigma}, \mathbf{k}) = E(\boldsymbol{\sigma}, -\mathbf{k})$. Combined with TR symmetry, this ensures all bands in the band structure are two-fold degenerate.

2.2.2 Mirror symmetry

SnTe possesses an important set of mirror symmetries associated with the $\{110\}$ family of mirror planes. In particular, the (110) mirror symmetry, represented by mirror operator M, acts on the Bloch Hamiltonian as:

$$MH(k_x, k_y, k_z)M^{-1} = H(k_y, k_x, k_z). \tag{2.8}$$

From this, we see that the mirror-invariant plane in the BZ is defined by $k_x = k_y$. Therefore, the Bloch states within this plane are left invariant under the mirror operation and must be eigenstates of the mirror operator M.

Interestingly, if we apply the mirror operation twice, one might expect to recover the original state. However, for spin-$\frac{1}{2}$ particles such as electrons, a minus sign is picked up under a 2π rotation, leading to $M^2 = -1$. This implies that all (bulk) wave functions living in the mirror plane can be labeled by the mirror eigenvalues $M = \pm i$.

This allows the Hamiltonian to be block-diagonalized into two decoupled sectors:

$$H = H_i \oplus H_{-i} \tag{2.9}$$

where each block corresponds to states with mirror eigenvalue $+i$ or $-i$, respectively. Why this is useful will be discussed in a later section.

2.2.3 $k \cdot p$

Symmetries can also be used to study band structures analytically. In general, band structures can only be solved analytically in highly simplified models. As the complexity of the TB model increases, full exact solutions become impossible to find. However, it is still possible to analyze low-energy regions of the band structure analytically using perturbation theory along with symmetry constrains.

Since electrons occupy all states up to the Fermi energy E_F, it are primarily the states near E_F that determine the properties of a material. Therefore, developing an analytical understanding of the band structure in the vicinity of the Fermi level is particularly valuable. This can be achieved through an effective low-energy model, constructed using so called $\mathbf{k} \cdot \mathbf{p}$ theory, which we will outline here.

The periodic function $u_{n,\mathbf{k}}(\mathbf{r})$ of a Bloch state satisfies $H(\mathbf{k})u_{n,\mathbf{k}}(\mathbf{r}) = E_{n,\mathbf{k}}u_{n,\mathbf{k}}(\mathbf{r})$, which is similar to the Schrödinger equation but with Bloch Hamiltonian

$$H_{\mathbf{k}} = \frac{p^2}{2m} + \frac{\hbar\,\mathbf{k}\cdot\mathbf{p}}{m} + \frac{\hbar^2 k^2}{2m} + V \tag{2.10}$$

consisting of the standard Schrödinger Hamiltonian $H_0 = \frac{p^2}{2m} + V$ with an additional $\mathbf{k}$-dependent term. This term determines how the energy bands behave as a function of $\mathbf{k}$. In general there is no analytical solution. Using perturbation theory a low-energy model can still be constructed.
Suppose we are interested in the band structure near a particular HSP in the BZ, denoted by $\mathbf{k}_{\text{HSP}}$. Consider a small deviation $\delta\mathbf{k}$ from this HSP, such that $\mathbf{k} = \mathbf{k}_{HSP} + \delta\mathbf{k}$.

Expanding the Bloch Hamiltonian $H(\mathbf{k})$ up to first order in $\delta\mathbf{k}$, we obtain:

$$\begin{aligned} H(\mathbf{k}) &= H(\mathbf{k}_{HSP}) + \delta\mathbf{k}\cdot\nabla_{\mathbf{k}}H(\mathbf{k})|_{\mathbf{k}_{HSP}} + \mathcal{O}((\delta\mathbf{k})^2) \\ &= H(\mathbf{k}_{HSP}) + \frac{\hbar}{m}\delta\mathbf{k}\cdot(\mathbf{p} + \hbar\mathbf{k}_{HSP}) + \mathcal{O}((\delta\mathbf{k})^2). \end{aligned} \tag{2.11}$$

Since this is a Taylor expansion, the approximation is only valid when $\delta\mathbf{k}$ is small (i.e. close to the HSP). Therefore, $k \cdot p$ theory serves as an effective low-energy model. Treating $\delta\mathbf{k}\cdot\mathbf{p}$ as a perturbation, energy bands and wave functions can be analytically studied. From this, parameters such as the effective mass and group velocity can be extracted.

In constructing $k \cdot p$ models, symmetries play a crucial role. The crystal symmetries at HSP's constrain the allowed terms in the effective Hamiltonian.

For SnTe, the $k \cdot p$ model near the L-points in the BZ is given by [3]:

$$H(\mathbf{k}) = m_0\, s_0 \otimes \sigma_z + v(k_1 s_2 - k_2 s_1) \otimes \sigma_x + v_3 k_3\, s_0 \otimes \sigma_y, \tag{2.12}$$

where $\vec{s}$ and $\vec{\sigma}$ are Pauli matrices acting in spin and orbital space, respectively. This Hamiltonian describes a Dirac cone when the mass term $m_0 = 0$, when $m_0 \neq 0$, an energy gap opens.

Interestingly, the sign of the mass term m_0 is not merely a detail, it carries physical meaning. In order to explain its physical significance, we need to introduce topology.

2.3 Topology

Topology is the mathematical study of properties of spaces that remain invariant under continuous deformations. A classic example illustrating this is the topological equivalence of a coffee mug and a doughnut, which can be continuously deformed into each other. A sphere is not topologically equivalent to either the coffee mug or the doughnut, as deforming it into one of these shapes would require creating a hole, which is not allowed under continuous deformation.

In condensed matter physics, the topology of a material is not protected by a physical hole, but by the energy gap between the valence and conduction bands in its electronic band structure. In other words, two materials are topologically equivalent if the Hamiltonians describing them can be continuously deformed into each other without closing the energy gap. If the energy gap must close in order to continuously deform the band structure of one system into that of the other, the two systems belong to different topological phases.

Systems in different topological phases give rise to a wide range of interesting and physical phenomena. In what follows, we will touch upon the basic topology concepts relevant for this thesis.

2.3.1 Topological (crystalline) insulator

Topological insulators (TI's) are a subclass of topological materials. To build an understanding of the physics of TI's, we first examine two well-known quantum Hall systems. This foundation allows us to explore the general band structure characteristics of a TI.

From quantum Hall systems to topological insulators

The integer quantum Hall insulator (IQHI) was historically the first encounter with a quantum phase characterized by topology. Its phase is based on the integer quantum Hall effect, where applying a magnetic field perpendicular to a two-dimensional (2D) material induces unidirectional (chiral) edge states, schematically shown in Figure 2.2 (a). This is an example of a Chern insulator, which refers to 2D systems with an insulating bulk and conducting edge states.

The topological phases of the IQHI are characterized by the Chern number C, which serves as the topological invariant of this system. It can be shown that the Chern number must be an integer, meaning the IQHI possesses a $\mathbb{Z}$ invariant. Specifically, when $C = 0$, the system is in a trivial phase, without any edge states. When $C \neq 0$, the system enters a non-trivial topological phase, hosting chiral edge states. The Chern number can also be related to the number of edge states and therefore the quantized conductance seen in the integer quantum Hall effect. Therefore, the Chern number provides the theoretical tool to understand the IQHI in terms of topology. Computing the Chern number involves integrating over the energy bands in the BZ. The mathematical formulation of the Chern number can be found in Hatsugai et al. [10].

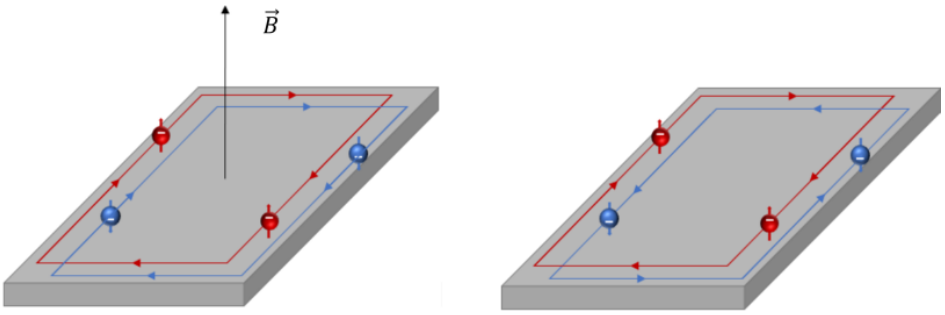

(a) IQHI (b) QSHI

Figure 2.2: Schematic illustration of the (a) integer quantum Hall insulator (IQHI) with chiral edge states, and (b) the quantum spin Hall insulator (QSHI) with helical edge states. This illustration was taken from [11].

It is important to highlight that the IQHI relies on an external magnetic field to generate edge states. In other words, these edge states exist due to broken TR symmetry. In topological systems, the presence or absence of symmetries plays a crucial role in determining whether a phase is trivial or non-trivial.

A related system, where TR symmetry must remain intact (instead of broken) to sustain a topological non-trivial phase, is the quantum spin Hall insulator (QSHI). Unlike the IQHI, the QSHI hosts two counter-propagating spin-polarized (helical) edge states, depicted schematically in Figure 2.2 (b). In this system, no external magnetic field is required. Instead, strong spin-orbit coupling (SOC) generates the edge states, with TR symmetry protecting them from backscattering. The corresponding topological invariant for the QSHI is the $\mathbb{Z}_2 = (0, 1)$ index [12]. This invariant differentiates the trivial phase (no edge states) from the non-trivial phase (with helical edge states).

The principles explaining the IQHI and QSHI provide a foundation for understanding topological insulators. The described ideas extend naturally to three-dimensional topological insulators, where protected surface states arise from non-trivial band topology. To understand these topological phases quantitatively, we will now study the band structure characteristics of a topological insulator.

Topological band structure characteristics

The schematic band structure of a trivial insulator is illustrated in Figure 2.3 (a). In this case, the valence and conduction bands are well seperated by the energy gap E_g. The Fermi level lies within this gap, as (at half-filling) the valence band is fully occupied while the conduction band is empty. This is of course at zero temperature, which is the regime considered in this thesis.

Figure 2.3 (b) schematically illustrates the band structure of a TI. Unlike a trivial insulator, a TI exhibits spectral flow, meaning that gapless states provide a continuous connection between the valence and conduction bands. These gapless states exist within the bulk energy gap and are localized at the boundaries of the material (i.e. boundary states). In a 3D TI, they appear as surface states, while in a 2D TI, they manifest as edge states.

Note that the band structure of a trivial insulator and a topological insulator cannot be continuously deformed into one another without closing the energy gap, indicating that they belong to topologically distinct phases.
An important difference between the bulk bands of these phases is band inversion, where the usual ordering of conduction and valence bands is reversed due to strong SOC. This inversion changes the topological character of the bulk bands and leads to the emergence of protected gapless boundary states.

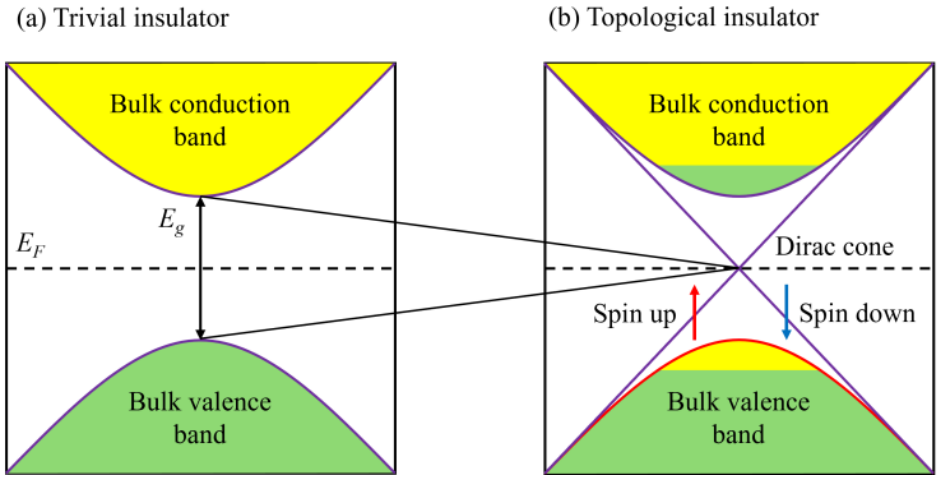

Figure 2.3: Schematic illustration of band structures. (a) Trivial insulator: the conduction and valence bands are separated by an energy gap (E_g), with the Fermi level (E_F) positioned within the gap. (b) Topological insulator: features spin-polarized gapless states forming a Dirac cone, with band inversion indicated.

These gapless states have a linear dispersion relation, forming the characteristic Dirac cone. The Dirac point is typically located at TRIM points in the BZ. Due to the linear dispersion, these gapless states behave as massless fermions, as there effective mass becomes zero ($m^* = 0$). This means that the electron response is extremely sensitive to an external force, allowing for dissipationless transport.

The gapless states also exhibit spin-momentum locking. This occurs in materials with strong SOC, giving rise to spin-polarized states. In such materials, the electron's spin becomes tied to its momentum. In a low-energy model this is typically captured by $\mathbf{k} \cdot \sigma$ terms, as can be seen in the $k \cdot p$ Hamiltonian from eq. 2.12.

Although gapless states are localized at the boundary, their wave functions penetrate into the bulk with an exponential decay: $\psi = e^{-z/\xi}$, characterized by the penetration depth ξ.
If wave functions of gapless states localized on opposing boundaries of a material have a finite overlap, they hybridize and open a finite-size-induced energy gap in the Dirac cone. The overlap of the surface states on opposing sides of a slab geometry is approximately given by

$$\langle \psi_{\text{top}} \mid \psi_{\text{bottom}} \rangle \sim e^{-N/\xi}, \tag{2.13}$$

where N is the number of layers of the slab geometry. Therefore, the finite-size-induced energy gap scales as $E_g \sim e^{-N/\xi}$. Thus, only if the system size $N >> \xi$ we expect to see a clear Dirac cone.

Topological protection

Assuming we have a system that is large enough, such that there are no hybridization effects, the Dirac cone is protected by the symmetry that protects the topology of the system.
For instance, for the QSHI, breaking TR symmetry would destroy its topological protection, leading to a gapped Dirac cone (i.e. a finite energy gap).

The topology of a material can be quantified through topological invariants, which mathematical formulation depends on the underlying symmetries of the system and its Bloch bands. In general, using the local symmetries: TR, particle hole and chiral symmetry, the topology of a material can be classified using the Altland-Zirnbauer classification.

Another class of TI's is the topological crystalline insulator (TCI), which will be focused on in this thesis. It is novel in the sense that the topological protection relies on crystalline point group symmetries, rather than local symmetries.

SnTe is an example of such a TCI. The symmetry protecting the topology is the family of $\{110\}$ mirror symmetry planes. The topological invariant for SnTe is the mirror Chern $C_m = -2$. The mirror Chern number is defined as

$$C_m = (C_i - C_{-i})/2 \tag{2.14}$$

where $C_{\pm i}$ are the Chern numbers corresponding to each sector in the block-diagonalized Hamiltonian from eq. 2.9. TR symmetry ensures $C_i + C_{-i} = 0$, but the difference can be non-zero, defining the non-trivial mirror Chern number [13].

For SnTe, the mirror Chern number in each of the $\{110\}$ mirror planes has been computed to be $C_m = -2$. Therefore, SnTe is expected to host an even number of Dirac cones on high-symmetry crystal surfaces such as $\{001\}$, $\{110\}$, and $\{111\}$ [3]. These Dirac cones are topologically protected by the $\{110\}$ mirror plane.

When the mirror symmetry plane protecting the Dirac cone is broken, the Dirac cone becomes gapped. A natural way of breaking a mirror symmetry is by applying strain to the material.
Strain deforms the crystal, causing atoms to stretch and squeeze. This effectively changes bond lengths, altering the overlap between orbitals. This symmetry breaking removes the (onsite) degeneracy of the orbitals, causing them to split in energy.

This effect can be modeled using a crystal field splitting term characterized by the strain strength parameter Δ (see supplementary materials of Schindler et al. [5]). The lowest order term capturing this anisotropy is given by:

$$H_{\mathrm{CF}} = \frac{\Delta}{2}\left[(\mathbf{L}\cdot\mathbf{d}_2)^2 - (\mathbf{L}\cdot\mathbf{d}_1)^2\right] \tag{2.15}$$

where $\mathbf{L} = (L_x, L_y, L_z)$ is the orbital angular momentum operator. Unit vectors $\mathbf{d}_1$ and $\mathbf{d}_2$ specify the directions along which the strain is applied.

Although strain also modifies the hopping terms by altering the overlap integrals, we will neglect this effect, as the crystal field splitting term already captures the relevant symmetry-breaking behavior.

Finally, because strain modifies the bond lengths, it can potentially change the band inversion and induce a topological phase transition, as SnTe is not trivially connected to the atomic limit [3]. Therefore, it should be checked for which strain strength Δ the bulk energy gap E_g closes.

2.3.2 Bulk-boundary correspondence

The link between the topological invariant (determined solely by the bulk) and the presence/absence of gapless surface (or edge) states is known as the bulk-boundary correspondence [14]. In other words, the topological properties of the bulk alone indicate the existence of gapless states.

This principle provides a theoretical framework that explains the robustness of gapless boundary states. In order to eliminate the gapless states, the system's topological invariant must be changed, which would require a topological phase transition.

An intuitive picture of bulk-boundary correspondence arises when considering a domain wall, which can be an interface between a trivial and non-trivial system.

Domain wall

Bulk-boundary correspondence predicts protected boundary states based solely on bulk topology. Another way to interpret these boundary states is as arising from a domain wall. This scenario can be analytically analyzed using $k \cdot p$ theory.

An important term in the $k \cdot p$ Hamiltonian of SnTe (eq. 2.12) is the mass term m_0, whose sign determines the topological phase of the system: $m_0 > 0$ corresponds to a band-inverted non-trivial phase (e.g. SnTe), while $m_0 < 0$ corresponds to a trivial insulator (e.g. PbTe).

For a domain wall, the effective mass m_0 changes sign at the interface, introducing a spatial dependence $m_0 \to m(x)$. Starting from the $k \cdot p$ Hamiltonian for SnTe (Eq. 2.12) and simplifying to one dimension (setting $k_1 = k_2 = 0$) in position space ($k_3 \to -i\partial_x$), yields

$$H(x) = -iv_3\sigma_y\partial_x + m(x)\sigma_z \tag{2.16}$$

This 1D Dirac Hamiltonian was first studied by Jackiw-Rebbi [15]. Solving it for a mass profile that changes sign at the interface reveals a bound state ($E = 0$) localized at the interface. The state decays exponentially into the bulk $\psi \sim e^{-x/\xi}$.

This analyses can be generalized to higher dimensions, the principle remains the same: a domain wall is accompanied by a bound state localized at the interface and decaying exponentially into the bulk. This provides the theoretical basis for the gapless states we encountered earlier.

Importantly, a domain wall is not necessarily an interface between a trivial and a non-trivial system. It can also arise in other contexts. For example, when two surfaces meet to form a hinge, which we will turn our attention to now.

Hinge states

Higher-order topological insulators (HOTIs) go beyond the conventional bulk-boundary correspondence. Unlike TI's, where gapless states appear on boundaries one dimension lower than the system, HOTIs host gapless states on boundaries that are two or more dimensions lower. In a 3D HOTI, this means that the gapless states can appear along 1D hinges instead of 2D surfaces. SnTe has been identified as a HOTI, hosting helical hinge states at the edges of a nanowire [5].

Figure 2.4 illustrates the formation of these hinge states. First consider a surface hosting two gapless Dirac cones. Tilting the surface on both ends breaks the mirror symmetry that was protecting the surface Dirac cones, allowing a mass term in the $k \cdot p$ Hamiltonian. Since the angles are opposite $\pm\alpha$, it can be shown that the mass terms are opposite [5]. Therefore, these two surfaces form a domain wall at the hinge. This gives rise to a pair of counter-propagating protected hinge states. Increasing the tilting angle cannot remove the hinge state, as long as the opposite surfaces map into each other such that the mirror symmetry at the hinge is preserved.

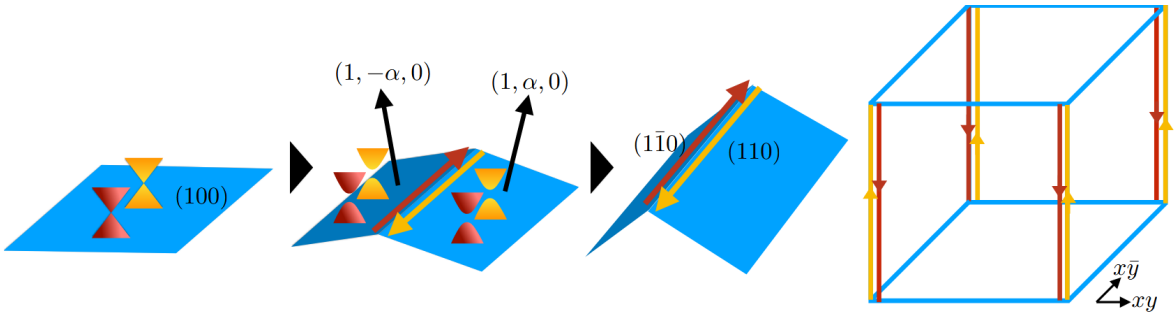

Figure 2.4: Formation of hinge states, image taken from [16].

2.4 Scattering matrix formalism

The study of quantum transport has historically proven to be a powerful tool in identifying and characterizing topological phases. A prime example is the integer quantum Hall insulator (IQHI), where quantized plateaus in the Hall conductance are directly related to the topological invariant.

What distinguishes a non-trivial topological insulator from a trivial one is the presence of robust, spin-polarized, gapless surface states. Since these states cross the Fermi level, they can support conduction even when the bulk is insulating. Studying the conductance around the bulk energy gap thus provides direct insight into the nature and presence of such topological surface states.

By studying the quantum transport properties of SnTe nanowires, we aim to identify transport signatures of the gapless states present. Conductance is numerically computed using the scattering matrix formalism, which we introduce in this section.

Scattering problem

In order to study the quantum transport properties of the nanowire structures, we need a way to extract the conductance from our system. In the ballistic mesoscopic regime, computing conductance G comes down to finding the total transmission probability T between incoming and outgoing modes. Finding these probabilities for a particular configuration is known as a scattering problem.

Figure 2.5 illustrates a general 1D scattering problem. An incoming mode encounters a scattering region, visualized as a potential barrier $V(x)$. The goal is to find the transmission probability t, i.e. the probability of the incoming mode scattering into an outgoing mode. From current conservation, the reflection probability is directly related by $|r|^2 + |t|^2 = 1$.

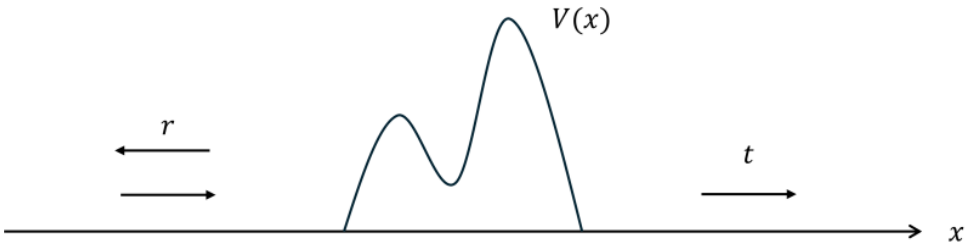

Figure 2.5: Schematic illustration of a 1D scattering problem.

To solve this system, we discretise everything onto a lattice. Since the wavefunctions in the incoming/outgoing leads are known (plane waves), they can be matched to the wavefunction in the scattering region. This results in a linear system of equations that can be numerically solved to obtain the transmission amplitudes. For further details, see [17].

In this thesis, the scattering geometry involves two leads connected via a central scattering region. We fix the energy E and define M_0 and M_1 as the number of propagating modes in lead 0 and lead 1, respectively. The reflection and transmission amplitudes between incoming and outgoing modes are summarized by the scattering matrix

$$S = \begin{bmatrix} S_{00} & S_{01} \\ S_{10} & S_{11} \end{bmatrix}$$

Each block is a submatrix describing scattering between modes in the leads. S_{00} and S_{11} correspond to reflection within leads 0 and 1, respectively, while S_{01} and S_{10} describe transmission between the leads.

In particular, we are interested in the submatrix S_{01}, which has dimensions $M_0 \times M_1$. The total transmission probability T_{01} is given by the squared Frobenius norm of S_{01}, i.e. the sum of all mode-to-mode transmission amplitudes.

Conductance

The Landauer-Büttiker formula relates the total transmission probability to the conductance:

$$G = \frac{e^2}{h} T_{01} = \frac{e^2}{h} \sum_{ij} |S_{01}^{ij}|^2 \tag{2.17}$$

where h is Planck's constant and e is the elementary charge, with the prefactor e^2/h defining the conductance quantum.

We study the conductance as a function of energy E, particularly in the energy range between the valence and conduction bands, where the gapless states are located. The conductance spectrum $G(E)$ reveals how states at different energies contribute to transport through the scattering region. It is especially sensitive to the presence of confined or extended states in the scattering region.
For example, when the scattering region supports confined quasi-bound states, due to confinement from two potential barriers, resonant tunneling occurs. In that case, when the energy of an incoming mode matches the energy of a confined state, a sharp peak occurs in the conductance spectrum $G(E)$. In contrast, when states are not confined, conductance varies more smoothly with energy.

When computing conductance with leads connected perpendicular the infinite nanowire system (probing conductance in the transverse direction), a k_z value needs to be specified. To account for all states contributing to transport, the total conductance is obtained by integrating over the one-dimensional BZ of the nanowire:

$$G(E)/L = \frac{1}{2\pi} \int G(k_z, E)\, dk_z \approx \frac{1}{2\pi} \sum_{k_z} G(k_z, E) \Delta k \tag{2.18}$$

where L is the wire length. The sum approximates the integral under the assumption that $G(k_z, E)$ is smooth.
Note that integrating over the states in the BZ is not necessary when attaching leads parallel to the nanowire (the longitudinal direction), as in that case the scattering region is finite.

3 Tight-binding models and validation

This section presents the tight-binding (TB) approach applied to SnTe. We introduce two distinct TB models, validate their implementation, and demonstrate their topological equivalence. This will be carried out through characteristic examples involving both bulk and slab geometries. Along the way, we will discuss important concepts such as penetration depth, spin-momentum locking, and the topological phase transition.

3.1 Tight-binding models

In literature on theoretical studies of SnTe, two TB models are frequently used. In this work, we will refer to these two models as the Hsieh model [3] and the Lent model [9].

The Lent model is historically most widely used and is considered the more accurate model. The TB Hamiltonian includes onsite potentials, nearest-neighbor hopping, and a spin-orbit coupling (SOC) term. It includes s-, p-, and d-orbitals, in total 18 orbitals per atom (one s, three p, and five d, each with spin degeneracy). While including a lot of orbitals makes the model more accurate, it also significantly increases the Hamiltonian size. Between these orbitals, it incorporates not only the dominant σ-bonding term, but also the higher-order bonding interactions such as the π- and δ-bonds. The Hamiltonian as well as the parameters used for the Lent model, are presented in the Appendix A1.

The Hsieh model is used as an effective model, designed to capture the essential topological features of SnTe near the Fermi energy. It considers only the p- orbitals with σ-bonding, as these give the dominant contributions around the Fermi energy. This decreases the DOF to 6, making it computationally much more efficient. For most of the results presented in this thesis, we use the Hsieh model. Therefore, we will take a closer look at its TB Hamiltonian:

$$\begin{aligned} H_{tb} = & m \sum_j (-1)^j \sum_{\mathbf{r},\alpha} \mathbf{c}^\dagger_{j,\alpha}(\mathbf{r}) \cdot \mathbf{c}_{j,\alpha}(\mathbf{r}) \\ & + \sum_{j,j'} t_{jj'} \sum_{(\mathbf{r},\mathbf{r}'),\alpha} \mathbf{c}^\dagger_{j,\alpha}(\mathbf{r}) \cdot \hat{\mathbf{d}}_{\mathbf{r}\mathbf{r}'} \hat{\mathbf{d}}_{\mathbf{r}\mathbf{r}'} \cdot \mathbf{c}_{j',\alpha}(\mathbf{r}') + h.c. \\ & + \sum_j i\lambda_j \sum_{\mathbf{r},\alpha,\beta} \mathbf{c}^\dagger_{j,\alpha}(\mathbf{r}) \times \mathbf{c}_{j,\beta} \cdot \mathbf{s}_{\alpha,\beta}. \end{aligned} \tag{3.1}$$

The first line represents the onsite potentials at the sites, labeled by position $\mathbf{r}$. The first term m is the onsite potential difference between Sn and Te. Index j labels Sn ($j = 1$) and Te ($j = 2$), $\alpha = \uparrow, \downarrow$ the spin. The creation ($\mathbf{c}^\dagger$) and annihilation ($\mathbf{c}$) operators are vector operators, written in the following basis:

$$\{|p_x,\uparrow\rangle, |p_y,\uparrow\rangle, |p_z,\uparrow\rangle, |p_x,\downarrow\rangle, |p_y,\downarrow\rangle, |p_z,\downarrow\rangle\}$$

The second term includes the nearest ($t_{12} = t_{21}$) and next-nearest (t_{11} and t_{22}) neighbor hopping terms. The dot product with unit vector $\hat{\mathbf{d}}_{\mathbf{r}\mathbf{r}'}$ between sites $\mathbf{r}$ and $\mathbf{r}'$ ensures σ-bond hopping.
The third term is the SOC term, written in terms of creation and annihilation operators. It can be easily implemented using $\mathbf{L} \cdot \mathbf{S} = \sum_{i=0}^{2} (\sigma_i \otimes L_i)$, where $\lambda_{1,2}$ represents the strength of the SOC.

When using the Hsieh model, the following set of parameters will be used: $m = -1.65$, $t_{11} = -t_{22} = 0.5$, $t_{12} = t_{21} = 0.9$, $\lambda_1 = \lambda_2 = 0.7$. These parameters were also used in previous studies of SnTe

nanowires [6]. Using the topological invariants presented in [7], it can be checked that these parameters fall within the topological regime. Parameters used for the Lent model are given in the Appendix A1.

These TB models were implemented using Kwant [17]. Kwant is a Python library for numerical calculations involving TB models, designed to make the simulation and implementation as easy as possible. Since these models give rise to large sparse matrices, the MUMPS library [18] was used. The code used to produce the results presented in this thesis is publicly available on GitLab[1]. For the implementation of the Lent model, existing code, written by Dániel Varjas was used[2].

[1] https://gitlab.kwant-project.org/qt/tci_surface_states/-/tree/master?ref_type=heads
[2] https://gitlab.kwant-project.org/qt/SnTe/-/blob/master/model/SnTe_models.py?ref_type=heads#L125

3.2 Model validation

This section covers the analyses of SnTe in both bulk and slab geometries, focusing on systems that are well understood and have been extensively studied in literature. Our goal is twofold: validate our implementation of the tight-binding (TB) models as well as demonstrating the topological equivalence between the Hsieh and Lent TB models.

To justify the use of the Hsieh model in later sections, it is important to establish that both models exhibit equivalent topological band structure features, specifically Dirac cones and surface states. We will also cover other relevant topics in the context of topological states, like penetration depth and spin-momentum locking.

3.2.1 Bulk

Figure 3.1 (a) shows the bulk band structure of SnTe along a high symmetry path, computed using the Lent TB model. Parameters reported in the Lent paper [9] were used using the Slater-Koster sign convention ($V_{p,s}$ $V_{p,d}$ and $V_{p,d\pi}$ opposite sign), presented in Appendix A1. This sign convention seems to give slightly better fits with other SnTe band structure computations (for more details, see the supplementary materials of Safaei et al. [19]).
Figure 3.1 (b) gives a zoomed-in view of the band structure (a) around the energy gap. The band gap is smallest at the L-points, with E_g = 0.22 eV. The colors indicate the weight of the wavefunction on the Sn-atom $|\psi_{Sn}|^2$. The exchange of the band character at L-point, indicates the intrinsic band inversion of SnTe [3].

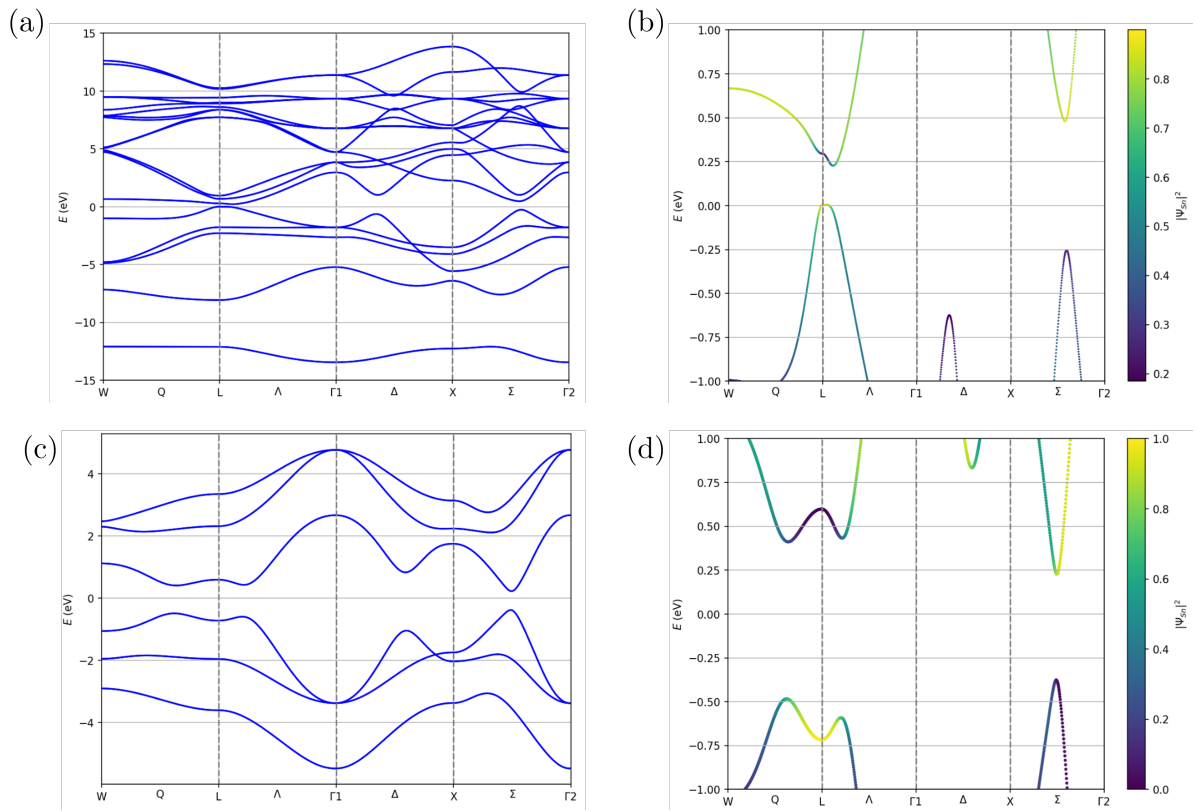

Figure 3.1: Bulk band structure for the (a) Lent and (c) Hsieh models. (b) Zoomed-in view of the band gap for the (b) Lent and (d) Hsieh models, showing intrinsic band inversion at the L-point.

Figure 3.1 (c) shows the bulk band structure for the Hsieh TB model. Interestingly, the smallest energy gap does not occur at the L-point, but rather along the Σ line, where E_g = 0.60 eV. Figure 3.1 (d) again illustrates band inversion between the valence and conduction band, which is absent along the Σ line.

The combination of band inversion, {110} mirror symmetry protection and a small energy gap, is what gives rise to the topological states. Therefore, topological behavior is expected at the projections of the L-point.

It is important to note that the energy scales of the Lent and Hsieh models differ. However, what matters for our numerical analyses is their topological equivalence, which will be further demonstrated in the following section.

3.2.2 Slab geometries

SnTe is known to have robust surface states with an even number of Dirac cones on crystal surfaces such as {001}, {110} or {111}, which are symmetric about {110} mirror planes [3]. Figure 3.2 indicates the (a) (001)-, (b) (110)- and (c) (111) Miller planes (in green). These planes can form the surface termination of slab geometries.

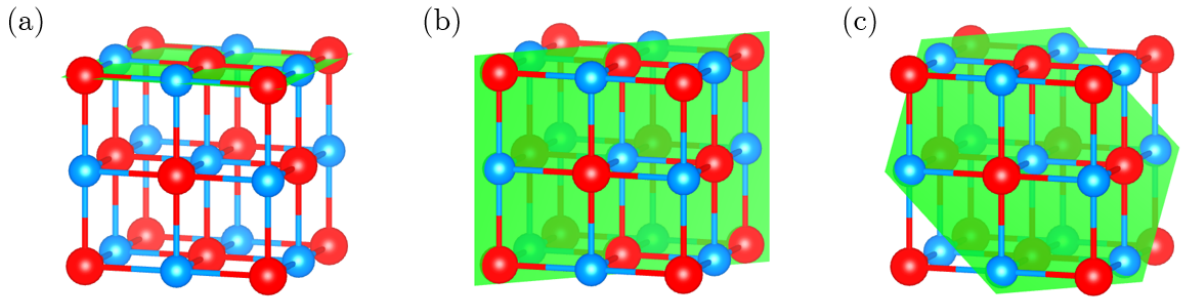

Figure 3.2: Rock-salt crystal structure showing (a) (001)-, (b) (110)- and (c) (111) Miller planes (in green).

In contrast to three lattice vectors for the bulk, a slab geometry has two lattice vectors $\mathbf{a}_1$ and $\mathbf{a}_2$. Which specific vectors these are, depends on the surface termination. Table 3.1 gives the lattice vectors {$\mathbf{a_1}$, $\mathbf{a_2}$} as well as the normal vector $\mathbf{n}$ for each surface termination of interest.

Kwant constructs the slab geometry by applying periodic boundary conditions along the translational invariant directions, defined by the lattice vectors. In the direction normal to the slab's surface $\mathbf{n}$, Kwant applies an open boundary condition, which can be used to set the thickness of the slab.

Table 3.1: Lattice vectors {$\mathbf{a_1}$, $\mathbf{a_2}$} and surface normal $\mathbf{n}$ of slab geometries with [001]-, [110]-, and [111] surface termination.

Surface termination	$\mathbf{a}_1$	$\mathbf{a}_2$	$\mathbf{n}$
[001]	(1, 1, 0)	(1, -1, 0)	(0, 0, 1)
[110]	(0, 0, 2)	(1, -1, 0)	(1, 1, 0)
[111]	(1, -1, 0)	(1, 0, -1)	(1, 1, 1)

Going from three to two translational invariant directions also means going from a 3D Brillouin zone (3DBZ) to a 2D Brillouin zone (2DBZ). Figure 3.3 shows how the 2DBZ projections (marked in green) originate from the 3DBZ. The corresponding {110} mirror planes are marked in the 3DBZ (in yellow), as well as their projections as a dotted line in the 2DBZ.

Note that the Dirac cones must be located within the mirror plane in the 3DBZ or on its projected dotted lines in the 2DBZ, since the topological protection of the Dirac cone originates from this mirror symmetry. The high symmetry L-points are indicated in the 3DBZ, the dotted vertical lines indicate their projections onto the 2DBZ. The Dirac cones are expected to be located at these points. HSPs in the 2DBZ are indicated by a bar on top of them. For example: L_1 and L_2 from the 3DBZ, project onto $\bar{X}_1$ in the 2DBZ.

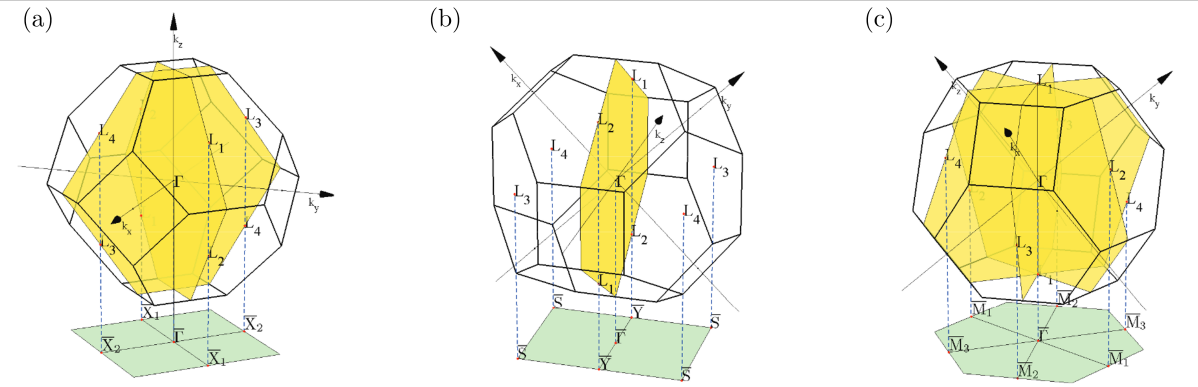

Figure 3.3: 2D Brillouin zone projections (in green) for the (a) (001)-, (b) (110)- and (c) (111)- slab geometries. The {110} mirror planes are indicated (in yellow). This figure was taken from [20].

Slab (001)

Figure 3.4 (a) shows the band structure of the (001) slab geometry, for a thickness of 61 atoms. The color indicate the weight of the wavefunction on the Sn atom $|\psi_{\mathrm{Sn}}|^2$. The Dirac cone is present at the $\bar{\Gamma} - \bar{\mathrm{X}}$ line, but not exactly located at $\bar{\mathrm{X}}$. It exhibits a Lifshitz shift [21], due to intervalley scattering between different L-points [22]. The Dirac point is located at $E = 0.15$ eV. Figure 3.4 (c) indicates the path taken through the 2DBZ in red.

This illustrates an important distinction between topological crystalline insulators (TCIs) and time-reversal invariant topological insulators (TIs). In TCIs, the Dirac cones are protected not by time-reversal symmetry but by crystalline symmetries. As a result, surface Dirac cones in TCIs are not constrained to appear at time-reversal-invariant momenta (TRIMs), but can instead occur at non-TRIM points in the Brillouin zone, provided the protecting crystal symmetries remain unbroken.

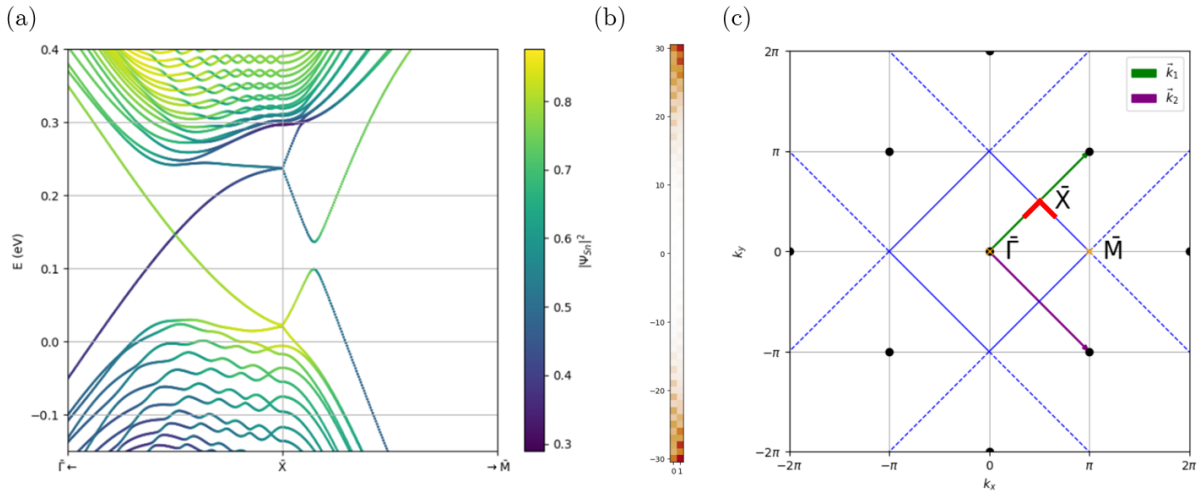

Figure 3.4: (a) Band structure of a (001) slab, obtained using the Lent TB model. (b) Surface state at the Dirac cone. (c) Brillouin zone for the (001) slab. The path along which the band structure is computed is indicated by red.

The bands are twofold degenerate, due to the simultaneous presence of inversion and time-reversal symmetry [23]. Giving rise to a fourfold degenerate Dirac point, creating a degenerate subspace of four orthonormal wave functions $\{\psi_1, \psi_2, \psi_3, \psi_4\}$. To visualize this state, we sum the probability densities and plot them onto the unit cell of the slab, shown in 3.4 (b). Clearly the states are localized at the surface of the slab, exponentially decaying into the bulk.

Figure 3.5 (a) shows the band structure computed using the Hsieh TB model. It has the same topological features as the Lent TB model. We see a Dirac cone at the $\bar{\Gamma} - \bar{X}$ line with a Lifshitz shift. Again, inspecting the probability density of the fourfold degenerate Dirac point shows a surface state in Figure 3.5 (b).

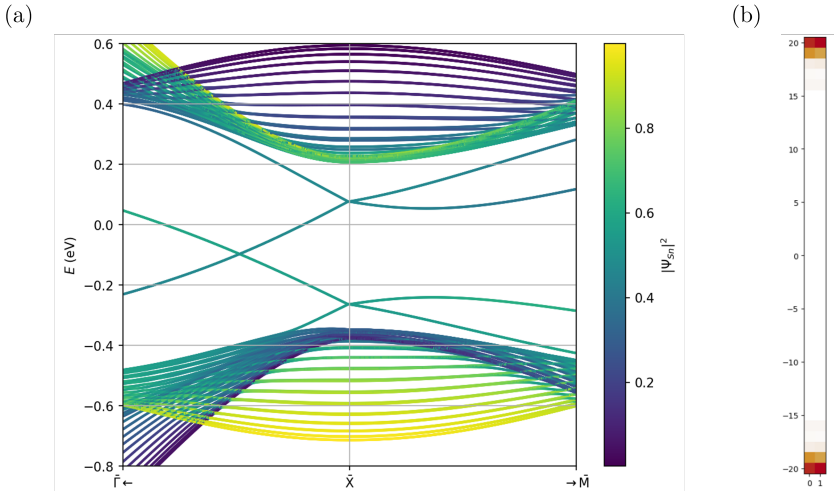

Figure 3.5: (a) Band structure of a (001) slab, obtained using the Hsieh TB model. (b) Surface state at the Dirac point.

An important distinction between the Hsieh and Lent models lies in the localization length of their surface states. Specifically, the surface state in the Hsieh model decays more rapidly into the bulk, indicating a shorter localization length compared to that of the Lent model. This characteristic, will be examined in more detail in the next section.

The Dirac point of the Hsieh band structure is located at $E = -0.096$ eV, indicating an energy offset compared to the Lent model. The energy gap seen in the Hsieh model (Fig. 3.5) is approximately twice that of the Lent model (Fig. 3.4). Beside the offset in the Dirac point and difference in the energy gap, both band structures exhibit similar qualitative features.

Slab (110)

Figure 3.6 shows the overlayed band structures of the (110) slab, for the Hsieh and Lent model. The Hsieh band structure is given an energy offset (0.22 eV) for a clear visual comparison. Both band structures have the same topological characteristics. There is a Dirac cone located at the $\bar{\Gamma} - \bar{Y}$ line, which is protected by the $\{110\}$ mirror plane symmetry of the crystal (see Figure 3.3 (b)). The Dirac cone again exhibits a Lifshitz shift.
There appears to be an avoided crossing around the $\bar{S}$ point, which makes sense as there is an L-point projection onto $\bar{S}$, but it does not coincide with the $\{110\}$ mirror plane and is therefore not protected.

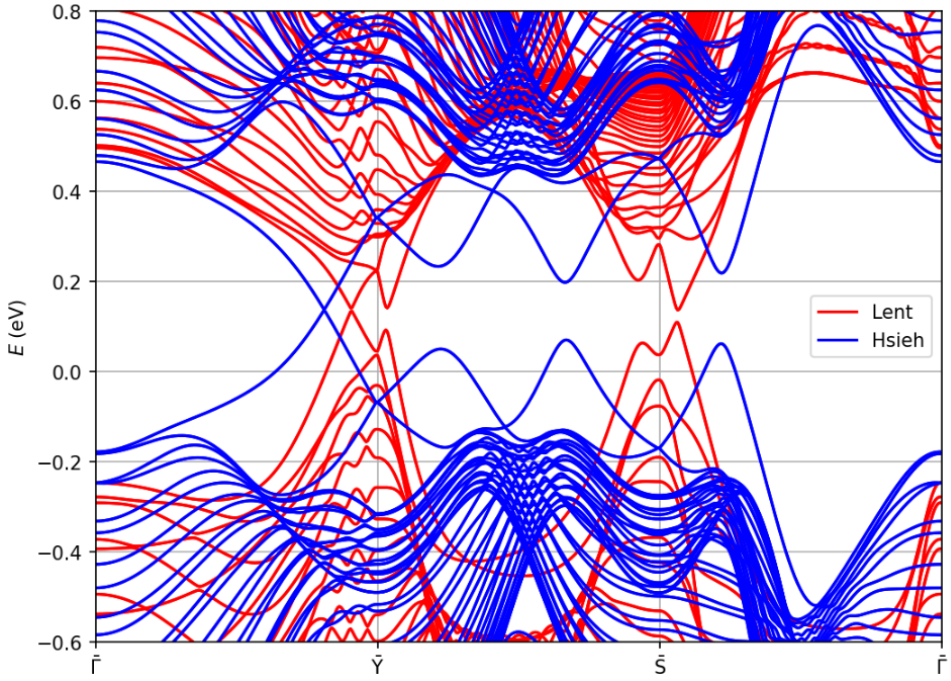

Figure 3.6: Overlayed band structures of the (110) slab for the Hsieh and Lent model.

Slab (111)

Although the (111) surface termination is of theoretical interest, it will not be the focus of this thesis. We concentrate on nanowires with (001) and (110) surface terminations, which are experimentally more stable and commonly realized. For completeness, the (111) surface is briefly discussed in the context of a slab geometry.

Figure 3.7 shows the overlayed band structure of the (111) slab, for the Hsieh and Lent model. The Dirac cone is located at $\bar{\Gamma}$ and $\bar{M}$, with no Lifshitz shift as there is no intervalley coupling [22].
Note that this surface termination consists of a single type of atom, either all Sn or all Te. In Figure 3.7 the slab thickness is 61 layers, with both surfaces Te-terminated. The Dirac points lie close to the bottom of the conduction band. The Dirac point at $\bar{M}$ is even hidden in the bulk band. Though it might be possible to shift it within the band gap, using a surface potential, which would make them accessibly to probe in experimental measurements.

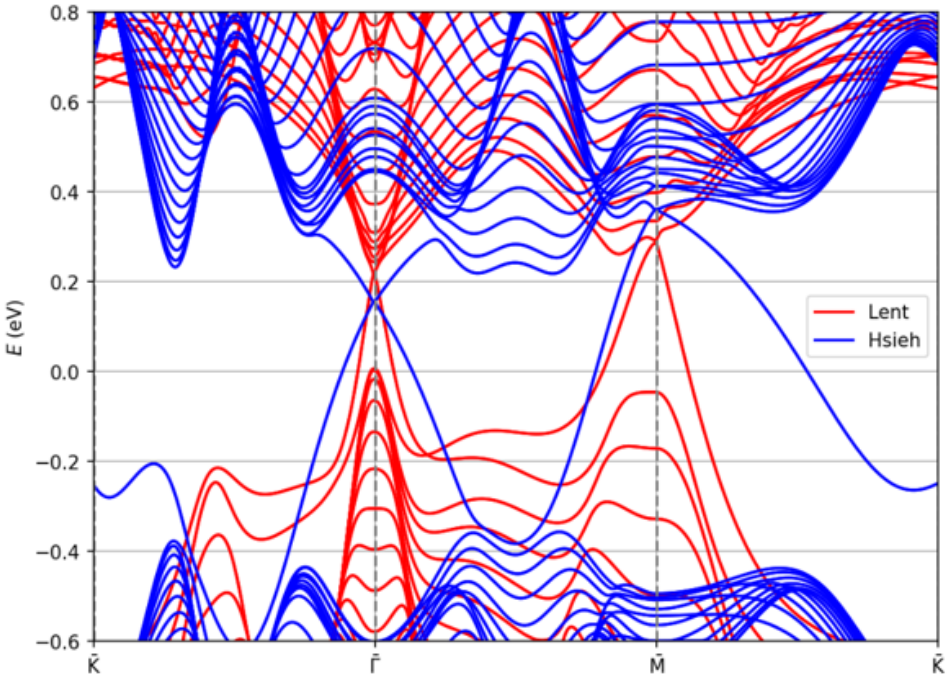

Figure 3.7: Overlayed band structures of the (110) slab for the Hsieh and Lent model.

3.2.3 Penetration depth

As we saw previously, the wave function of the surface state is not completely restricted to the surface of the slab (see Fig. 3.4 & 3.5 (b)). Rather, it decays exponentially into the bulk $\psi = e^{-z/\xi}$, characterized by the penetration depth ξ. By studying the decay of E_g as a function of the number of layers of the slab N_z, we can extract the penetration depth ξ (see eq. 2.13). The penetration depth has been well studied for the Lent model [24, 19], as it helps to determine experimental system sizes for topological behavior. We will also examine it for the Hsieh model, to establish computational boundaries for the nanowire systems we aim to study.

Figure 3.8 (a) shows the finite-size-induced energy gap E_g as a function of the number of layers N_z in the (001) slab. A distinction is made between even (dotted line) and odd (solid line) values of N_z, as these slabs exhibit different symmetries.
Both TB models yield an exponentially decaying energy gap. For the Hsieh model, the decay flattens around $N_z > 40$ due to numerical resolution limits. The Lent model displays a clear even-odd effect, meaning the dotted (N_z even) and solid (N_z odd) follow a distinct oscillatory pattern. These effects are less apparent for the Hsieh model. Exponential fits yield penetration depths of $\xi_{Lent,001} \sim 7$ layers and $\xi_{Hsieh,001} \sim 2$ layers.

Figure 3.8 (b) reveals that the location of the Dirac cone converges quickly to $k = 0.90\ \pi/a$ for the Hsieh model and $k = 0.91\ \pi/a$ for the Lent model.

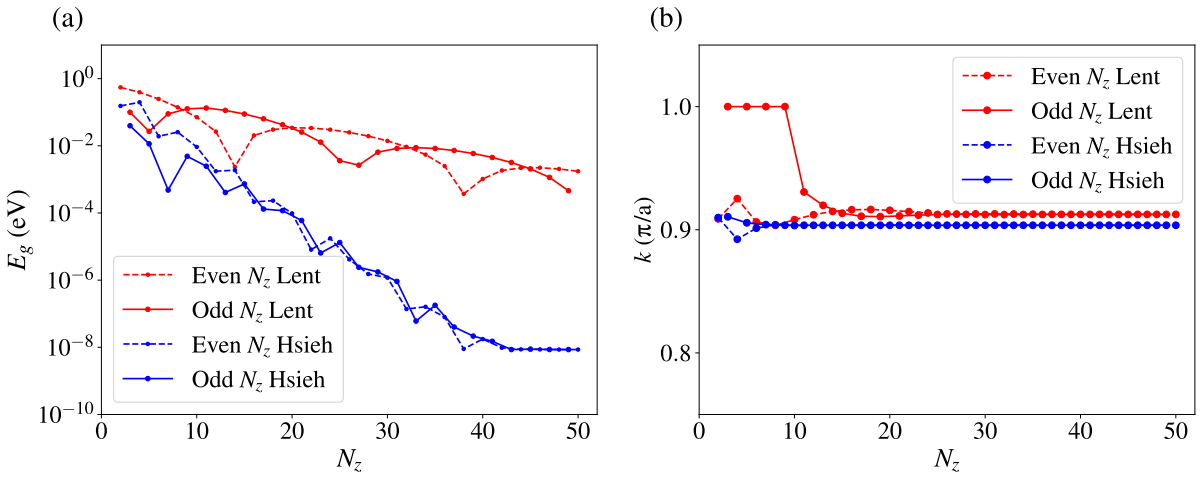

Figure 3.8: (a) Finite-size-induced energy gap E_g as a function of the number of layers N_z in a (001) slab geometry. (b) Position of the Dirac point along the $\bar{\Gamma} - \bar{X}$ line as a function of N_z.

Figure 3.9 (a) shows the finite-size-induced energy gap as a function of the number of layers in the (110) slab. This time an even-odd effect, along with an oscillatory behavior in the energy gap, is observed in both models. Exponential fits yield penetration depths of approximately $\xi_{Lent,110} \sim 7$ and $\xi_{Hsieh,110} \sim 3$ layers, values comparable to the penetration depth of the surface states of the (001) slab. Figure 3.9 (b) shows the position of the Dirac cone along the $\bar{\Gamma} - \bar{Y}$ line as a function of N_z. The Dirac point quickly converges to $k = 0.82\ \pi/a$ for the Hsieh model and $k = 0.91\ \pi/a$ for the Lent model. The difference in the location of the Dirac cone in the BZ can also be seen in Figure 3.6.

To study clear resolved isolated surface states, system size N_z should be at least a couple of times the penetration depth from each boundary, say $N_z/\xi \sim 5$. This means nanowires using the Hsieh model need about 20 layers, while those with the Lent model require around 60. This highlights an important advantage of the Hsieh model, smaller systems can be used to study topological states, reducing the computation time.

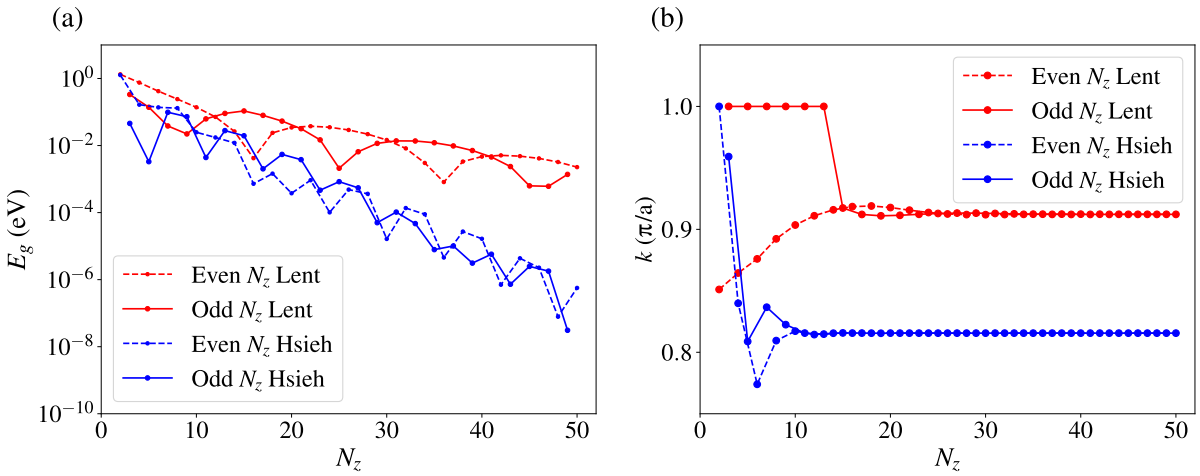

Figure 3.9: (a) Finite-size-induced energy gap E_g as a function of the number of layers N_z in a (110) slab geometry. (b) Position of the Dirac point along the $\bar{\Gamma} - \bar{Y}$ line as a function of N_z.

3.2.4 Spin-momentum locking

Spin-momentum locking refers to the spin orientation being linked to the momentum of an electron. This is a general phenomenon among TI's, arising from strong SOC and symmetries dictating the spin texture. A key feature of this is that electrons traveling in opposite directions (so called time-reversal (TR) partners) have opposite spins, resulting in a helical spin texture. In this section, we will examine the spin texture for the (001) slab.

Figure 3.10 provides a zoomed-in view of the Dirac cone from Figure 3.5 (a). However, here we take a straight path through the BZ, extending into the adjacent BZ to reveal the spin density of the TR partner.
The σ_x component of the spin density is plotted for all bands at $E = -0.05$ eV. Note that TR partners (A & D, B & C) indeed exhibit opposite spin orientation.

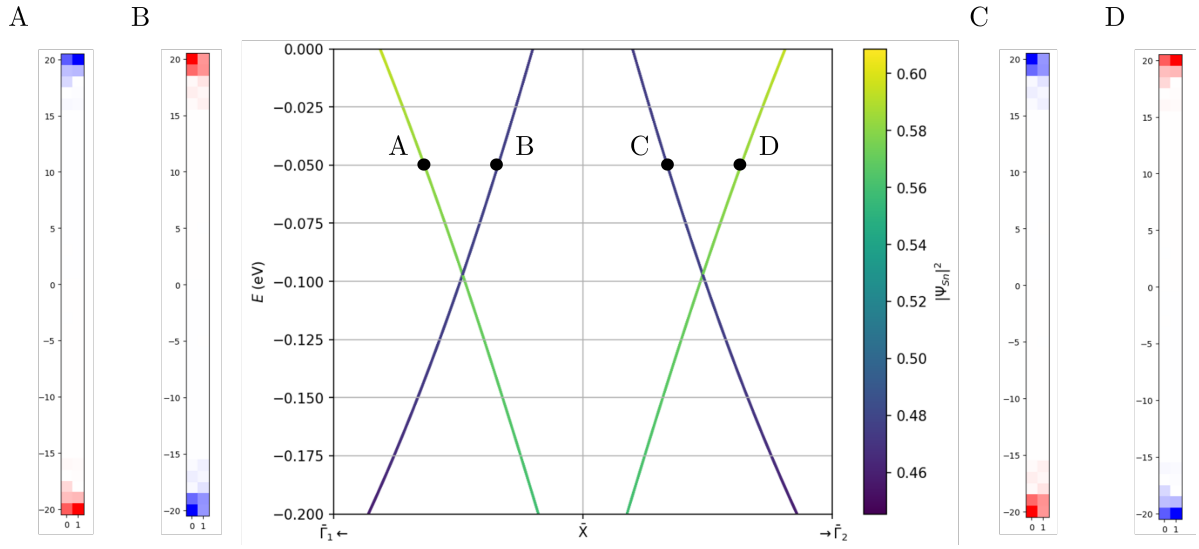

Figure 3.10: Band structure of a (001) slab, zoomed-in on the Dirac cone, obtained using the Hsieh TB model. Spin density plots of the σ_x component for all bands at $E = -0.05$ eV.

Furthermore, the spin direction on the top surface is opposite to that on the bottom surface, consistent with the (symmorphic) mirror symmetry present in the slab with an odd number of layers ($N_z = 41$). Note that a slab with an even number of layers lacks this mirror plane, but retains a (non-symmorphic) glide symmetry. This does not eliminate spin-momentum locking, although the precise spin density is slightly modified due to different symmetry constraints.

The σ_y component of the spin shows a similar structure, but opposite sign relative to σ_x. The out-of-plane spin component (σ_z) is zero, indicating that the spin polarization lies entirely in the plane of the slab. Combining these findings shows that the spin is oriented along $\hat{s} = \pm(\hat{x} - \hat{y})/\sqrt{2}$, which is perpendicular to the momenta on the $\bar{\Gamma} - \bar{X}$ line, pointing along the $(\hat{x} + \hat{y})/\sqrt{2}$ vector.

3.2.5 Topological phase transition

Experimentally growing SnTe is challenging due to Sn vacancies giving rise to bulk conductance. An approach to solve this is growing the ternary $Pb_{1-x}Sn_xTe$, for which selective area growth in nanowires is possible [25].
PbTe is known as a trivial insulator, whereas SnTe is a TCI. Changing alloy composition x results in a topological phase transition [26].

To model $Pb_{1-x}Sn_xTe$, we use the virtual crystal approximation [27]. In this approximation, the bulk unit cell consist of a Te atom and a virtual atom. The properties of the virtual unit cell are linearly interpolated between the SnTe and PbTe tight-binding parameters, based on the stoichiometric mixing ratio x. The PbTe parameters were taken from Lent et al. [9] and used in the Slater-Koster sign convention (see Appendix A1).

Figure 3.11 shows the band structure of a (001) slab (61-monolayers) for a Sn content of $x = 0.2, 0.381, 0.6$ and 1. For $x = 0.2$ (a) the system is in the trivial insulating regime due to the energy gap. At $x = 0.381$, known as the critical composition x_c for bulk $Pb_{1-x}Sn_xTe$ [24], the valence and conduction bands should touch, closing the energy gap. However, due to finite-size effects, the gap remains slightly open. For $x = 0.6$, band inversion occurs, but a small finite-size-induced energy gap persists. Increasing Sn content further to $x = 1$ (SnTe) results in the topological phase, as also shown in Figure 3.4 (a).

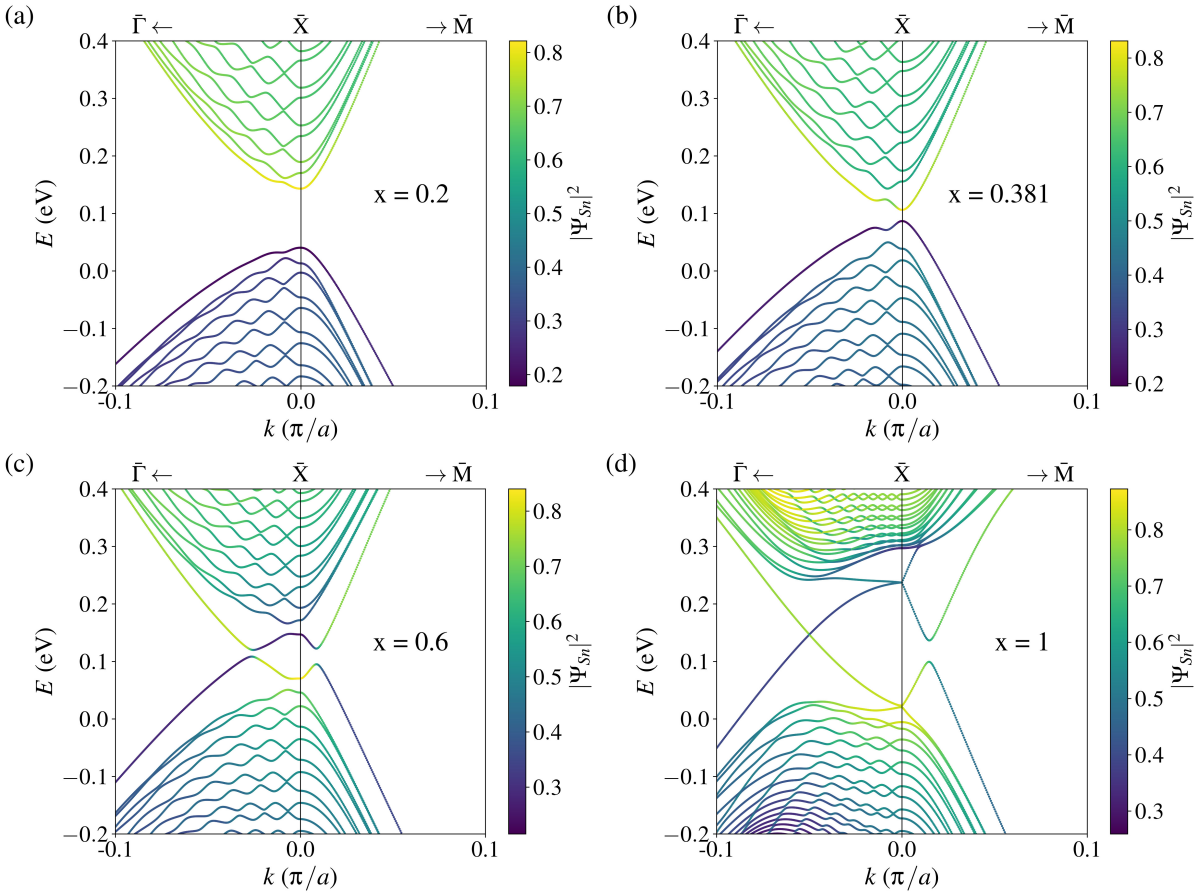

Figure 3.11: Band structures for a $Pb_{1-x}Sn_xTe$ 61-monolayer (001) slab, varying x.

Although the critical composition x_c varies with the slab thickness due to finite-size effects, SnTe shares the same topological phase as $Pb_{1-x}Sn_xTe$ as long as $x > x_c$. Therefore, we believe that the results presented in this thesis on SnTe nanowires will also be applicable to the non-trivial phase of $Pb_{1-x}Sn_xTe$ nanowires. Or in general, the results are applicable for any range of parameters that do not close the bulk energy gap.

4 Nanowires

So far, we have focused on bulk and slab geometries to understand the physics of SnTe. While these provide valuable insights, any practical realization of the material will necessarily be finite. In this context, SnTe nanowires are of particular interest due to their potential applications.

In this section, we examine nanowires with distinct surface terminations. We explore a broad range of phenomena, including their band structure, the emergence of gapless states, the flux response, the influence of strain, spin polarization and corner charge. Additionally, we briefly discuss step edges and rounding off the hinges, which are relevant in experimental settings.

4.1 Nanowire (100)

Figure 4.1 (a) schematically illustrates the (100) nanowire configuration and its cross section (b). The (100) nanowire is infinite along the z- direction, with facets oriented along [100] and [010]. Note that its unit cell consists of two cross sectional layers. The red dotted lines indicate the bulk mirror symmetries that would protect the surface Dirac cones for the related slab geometries. However, in the nanowire, these symmetries are broken by the open boundary conditions along the x- and y-directions. As a result, the corresponding surface Dirac cones are expected to gap out.

Note that some mirror symmetries remain unbroken in the nanowire geometry and continue to protect other topological features. The hinge mirror symmetries, indicated by purple dotted lines (M_{xy} and $M_{x\bar{y}}$), remain preserved. Therefore, we expect the emergence of topologically protected helical hinge states [5].

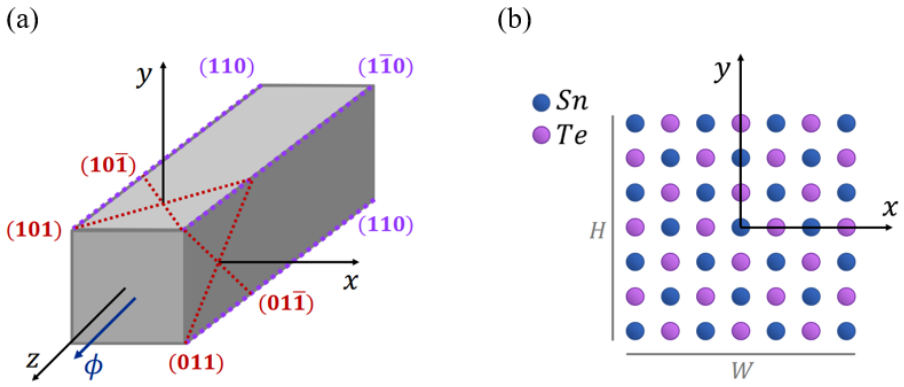

Figure 4.1: Nanowire (100) configuration (a) with cross section (b), images taken from [6].

4.1.1 Band structure

To understand the band structure of the (100) nanowire we need to look back at the slab geometry. The (100) nanowire can be deformed to a slab with [010] (or [100]) surface termination, by replacing the open boundary condition in the x- (or y-) direction with a periodic boundary condition. Therefore, the nanowire can be thought of as a (100) slab which is compactified along one of its translational invariant directions.

Considering a (100) slab with $N = 46$ layers, the spacing in reciprocal space is $\Delta k = \frac{2\pi}{N \cdot a/2} \approx 0.26$ a^{-1}. To obtain the correct 1D Brillouin zone (BZ) projection, we use a slab unit cell with translational invariance vectors $\mathbf{a}_1 = (0, 0, 2)$ and $\mathbf{a}_2 = (0, 2, 0)$. In the slab's 2DBZ, the Dirac cone is located at $k_x = k_y = 0.90\pi$ a^{-1}. The slab's band structure, computed along cuts at $k_x = 0.90\frac{\pi}{a} + n\frac{2\pi}{N \cdot a/2}$ for $n \in \mathbb{N}$, is shown in Figure 4.2 (a). It provides insight into what to expect for the (100) nanowire band structure.

The band structure of the (100) nanowire is given in Figure 4.2 (b). It shows that the surface Dirac cone becomes gapped, due to the breaking of the bulk mirror symmetries near the hinges. Hinge band appear crossing the gap, as they remain protected by the M_{xy} and $M_{x\bar{y}}$ symmetries. These findings are similar to the results from Skiff et al. [6].

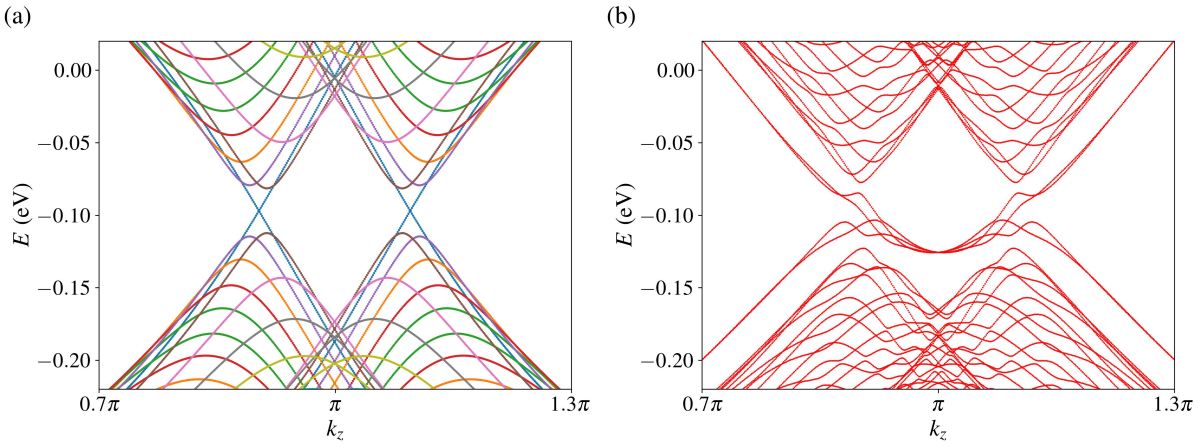

Figure 4.2: (a) Band structure of the (100) slab ($N = 46$ layers) for cuts $k_x = 0.90\frac{\pi}{a} + n\frac{2\pi}{N \cdot a/2}$ for $n \in \mathbb{N}$. (b) Band structure of the (100) nanowire, 46×46 atoms.

Wave functions

Here we will be inspecting how the probability density of the wave functions look like for the gapless states. Since each band is two-fold degenerate, we orthonormalize the states within the degenerate subspace using QR decomposition and sum their probability densities.

Figure 4.4 shows the probability density at three points: A, B & C. Densities A & C can be clearly identified as hinge states, due to the localized probability density in the corners. Around the gapped Dirac cone, the hinge state becomes an extended surface state, matching the results from Skiff et al. [6].

It should be noted that the 46x46 (100) nanowire strictly does not obey C_4 symmetry. Plotting the densities of the total unit cell (i.e. 2 cross-sectional layers) on top of each other, restores the C_4 symmetry in the wave function probability density.

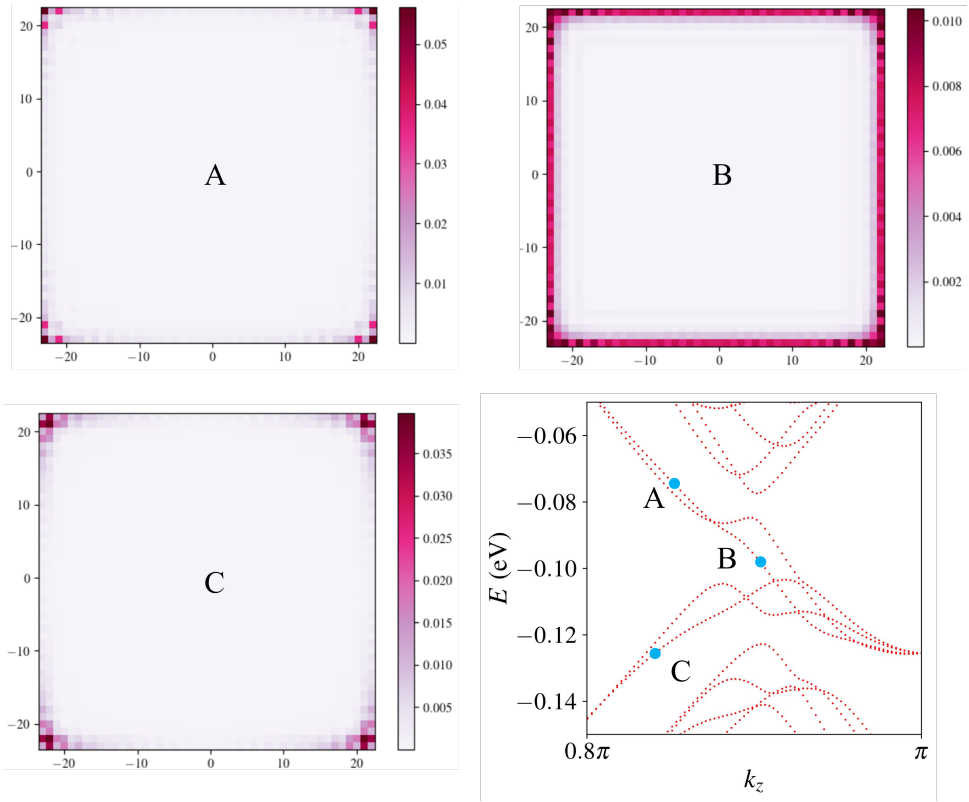

Figure 4.3: Probability densities of the wave functions for points (labeled A-C) indicated by insets in the band structure of the (100) nanowire.

Flux response

Applying a homogeneous magnetic field along the nanowire's axis ($\mathbf{B} = B_0\hat{z}$ with gauge $\mathbf{A} = -B_0 y\hat{x}$) gives rise to a flux through the nanowire. The flux $\phi = BA$, where A is the area of the nanowire, is given in units of the flux quantum $\phi_0 = h/e$.

This reproduces the characteristic band openings and closings between the surface and hinge bands [6]. These gap openings and closings are manifestations of Aharonov-Bohm (AB) oscillations, arising from quantum interference of wave functions encircling the wire perimeter, which acquire flux-dependent phases.

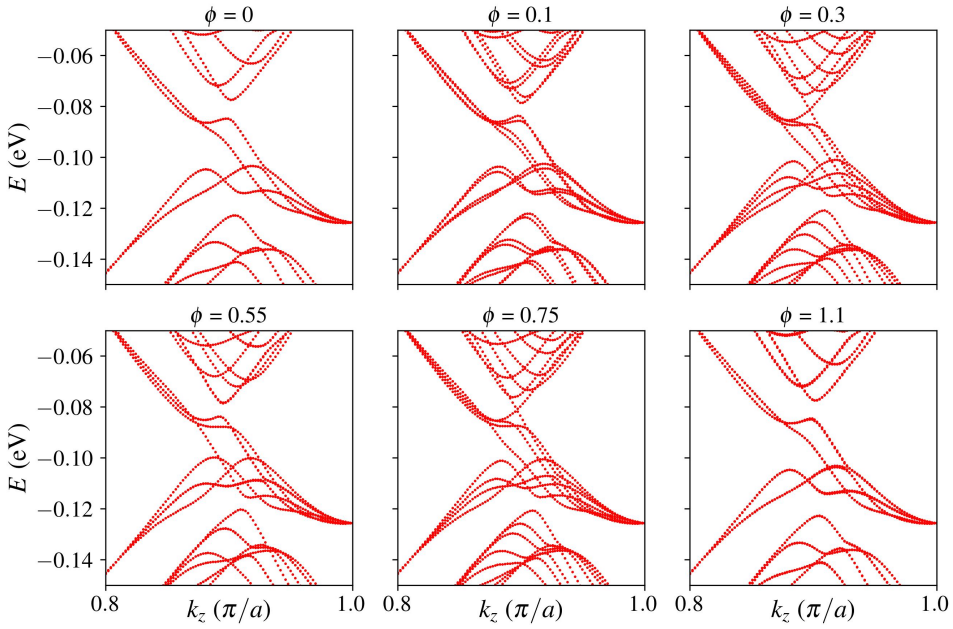

Figure 4.4: Flux response of a 46 × 46 (100) nanowire.

The magnetic field breaks time-reversal symmetry, lifting the two-fold degeneracy of the energy bands. The degeneracy is approximately restored at $\phi = 1.1$, not exactly at a flux quantum as the surface states enclose effectively a smaller area due to their finite penetration depth.

Strain

Although the bulk (110) mirror plane protecting the surface Dirac cones is broken near the corners, extended surface states are still preserved. The topological protection of these surface states can be explicitly broken by applying strain, following a similar approach as Schindler et al. [5].

Using the crystal-field splitting term in eq. 2.15 with $\mathbf{d}_1 = (1,1,0)/\sqrt{2}$ and $\mathbf{d}_2 = (1,-1,0)/\sqrt{2}$, we apply strain along the (110) direction, breaking the mirror symmetries $M_{xz}, M_{x\bar{z}}, M_{yz}$ and $M_{y\bar{z}}$ that protect the surface Dirac cones of the [100] and [010] surfaces. Figure 4.5 (b) illustrates the breaking of topological protection by displaying the (un)protected Dirac cone at $\Delta = 0$ ($\Delta = -0.8$) for the (100) slab. The mirror planes $M_{x,y}$ and $M_{x,\bar{y}}$ protecting the hinge states, remain preserved under strain, as shown in Figure 4.5 (a).

Figure 4.5 (d) shows the band structure of the (100) nanowire, with strain applied along the (110) direction. The hinge states continue to cross the energy gap, consistent with the preservation of M_{xy}, $M_{x\bar{y}}$ symmetries. The sign of strain parameter Δ corresponds to stretching ($\Delta > 0$) and squeezing ($\Delta < 0$) along the given axis. Note that the sign of Δ does not affect the nanowire's band structure.

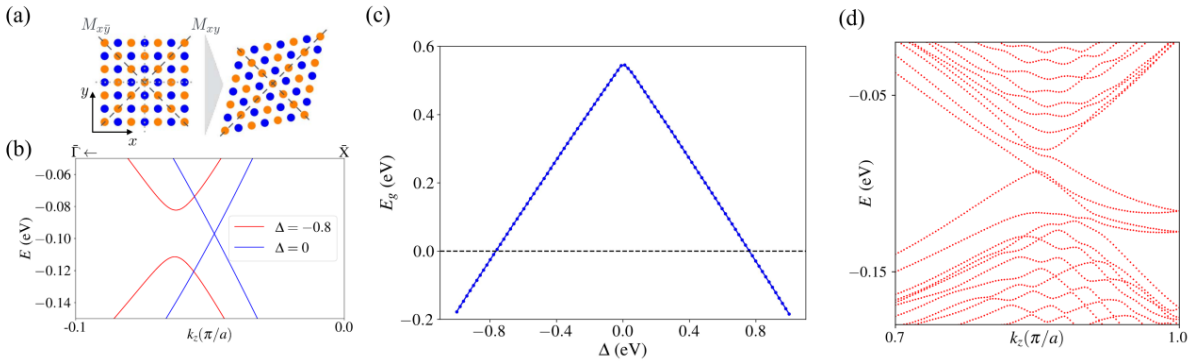

Figure 4.5: (a) Preservation of M_{xy}, $M_{x\bar{y}}$ mirror planes under strain, taken from [5]. (b) Gap opening in the surface Dirac cone of the (100) slab. (c) Bulk energy gap E_g as a function of the strain parameter Δ. (d) Band structure of a 46×46 (100) nanowire at $\Delta = -0.8$.

An interesting question is for what strain strength the system undergoes a topological phase transition. Figure 4.5 (b) shows the bulk energy gap E_g as a function of strain strength Δ. Note that extracting the energy gap from the bulk band structure, which is computed along a high-symmetry path through the BZ, is insufficient here. Strain shifts the location of the energy gap away from this high-symmetry path. Therefore we compute the gap using a grid covering the entire 3DBZ. The bulk band gap closes at $|\Delta_c| = 0.76$, going through a topological phase transition. This also causes the bulk bands in the nanowire's band structure (around $k_z = 0$) to shift into the energy gap, making the 'gapless' states unmeasurable when the strain becomes too large ($|\Delta| > |\Delta_c|$).

For $|\Delta| < |\Delta_c|$, we can argue that states in the unstrained nanowire are protected by the same symmetry as those in the strained nanowire (i.e. $M_{xy}, M_{x\bar{y}}$), since the two systems are continuously connected without closing the bulk energy gap.

Figure 4.6 shows the probability density of the gapless wave function from a hinge band near the surface Dirac cone. For $\Delta = -0.3$ (a), the surface state remains extended despite a slight breaking of C_4 symmetry. Increasing the strain to $\Delta = -0.6$ (b) reveals how the extended surface state localizes into a hinge state as the surface Dirac cone becomes increasingly gapped. Further increasing the strain to $\Delta = -0.9$ (c), going through the topological bulk transition, does not qualitatively change this behavior. Note that for this strain strength, bulk bands are pushed through the energy gap near $k = 0$. The gapped Dirac cone with its hinge bands remain intact, allowing us to identify the 'gapless' state even when the bulk gap is closed.

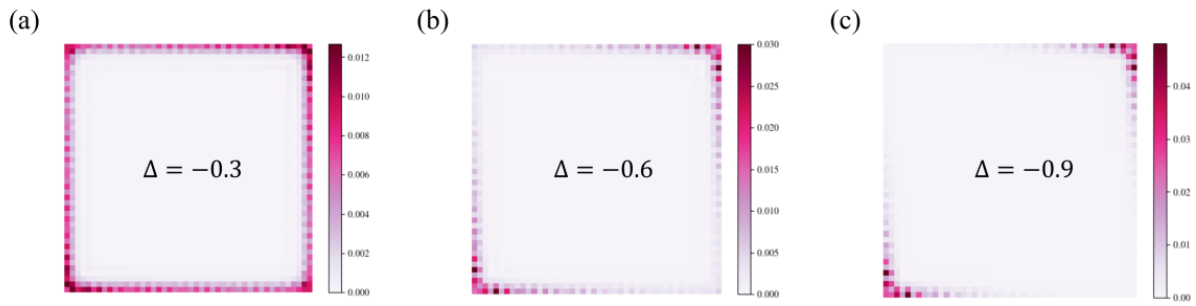

Figure 4.6: Probability density of the gapless wave function from a hinge band near the surface Dirac cone for different strain parameters $\Delta = -0.3, -0.6, -0.9$.

Finite-size effects

Figure 4.7 (a) shows the finite-size-induced energy gap E_g between the valence and conduction bands of the surface Dirac cone, plotted as a function of the square (100) nanowire's side length W (in number of atoms). Increasing the wire's cross-section reduces the gap, as the system approaches the bulk limit. An exponential fit was applied to the data and provided a slightly better fit compared to the $E_g \sim \frac{1}{W}$ dependence.

Naively, one could extract the penetration depth from the exponential fit, yielding $\xi \sim 24$ atoms, similar to our approach for the slab geometry. However, this interpretation is incorrect in the nanowire geometry. Unlike the slab (where surface states are located on opposing top and bottom surfaces), the extended surface states wrap around the full perimeter of the nanowire. As a result, the surface states are not spatially separated as they touch at the hinges, regardless of the side length of the wire. Additionally, hinge bands cross the energy gap, disrupting clean separation between valence and conduction bands. Thus, an exponential fit to $E_g(W)$ does not isolate the penetration depth reliably.

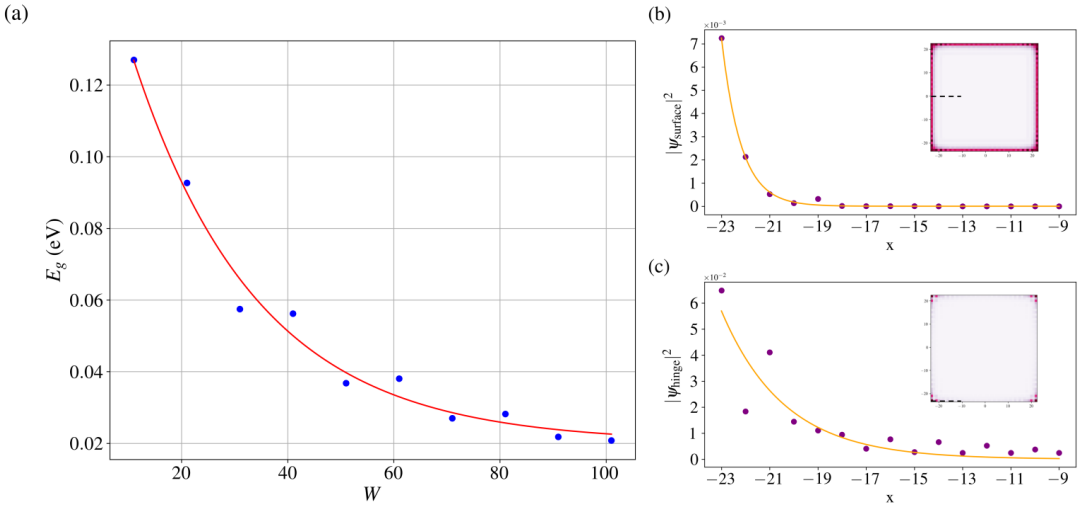

Figure 4.7: (a) Finite-size-induced energy gap E_g between the valence and conduction band for a square (100) nanowire with side length W. (b) and (c) show the probability densities $|\psi|^2$ for the extended surface state and hinge state, respectively, along the path indicated by the black dotted line in the inset.

To still estimate the penetration depth of the extended surface state (Fig. 4.4 B) into the bulk, we analyze the probability density in Figure 4.7 (b), extracted along dotted black line in the inset. Since the probability density of the surface states scales as $|\psi_{\text{surface}}|^2 \sim e^{-2x/\xi_{\text{surface}}}$, we can extract $\xi_{\text{surface}} \sim 2$ atoms, consistent with the penetration depth of the surface states from the (100) slab.

Similarly, we extract the decay length of the hinge state above the Fermi energy, (Fig. 4.4 A) by plotting the probability density along the nanowire edge. This yields $\xi_{\text{hinge, A}} \sim 5$ atoms, indicating weaker localization compared to the surface states decay into the bulk. For the hinge state below the Fermi energy (Fig. 4.4 C), an even larger localization length of $\xi_{\text{hinge, C}} \sim 13$ is found.

Step edge states

Step edges are one-dimensional edge channels giving rise to flat bands. Such states have been both theoretically predicted and experimentally observed in $Pb_{1-x}Sn_xSe$ [28, 29]. They were also predicted in $Sn_{1-x}Pb_xTe_{1-y}Se_y$ for slab geometries [30]. Consistent with these findings, step edge states also emerge in SnTe nanowires.

Figure 4.8 (a) shows the band structure of a 46×46 (100) nanowire, with a single atomic step edge introduced for $y < 0$, as schematically depicted in panel (b). The flat band (labeled A) originates from the step edge. The corresponding wave function's probability density is shown in panel (c).

The presence of a step edge breaks the inversion symmetry, which lifts the degeneracy of the band structure. Since time-reversal symmetry is preserved, two-fold degeneracy is restored at the $k_z = \pi/a$ TRIM point.

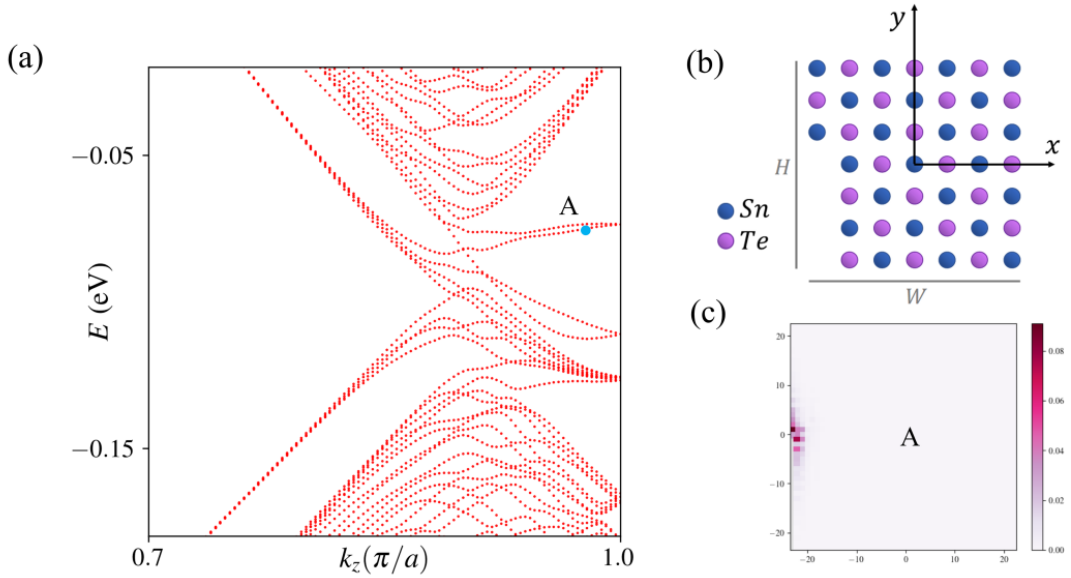

Figure 4.8: (a) Band structure of a 46×46 (100) nanowire with a single atomic step edge for $y < 0$, illustrated in (b). The probability density of the step edge wave function (labeled A) is shown in (c).

Rounding off the hinges

Up until now, sharp (90°) corners have been considered. In this section, we investigate how the band structure evolves when these corners are gradually rounded.

Figure 4.9 shows the band structures for various radii. A schematic illustration of the cross-sectional shape of the nanowire is depicted as well. For the given band structures, the rounding radii r (atoms) are reaching up to $r/W \sim 0.1$. When $r \neq 0$, the hinge bands become noticeably flatter within the energy gap, reminiscent of the behavior seen at step edges. This is due to the discrete nature of the crystal structure, making rounded hinges resemble multiple step edges.

When the rounded hinges start becoming more significant $r/W \gtrsim 0.2$, the energy gap closes. The hinge states remain present, but become effectively unmeasurable.

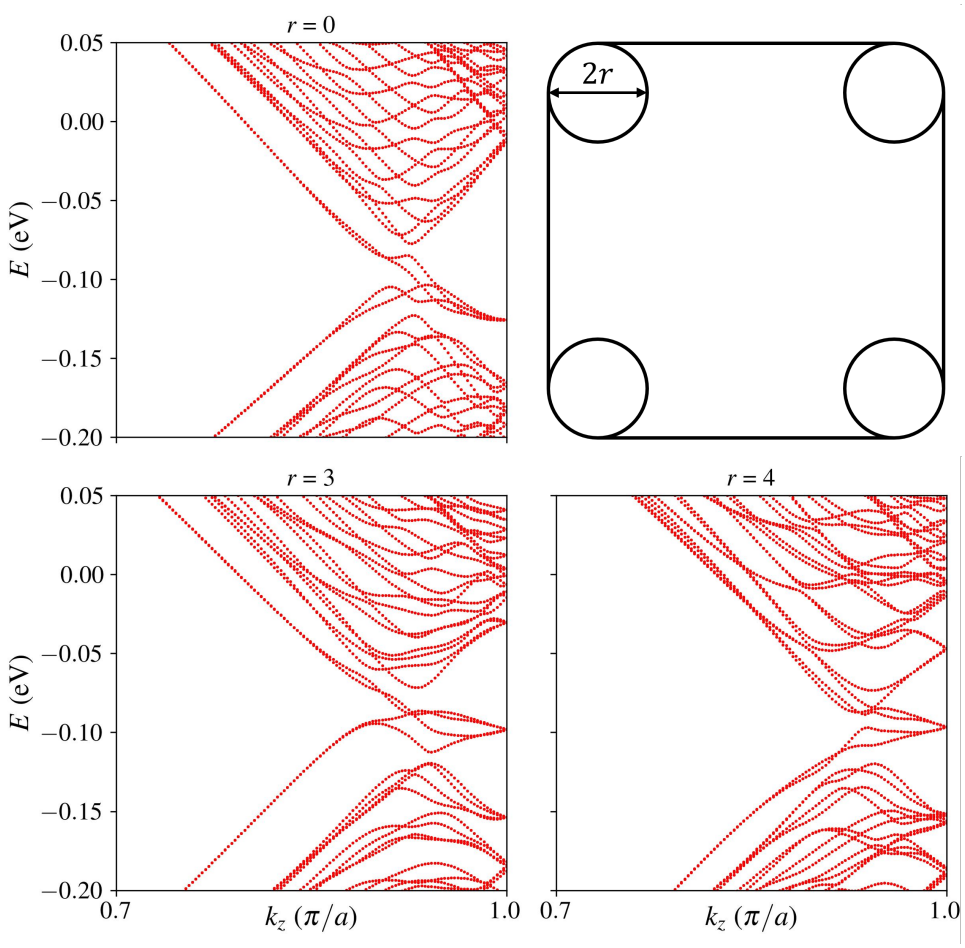

Figure 4.9: Rounded hinges in a 46 × 46 (001) nanowire, for radii r given in atoms.

4.1.2 Spin polarization

Spin is an axial vector, meaning that under a mirror operation, only the component parallel to the plane changes sign. The mirror planes of the cross section (Figure 4.1 (b)) are M_x, M_y, M_{xy} and $M_{x\bar{y}}$. The (non-trivial) spin texture consistent with all these mirror symmetries is a rotational pattern, shown in Figure 4.10 (a).

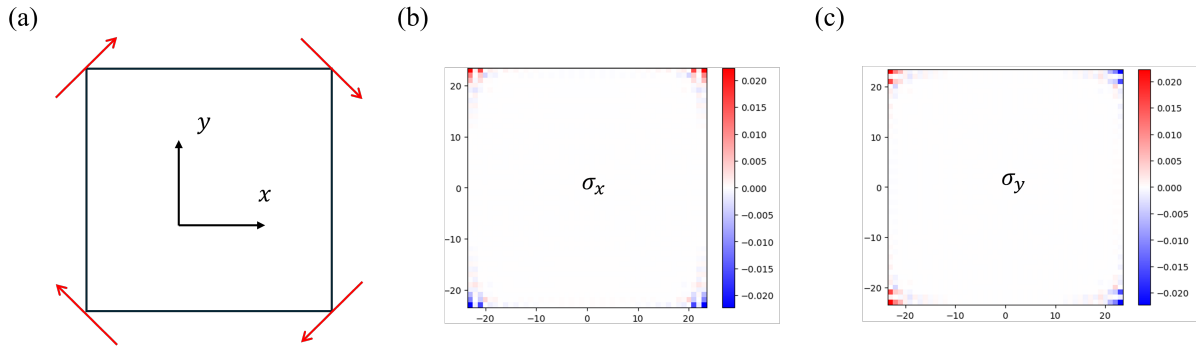

Figure 4.10: Spin texture for nanowire (100) configuration (a), with spin density component σ_x (b) and σ_y (c).

Figures 4.10 (b) and (c) show the σ_x and σ_y components of the spin density, respectively, for the hinge state from Fig. 4.4 A. Taking a superposition of these spin components reproduces the full spin texture. The time-reversal partner of this state has spin polarization in the opposite direction. The σ_z component is not shown, as it is zero.

4.1.3 Corner charge

The localization of the gapless hinge states at the corners of the nanowire give rise to corner charge Q_c. Since the conduction and valence band are connected by the hinge bands, we have a different number of states below the Fermi level (at half-filling) at $k_z = 0$ with $k_z = \pi/a$.

The probability density at a specific k-point is defined as:

$$\rho_{k_z}(\mathbf{r}) = \sum_{n:E_n<E_F} |\psi_{n,k_z}(\mathbf{r})|^2 \tag{4.1}$$

By comparing the densities at $k_z = 0$ (ρ_0) with $k_z = \pi$ (ρ_π), the excess charge localized at the corners can be identified as the corner charge: $Q_c = \rho_\pi - \rho_0$. This identification reflects the bulk-boundary correspondence in higher-order topological insulators. Additional details for the extraction of corner charge are given in the Appendix A3.

Figure 4.11 (a) shows the resulting corner charge distribution for a 21×21 (100) nanowire. The excess charge is clearly localized in the corners and decays away from them. To quantify this decay, we enclose each corner in a square box of side length l and compute the summed charge within the box. The summed corner charge as a function of l is plotted in 4.11 (b) and fitted using exponential function $\sum Q_c = 1 - e^{(-0.28l)}$. The fit is expected to become more accurate with increasing system size. Summing over the entire cross section yields a total corner charge of $Q_c = 4e$, consistent with four in-gap states crossing the Fermi level.

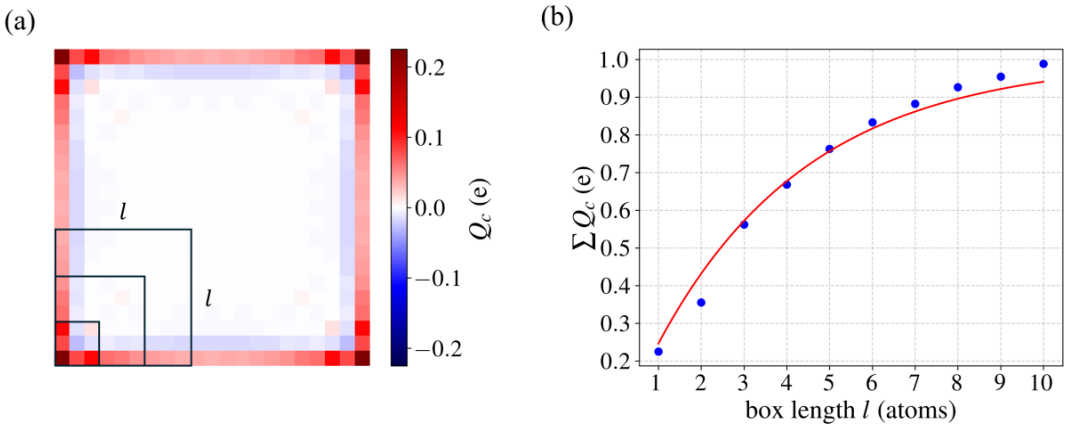

Figure 4.11: (a) Corner charge distribution Q_c for a 21×21 (100) nanowire. (b) Summed corner charges as a function of box length l, fitted exponentially.

The robustness of the hinge bands to size effects, strain and flux, along with their spin polarization and corner charge, confirms the intrinsic higher-order topological nature of the (100) nanowire.

4.2 Nanowire (110)

Now that we have analyzed the electronic properties of the (100) nanowire, we turn our attention to a nanowire with a different surface termination. Since the {110} mirror planes possess a non-zero mirror Chern number, it is natural to investigate a nanowire terminated along this orientation.

Figure 4.12 (a) illustrates the so called (110) nanowire configuration, with its cross-sectional view shown in panel (b). Note that the nanowire remains translationally invariant along the z-axis, only the shape of the cross section is changed compared to the (100) nanowire.

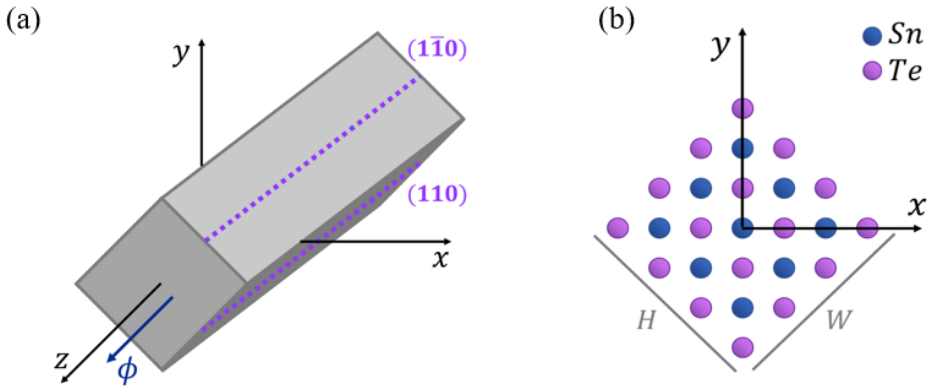

Figure 4.12: Nanowire (110) configuration (a) with cross section (b), images taken from [6].

The (110) nanowire is made up of facets with surface terminations in the [110] and [1$\bar{1}$0] planes. Note that the system is infinite in the z- direction. The unit cell consists of two cross-sectional layers, with atoms alternating from Sn to Te in subsequent layers, removing any atom-type dependency in the size of the wire.

4.2.1 Band structure

To understand the band structure of the (110) nanowire, we recognize the wire as a (110) slab, compactified along the $\hat{\mathbf{e}}_1 = (\hat{\mathbf{e}}_x + \hat{\mathbf{e}}_y)/\sqrt{2}$ direction. Considering a (110) slab with thickness $N = 54$ layers and taking cuts through its 2DBZ at $k_1 = n\frac{2\pi}{N \cdot a/2}$ for $n \in \mathbb{N}$, reveals the band structure shown in Figure 4.13 (a). The two main features are the Dirac cone and avoided crossing. The Dirac cone is located at $k_z = 0.82\ \pi/a$, originating from the $\bar{\Gamma} - \bar{Y}$ line (i.e. $k_1 = 0$) in the 2DBZ of the (110) slab. The avoided crossing is located at $k_z = 0.54\ \pi/a$, originating from the $\bar{X} - \bar{S}$ line (i.e. $k_1 = \pi/a$), which is not protected by (110) mirror plane, resulting in an avoided crossing.

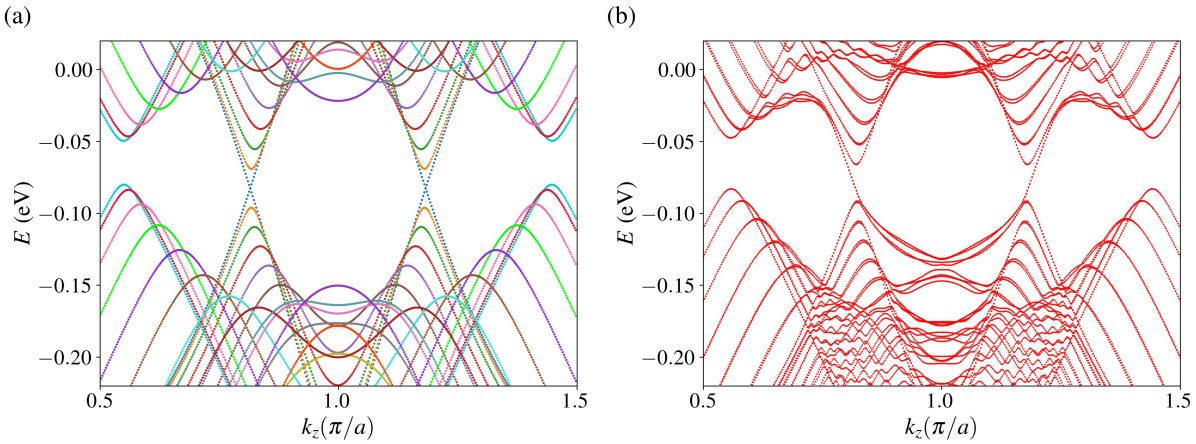

Figure 4.13: (a) Band structure of the (110) slab ($N = 54$) for cuts $k_1 = n\frac{2\pi}{N \cdot a/2}$ for $n \in \mathbb{N}$. (b) Band structure of the (110) nanowire, with 28×28 atoms in its outermost layer.

Figure 4.12 (b) shows the band structure of the (110) nanowire, with 28×28 atoms in its outermost layer. Note that this size is related to its thickness along the x-axis by $\frac{W}{2} + 1$. The spectral flow at the Dirac cone indicates gapless states connecting the conduction and valence bands. However, the presence of an avoided crossing complicates the interpretation, as it hybridizes potential hinge modes with bulk states, preventing a clear identification of the potential hinge bands.
The bands are two-fold degenerate, although it is hard to see from the band structure, two two-fold degenerate bands cross the energy gap, resulting in 4 gapless states in total.

Wave functions

Focusing on states around the Fermi energy, we examine the probability densities of the wavefunctions, shown in Figure 4.14. States at the avoided crossing (A) show confinement to each facet of the nanowire. Gapless states (B) show confined surface states as well, though there is still weak coupling between the states belonging to different facets of the wire. Moving further away from the gapped Dirac cone (C), the states regain there 1D character as hinge states.

Although the M_x, M_y symmetries are trivial, in the sense that mirror Chern number $C_m = 0$, localized hinge states are still observed. We will later examine them further by applying strain. First, we study the effect of the confinement to the flux response of the (110) nanowire.

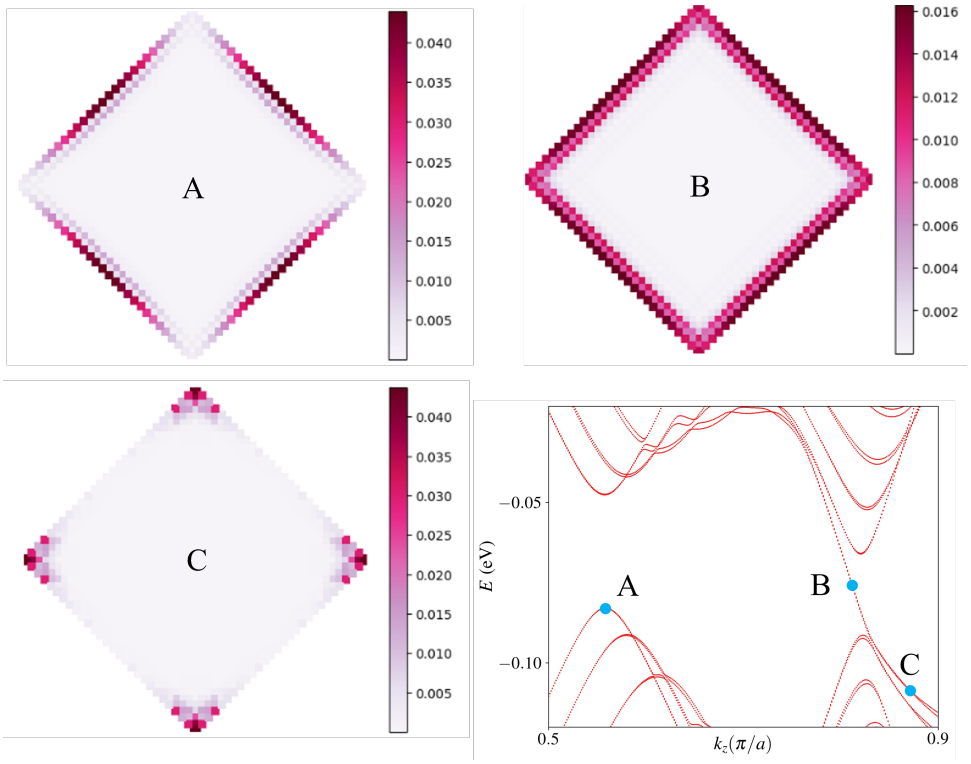

Figure 4.14: Probability densities of the wave functions for points (labeled A-C) indicated by insets in the band structure of the (110) nanowire.

Flux response

Figure 4.15 shows the flux response of the low-energy states for the (110) nanowire. The degeneracy of these states is completely lifted at $\phi = 0.3$, partially restored at $\phi = 0.5$ and fully recovered at $\phi = 1.1$ This behavior is typical for four weakly coupled sites connected in a circle, as described by Skiff et al. [6]. For the (110) nanowire, these 'sites' correspond to confined surface states, which are weakly coupled through tunnel barriers at the nanowire hinges.

No gap closings or openings are observed, indicating the absence of Aharonov–Bohm (AB) oscillations. This is consistent with the states not strongly encircling the nanowire's cross section, in contrast to the behavior of the extended surface states in the (100) nanowire. The flux dependence of a broader portion of the band structure is presented in appendix A2.

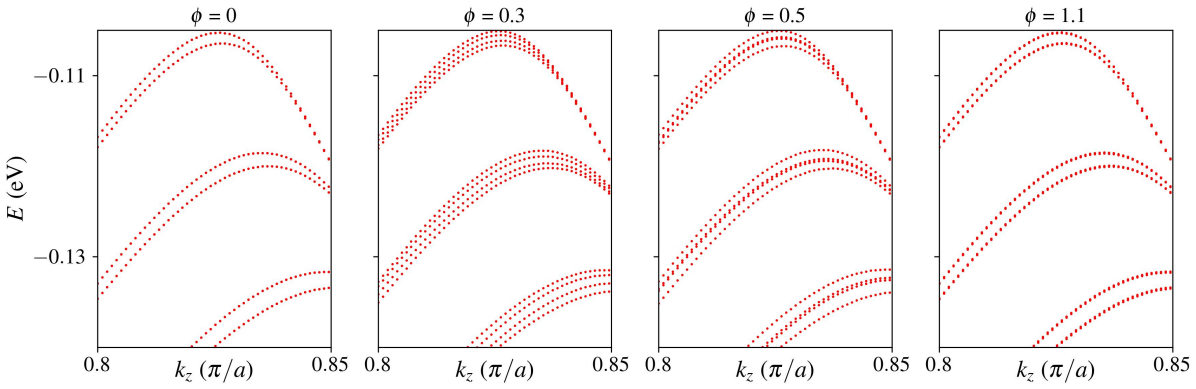

Figure 4.15: Flux response of the weakly coupled confined surface states for a 28×28 (110) nanowire.

Strain

To determine whether the gapless states truly belong to hinge bands, or are part of the surface Dirac cone, we observe if they are robust against strain. The (110) nanowire has facets along the [110] and $[1\bar{1}0]$ directions. Applying strain along the (110) direction (as was done for the (100) nanowire) does not open the surface Dirac cone, but instead shifts it into the bulk bands, since the crystal field splitting term act as an onsite potential.

In order to gap out the [110] and $[1\bar{1}0]$ surface Dirac cones, while preserving the mirror symmetry of the hinges (M_x, M_y), we apply strain along the $\mathbf{d}_1 = (1,0,0)$ and $\mathbf{d}_2 = (0,1,0)$ axis. It was confirmed that this does open the surface Dirac cone for the (110) slab.

Figure 4.16 shows the band structure of the strained (110) nanowire, for strain parameter $\Delta = -0.4$. We observe that the gapless state (labeled by A), corresponds to a hinge state. Following the hinge band, we see that localization tends to increase when we move away from the gapped Dirac cone. Since the hinge band remains gapless under strain, we conclude that the gapless states indeed originate from hinge bands, rather than the nearby surface Dirac cone. However, the hinge bands do not appear to be protected by the mirror symmetries of the [110] and $[1\bar{1}0]$ facets, as these are broken.

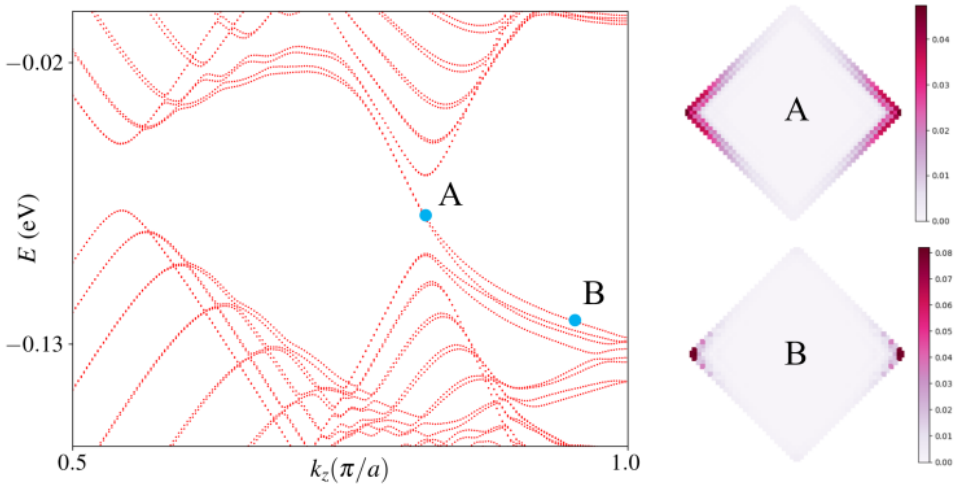

Figure 4.16: Band structure of the strained (110) nanowire for $\Delta = -0.4$. Probability densities of the wavefunctions labeled by A and B are shown.

The avoided crossing shifts up in energy if strain is applied. For small strain values, it remains outside the energy gap. However, around $\Delta = -0.8$ the avoided crossing is pushed up through the energy gap, such that the hinge states become unmeasurbable.

4.2.2 Spin polarization

Figure 4.17 (a) shows the spin texture of the confined surface states in the (110) nanowire configuration, constrained by the mirror symmetry planes of the unit cell. Panels (b) and (c) present the σ_x and σ_y components of the spin density, respectively, for the confined surface state from Figure 4.14 B. Again, the σ_z component is not shown, as it is zero.

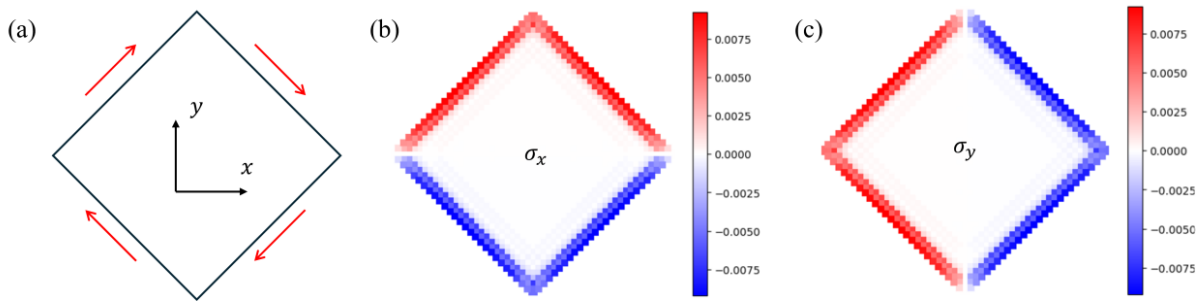

Figure 4.17: (a) Spin texture of the confined surface states for the nanowire (110) configuration, (b) spin density component σ_x and (c) σ_y.

4.2.3 Corner charge

Using the same algorithm outlined earlier for the (100) nanowire, we can compute the corner charge of the (110) nanowire. Due to computational limitations, we focus on a relatively small system size of 16×16 atoms.

Figure 4.18 shows the corner charge density Q_c for the (110) nanowire. Summing all corner charge contributions of the individual atoms yields Q_c = 4 e, consistent with four bands crossing the Fermi energy. Figure 4.18 (b) presents the summed corner charge contributions within a square box of size $l \times l$ atoms. The data is fitted by the exponential fit curve $\sum Q_c = 1 - e^{-0.41l}$, the fit is expected to become more accurate for larger system sizes.

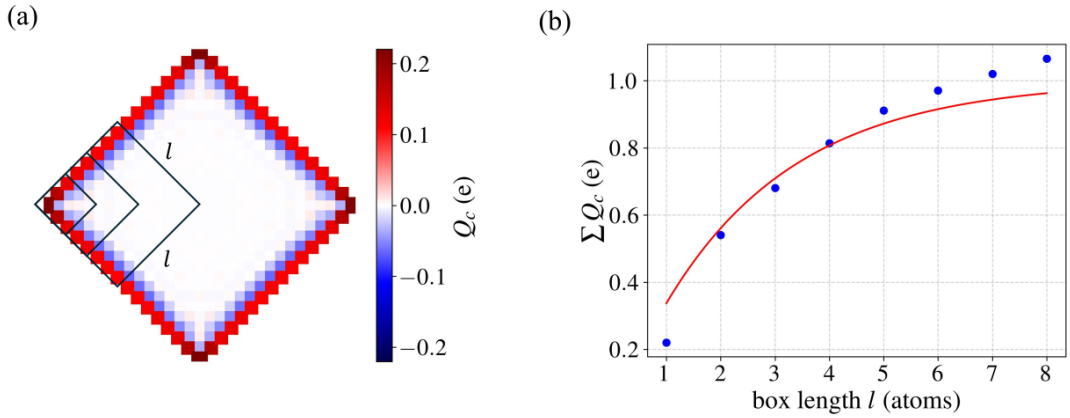

Figure 4.18: (a) Corner charge distribution Q_c for a 16×16 (110) nanowire. (b) Summed corner charges as a function of box length l, fitted exponentially.

The robustness of the hinge bands under strain and flux, combined with their spin polarization and corner charge, establishes the (110) nanowire as an intrinsic higher-order topological insulator.

4.3 Nanowire (101)

The (100) nanowire breaks bulk mirror symmetries (specifically (101), $(10\bar{1})$, (011) and $(01\bar{1})$) around its corners. Now we study a nanowire with the same cross section as the (100) wire (Fig. 4.1 (b)), but with translational invariance $\mathbf{a} = (0, 1, 1)$, such that its surface terminations are [011] and [100]. Since these surface terminations are of a different type, the nanowire respects C_2 symmetry (instead of C_4). Effectively, this nanowire can be viewed as a hybrid of the (100) and (110) nanowires discussed previously. We refer to this structure as the (101) nanowire.

Figure 4.19 (a) shows the band structure of a 46×46 atoms (101) nanowire. Where k_1 is the momentum along the direction defined by unit vector $\mathbf{e}_1 = (\mathbf{e}_y + \mathbf{e}_z)/\sqrt{2}$. Gapless states appear around $k_1 = 0.9\ \pi/a$, while an avoided crossing is observed at $k_1 = 0$.

The cross section is illustrated in the inset (not to scale). Note that the unit cell only consists of a single cross-sectional layer, leading to a strong atom-type (Sn/Te) dependency. For an even side length, diagonally opposite corners are of the same atomic type, whereas for an odd side length all corners are identical.

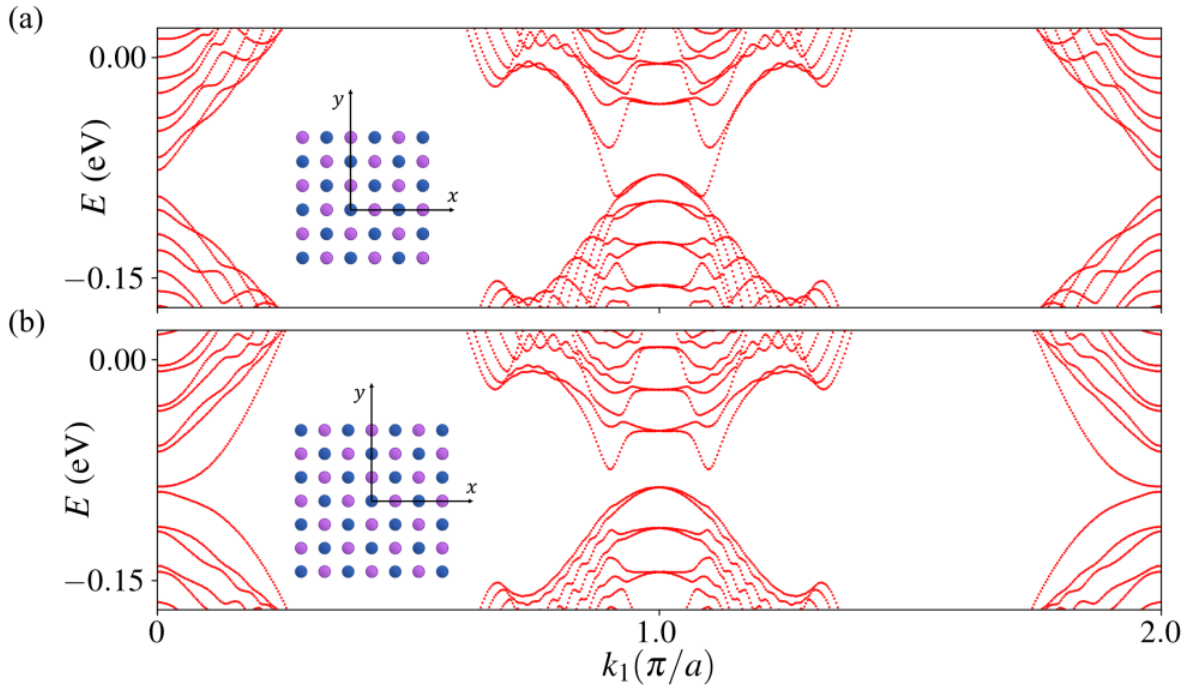

Figure 4.19: (a) Band structure of the (101) nanowire, with facets along [011] and [100]. The cross section is of even side length 46×46 atoms, illustrated (not to scale) by the inset. Momentum k_1 is along the $\mathbf{e}_1 = (\mathbf{e}_y + \mathbf{e}_z)/\sqrt{2}$ unit vector. (b) Band structure of the (101) nanowire for an odd side length of 47×47 atoms.

Figure 4.19 (b) shows the band structure for an odd side length of 47×47 atoms. In this case, the gapless states are no longer present. Instead, parabolic states appear at $k_1 = 0$, which do not connect the valence and conduction band by spectral flow, as these remain separated by a finite energy gap.

The absence of gapless states for an odd number of atoms persists even at larger system sizes. Due to this extrinsic behavior, we chose not to further investigate this (101) nanowire configuration.

5 Quantum transport

Having developed a detailed understanding of the electronic properties of the (100) and (110) SnTe nanowire configurations, we turn our attention to their quantum transport behavior.

We will examine transport in two configurations: the longitudinal (forward) direction, where leads are connected along the axis of the nanowire; and the transverse direction, where leads are connected perpendicular to the nanowire's axis. In both cases, we investigate the effect of threading a magnetic flux parallel to the nanowire's axis. The goal of this section is to identify quantum transport signatures that are characteristic for SnTe nanowires with (100) and (110) surface termination.

5.1 Longitudinal

Analyzing transport provides a connection between the electronic band structure and experiments. As conductance and its effect under a magnetic field, can be measured in experimental settings. In this section we will examine the conductance, its flux response and visualize the current flowing through the nanowires.

Scattering regions in the longitudinal direction are scalable in their length. This makes longitudinal transport especially suitable for studying disorder effects, such as Sn/Te vacancies, surface roughness or electrostatic/magnetostatic inhomogeneities.
In principle, higher-order Fabry–Pérot interference effects can also be explored. For example, by attaching leads to individual hinges and analyzing the resulting interference patterns [31]. However, such studies require hinge states to be sufficiently decoupled, which demands simulating wider nanowires. These longitudinal transport systems are not very scalable in their width. While the TB Hamiltonian of the scattering region involves sparse matrices, the leads (whose dimensions depend solely on the width) involve dense matrix operations. Therefore, we limit our analysis to systems with relatively small nanowire cross sections.

The computational limit for longitudinal transport systems appeared to be around $W \sim 20$ atoms. At this width, surface states are expected to be well separated since $W/\xi_{\text{surface}} \sim 10$. However, hinge states exhibit significant overlap, with $W/\xi_{\text{hinge, A}} \sim 4$ and $W/\xi_{\text{hinge, C}} \sim 2$ (see Fig. 4.7).

5.1.1 Nanowire (100)

We study a (100) nanowire with a cross section of 11×11 atoms. This small cross section introduces a relatively large finite-size-induced energy gap and stronger coupling between hinge states. Nevertheless, the topological features like hinge bands, hinge states, extended surface states, gap openings and closings with magnetic fields, remain intact. Therefore, this system still provides reliable insight into the conductance and Aharonov-Bohm (AB) oscillation signatures that we are looking for.

Aharonov-Bohm oscillations

To build intuition for the transport calculations, we first consider a nanowire connected to SnTe leads, effectively modeling an infinite nanowire.

Figure 5.1 (a) shows the scattering region (SnTe) in blue and a few unit cells of the leads (also SnTe in this case) in red. A homogeneous magnetic field is applied parallel to the nanowire axis. Figure 5.1 (b) displays the energy-dependent conductance through the nanowire for magnetic flux values $\phi = 0$ and $\phi = 0.475$, in units of the flux quantum $\phi_0 = h/e$. The conductance remains finite within the bulk energy gap due to the presence of topologically protected gapless states. Figure 5.1 (c) shows the band structure within the energy gap of the (100) nanowire for the same flux values.

The conductance is determined solely by the number of available propagating modes (i.e. channels) at a given energy. Each mode contributes a quantized unit of conductance e^2/h, resulting in discrete step-like increases. Due to the absence of disorder or interfaces between different materials, there is no mode mixing or backscattering, resulting in perfectly transmitted modes.

At $\phi = 0$, the bands are two-fold degenerate, leading to conductance steps that are multiples of $\Delta G = 2e^2/h$. When $\phi \neq 0$, time-reversal symmetry is broken, lifting the two-fold degeneracy. As a result, the step size reduces to $\Delta G = e^2/h$.

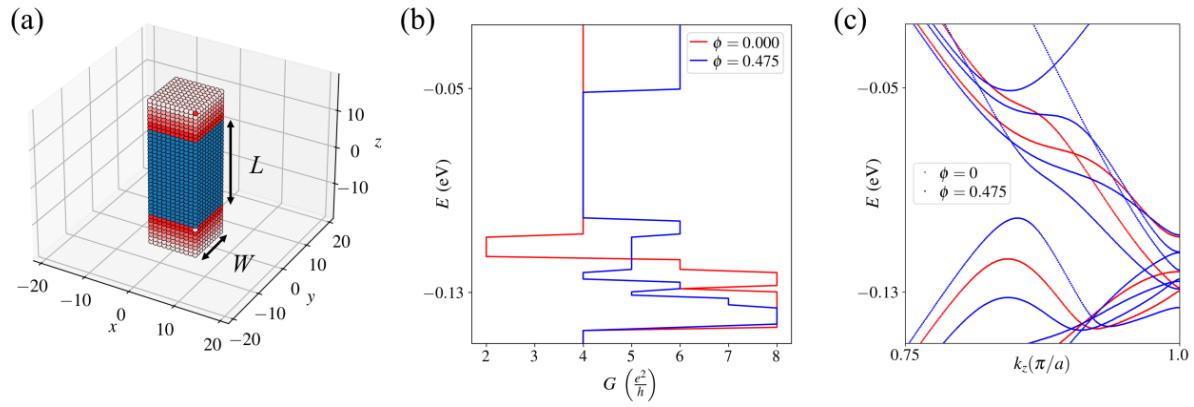

Figure 5.1: (a) Longitudinal transport system, the scattering region shown in blue and a few lead unit cells in red. (b) Conductance in the energy gap at $\phi = 0$ and $\phi = 0.475$. (c) Band structure corresponding to the 11×11 (100) nanowire.

Since the gap openings and closings occur near $E = -0.04$ eV, we take a closer look at this fixed energy to examine whether the conductance oscillation persists when metallic leads are attached. The result is shown in Figure 5.2 for a scattering region of $L = 131$ layers. For comparison, the case with SnTe leads is also included. Although the case with metallic leads does not exhibit perfectly quantized conductance steps, as modes in the lead and scattering region do not perfectly match anymore, a clear peak in conductance remains visible. This feature is robust and could, in principle, be observed in experiments using gate voltage control over the chemical potential. Appendix A4 discusses a similar plot for a wider ϕ range.

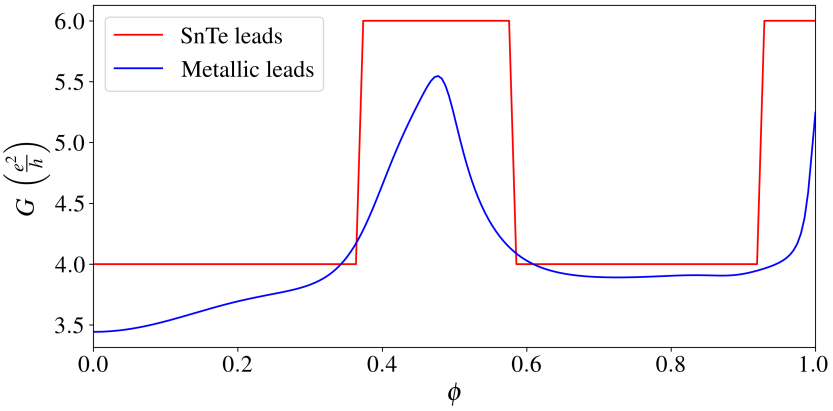

Figure 5.2: Conductance at fixed energy $E = -0.04$ eV as a function of magnetic flux ϕ for an 11×11 (100) nanowire with $L = 131$ layers connected to metallic leads. The result for SnTe leads is shown for reference.

In this simulation, the metallic leads are modeled as a collection of one-dimensional disconnected wires. This configuration results in a cosine band structure for the leads, where the degeneracy is determined by the number of degrees of freedom in the unit cell of the lead. This approach was chosen to avoid complications that arise when introducing magnetic flux in metallic leads with transverse hopping. In such cases, the flux causes the cosine bands to shift, altering the number of propagating modes in the leads at fixed energy.

Experimental parameters

To provide physical intuition for the relevant magnetic field strengths and their connection to experiments, we examine the relationship between the flux ϕ and the corresponding magnetic field B:

$$B = \frac{4h\phi}{e(aW)^2} \tag{5.1}$$

where $a = 6.31$Å is the lattice constant of SnTe and W the nanowire cross-section width (in units of atomic spacings). The factor of 4 in the numerator arises because the unit cell contains 2 atoms and the area scales as a^2, effectively giving $2 \times 2 = 4$ when expressed in terms of unit cell width.

For an 11×11 (100) nanowire, a single magnetic flux quantum ($\phi_0 = h/e$, i.e. $\phi = 1$) corresponds to a magnetic field of approximately $B \sim 400$ T.
Typical vapor–liquid–solid (VLS) grown nanowires have a width of around 80 nm [32], corresponding to a cross section of roughly 250×250 atoms. For such a wire, threading a single flux quantum through the nanowire would require a magnetic field of approximately 2.6 T, a value that qualifies as high but remains accessible under standard laboratory conditions.
Fabricating thinner nanowires reduces their magnetic flux response (assuming there is an experimental limit in the applied magnetic field), making AB oscillations more difficult to detect. Since inserting more than one flux quantum through the nanowire cross section requires even stronger fields, we restrict our analysis to the regime of a single flux quantum.

When the wire width W approaches the coherence length ξ, gapless states hybridize. To clearly resolve 1D hinge states, the wire width should satisfy $W >> \xi$.
The penetration depth of the surface states extracted from the Lent model (see Fig. 3.8) sets a lower bound near a 70×70 atomic cross section, corresponding to a nanowire width of approximately 22 nm. This ensures that $W/\xi_{\text{Lent, 001}} \sim 10$, which is sufficient to clearly resolve the surface states.

For the Hsieh model, the penetration depth of the hinge state was found to be up to seven times larger compared to the penetration depth of the surface states ($\xi_{\text{Hsieh,001}}/\xi_{\text{hinge,C}} \sim 7$).
There is no reason to expect significantly different behavior for the Lent model. Although we did not explicitly extract the penetration depth of the hinge state for nanowires simulated using the Lent model, we estimate the upper bound of the penetration depth of the hinge states to be approximately $\xi_{\text{hinge, Lent}} \sim 7 \cdot \xi_{\text{Lent, 001}} \sim 50$ atoms.

Currently VLS grown nanowires would have $W/\xi_{\text{hinge, Lent}} \sim 5$, which should be sufficient to observe well-separated hinge states. However, attempting to fabricate thinner wires is not recommended, as this causes hybridization of the hinge states and suppression of the flux response.

Current visualization

To understand how the current flows through the nanowire, we visualized the current density at $\phi = 0$. Figure 5.3 shows the current flowing through one of the facets of a (100) nanowire for a hinge state at $E = -0.040$ eV. At a slightly lower energy, $E = -0.065$ eV, the surface states become extended again, as shown in panel (b).

To probe the current distribution through the nanowire's cross section, we computed the total current flowing between two adjacent nanowire layers, from $z = 0$ to $z = 1$. The corresponding current density plot reveals localized hinge modes at $E = -0.040$ eV (panel (c)) and extended surface states at $E = -0.065$ eV (panel (d)).

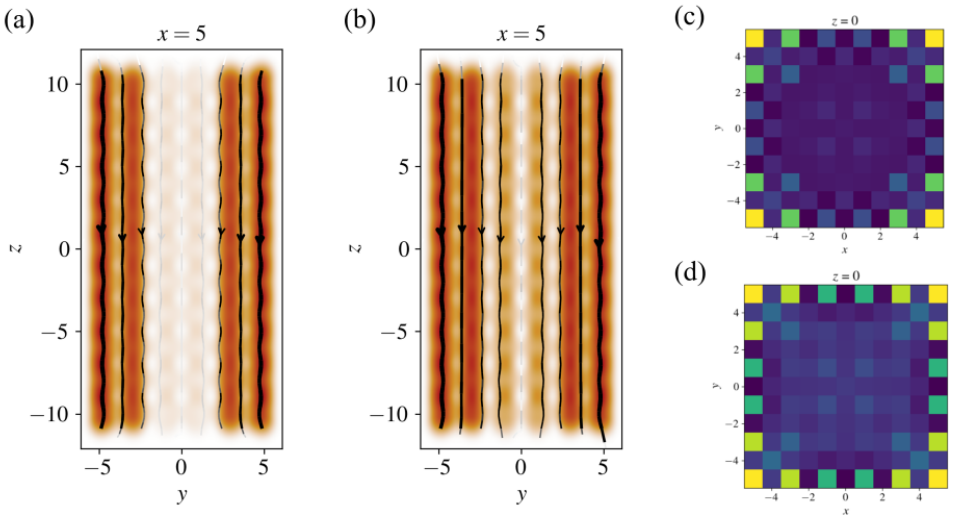

Figure 5.3: Current visualization for a (100) nanowire at $\phi = 0$. (a) Hinge state at $E = -0.040$ eV and (b) extended surface state at $E = -0.065$ eV, along a facet of the (100) nanowire. Cross-sectional current density for the hinge state (c) and extended surface state (d).

For $\phi \neq 0$, the hinge states remain robust and continue to flow along one-dimensional channels. The extended surface states begin to spiral around the nanowire under the influence of the magnetic field.

5.1.2 Nanowire (110)

The band structure of the (110) nanowire does not show any gap opening/closing when a magnetic field is applied along the nanowire's axis. This behavior can be attributed to the nature of the gapless states, which are confined to the surfaces of the individual facets and only weakly couple to each other.

Figure 5.4 (a) shows the conductance in the energy gap along the longitudinal direction for two flux values: $\phi = 0$ and $\phi = 0.3$. The conductance remains fixed at $G = 4e^2/h$, consistent with the presence of four gapless states. This indicates that no channels are opened or closed by the introduction of magnetic flux. As expected, AB oscillations are absent in the (110) nanowire when measuring conductance in the forward direction. For reference, the corresponding band structures are shown in Figure 5.4 (b) at both flux values.

Figure 5.4 (c) shows the current density of a gapless state flowing through the nanowire's cross section at $E = -0.075$ eV. The current is localized at the surfaces, consistent with the picture of confined surface states that remain gapless and unaffected by magnetic flux.

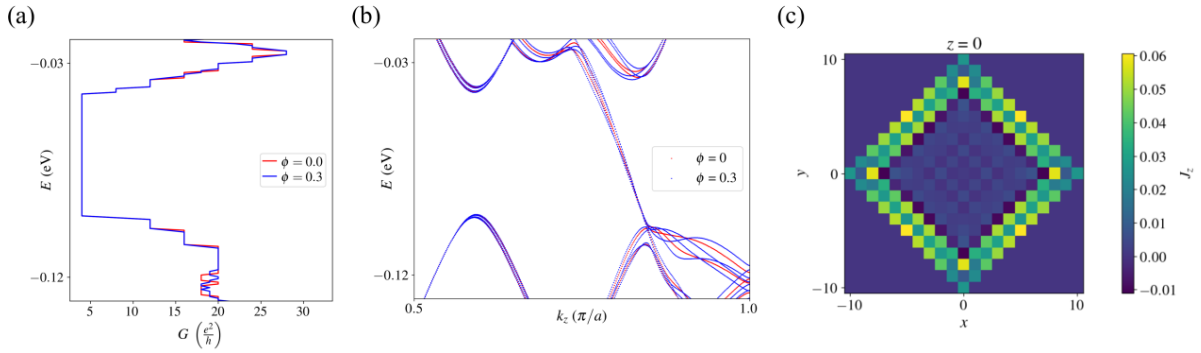

Figure 5.4: (a) Conductance of the 11×11 (110) nanowire at $\phi = 0$ and $\phi = 0.3$. (b) Corresponding band structures at the two flux values. (c) Current density plot showing surface-confined current at $E = -0.075$ eV.

5.2 Transverse

Having the different characters of the gapless states; hinge states, extended surface states and confined surface states, makes it interesting to look at transport in the transverse direction, perpendicular to the nanowire's axis. Specifically we will study the transverse transport properties for the (100) and (110) nanowires.

For computational efficiency, we restore translational invariance in the $z-$direction for both the scattering region and the leads. This introduces three momentum parameters: k_z, $k_{z,\text{lead }0}$ and $k_{z,\text{lead }1}$. Note that k_z specifies where we are in the band structure of the nanowire, we will set $k_z = k_{z,\text{lead }0} = k_{z,\text{lead }1}$. Due to the periodic boundary condition along the z-axis, we only need to do computations on the single unit cell of the transport system. Making these transverse transport simulations computationally much more efficient compared to the longitudinal transport simulations. Typically, we will look at systems of around $W \sim 50$ atoms or larger, ensuring the surface and hinge states are well resolved ($W/\xi >> 1$).
The metallic leads that are used to obtain these results are build using the 6-band Hsieh TB model, but with zero onsite and identity hopping.

5.2.1 Nanowire (100)

The (100) nanowire is known to host extended surface and hinge states in the energy gap. Since we are interested in these gapless states, we set $k_z = 0.90\ \pi/a$ (unless stated otherwise), which corresponds to the location of the Dirac cone. First we will study their transverse conductance properties. Next, we examine the response of the conductance to magnetic flux, to see if there are AB oscillations present. Finally, we calculate the total conductance by integrating over the entire BZ.

Conductance

To gain insight into transport along the transverse direction, perpendicular to the nanowire's axis, we study the conductance through a (100) slab geometry, shown in Figure 5.5 (a). The scattering region (47×47 atoms, shown in blue) is translationally invariant in the z-directions, the leads (red) are translationally invariant in the $z-$ and $x-$ directions, creating a (100) slab geometry with $N_x = 47$ layers.

Figure 5.5 (b) presents the conductance of this slab for SnTe and metallic leads. In the case of SnTe leads $G = 4$, the gapless surface states are perfectly transmitted through the scattering region without backscattering. The corresponding probability density of the scattering wavefunction ψ_{sr} (at $E = -0.1$ eV) is visualized in panel (c). The four conduction channels follow from the gapless states, present in the band structure shown in the Appendix A5.
When metallic leads are introduced, reflection occurs at the metal-SnTe interface, leading to interference effects causing an oscillatory conductance profile.

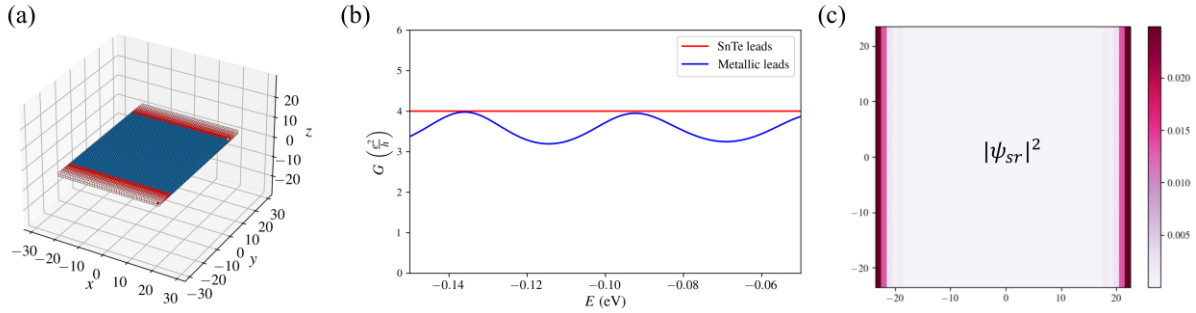

Figure 5.5: (a) Scattering region (47×47 atoms, shown in blue) translationally invariant in the z-direction and leads (red) translationally invariant in the $z-$ and $x-$ directions, resembling a (100) slab geometry. (b) Conductance through the scattering region for SnTe and metallic leads. (c) Probability density of the scattering wave function ψ_{sr}, at $E = -0.1$ eV.

Reducing the width of the leads effectively transforms the system into a (100) nanowire geometry. This minimizes the influence of the leads on the scattering states, allowing for a clearer examination of the nanowire's gapless states.
Figure 5.6 (a) illustrates a 47×47 scattering region with narrow metallic leads of width $W_{leads} = 2$. The conductance of the extended surface states for various nanowire sizes is shown in Figure 5.6 (b). The conductance curves exhibit fluctuations, as the number of scattering states varies as a function of energy at a fixed k_z. There are no sharp conductance peaks due to band broadening. Importantly, the conductance also does not decay with increasing system size. The average conductance remains approximately constant, which is characteristic for extended surface states.

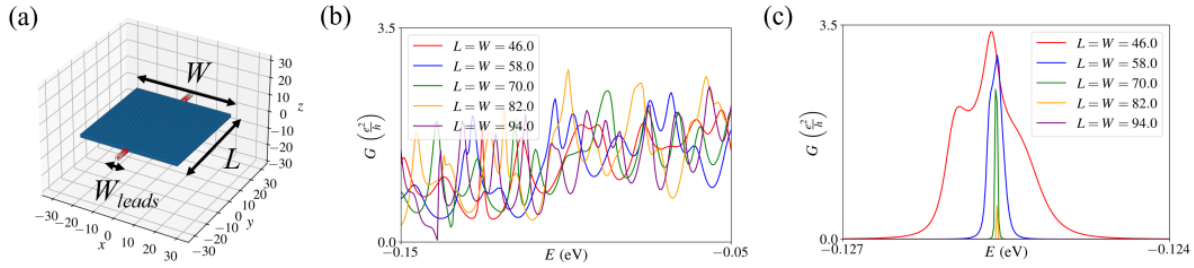

Figure 5.6: (a) Scattering region (47×47) and narrow metallic leads ($W_{\text{leads}} = 2$), effectively forming a (100) nanowire. (b) Conductance of extended surface states ($k_z = 0.90\pi/a$) as a function of nanowire size. (c) Conductance of hinge states ($k_z = \pi/a$) as a function of nanowire size.

To examine the conductance properties of the hinge state, we focus on the edge of the BZ for which $k_z = \pi/a$. Figure 5.6 (c) shows the conductance of these hinge states. Surprisingly, the hinge states contribute significantly to the transverse conductance between the leads when $L = W \lesssim 80$ atoms. However, when system size increases further, there contribution decays, consistent with the observation that hinge states are localized at the corners and decay exponentially along the nanowire's perimeter.

Flux response

To observe transport signatures such as AB oscillations, we thread the system with a magnetic flux. Since we are also interested in studying how the system size influences the strength of the flux response, we want to minimize finite-size effects. Therefore, we introduce a new gauge for the magnetic field along the nanowire's axis:

$$\begin{aligned} \mathbf{A} &= \phi\, \delta(x)\, \Theta(-y)\, \hat{x}, \\ \mathbf{B} &= \nabla \times \mathbf{A} = \phi\, \delta(x)\, \delta(y)\, \hat{z}. \end{aligned} \tag{5.2}$$

To build intuition, we begin with SnTe leads, resembling a (100) slab geometry. Figure 5.7 (a) shows the flux response for a slab with thickness $N = 15$ layers, evaluated in the middle of the energy gap at $E = -0.1$ eV. A clear AB oscillation is visible, though its amplitude is relatively small. This is expected, as the surface states at the top and bottom of the slab are exponentially decoupled, suppressing interference effects.

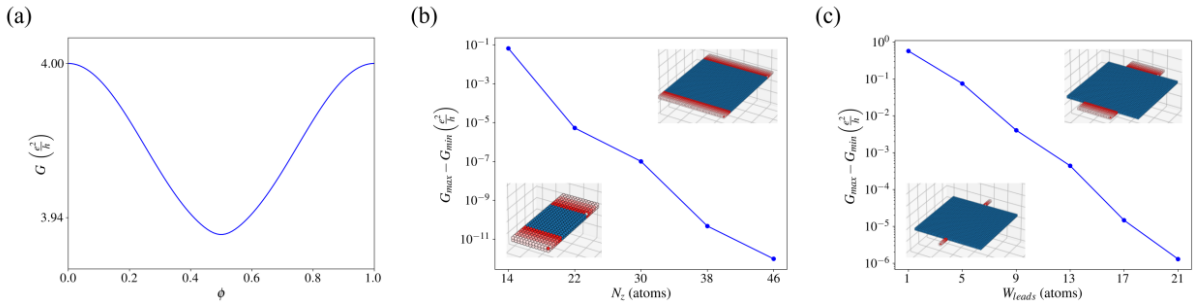

Figure 5.7: (a) Flux response obtained using SnTe leads, effectively forming a (100) slab with N = 15 layers. (b) The conductance range in the AB oscillation $G_{\max} - G_{\min}$, as a function of slab thickness N. (c) Amplitude as a function of metallic lead width W_{leads}, connected to the center of a 47×47 SnTe scattering region.

Figure 5.7 (b) plots slab thickness N against the conductance range of the AB oscillation, defined by $G_{\max} - G_{\min}$. The insets illustrate the increasing slab thickness. We observe that the AB oscillation range decreases exponentially as the slab thickness increases. This behavior is consistent with the exponential decay of the wavefunction overlap between the top and bottom surface states, as described by Eq. 2.13. When the thickness becomes sufficiently large, the surface states on opposite sides of the slab become effectively decoupled due to negligible wavefunction overlap. As a result, they can no longer coherently interfere, leading to a suppression of AB oscillations. Deviations from a perfect exponential trend arise from slight modifications in the slab's band structure as its size changes.

Next, we switch back to metallic leads and fix the nanowire size to 47×47 atoms. By decreasing the lead width W_{leads}, we examine its effect on the AB oscillation. Figure 5.7 (c) shows that narrower leads result in a stronger AB oscillation. As the lead width increases, the oscillation amplitude decreases exponentially. This makes sense because narrower leads induce more reflection, enhancing interference effects. The gapless states also meet in a narrower region, allowing them to interfere more strongly with each other.

These results were obtained at a fixed momentum $k_z = 0.90\pi/a$ and energy $E = -0.1$ eV. To assess whether these AB oscillations are observable under experimental conditions, it is necessary to integrate over the full BZ.
Figure 5.8 (a) shows the total conductance per unit length G/L, integrated over the Brillouin zone, in units of conductance quantum e^2/h per µm, for a 94×94 (100) nanowire with narrow metallic leads of width $W_{leads} = 2$, at flux $\phi = 0$ and $\phi = 0.5$. An increased conductance is visible at the top of the valence band, near $E = -0.125$ eV. On the other hand, gapless states in between the valence and conduction band, do not seem to give a clear signal. A more detailed analyses on Figure 5.8 is given in the Appendix A6.

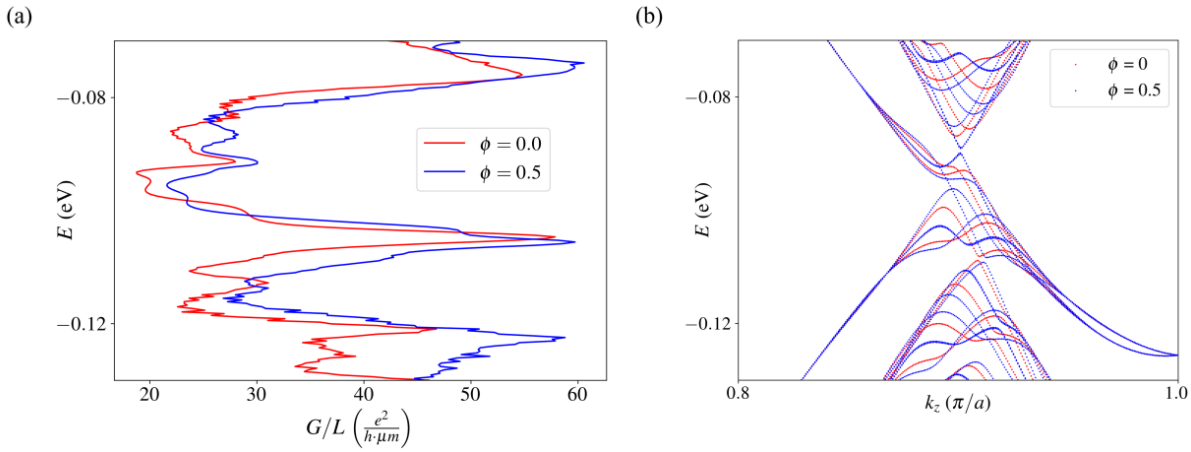

Figure 5.8: (a) Conductance per unit length G/L integrated over the Brillouin zone, for $\phi = 0$ and $\phi = 0.5$. (b) Band structure of the 94×94 (100) nanowire at $\phi = 0$ and $\phi = 0.5$.

As previously shown, increasing the lead width W_{leads} exponentially suppresses the AB oscillation. This suggests that in any realistic (100) nanowire, AB oscillations will be challenging to observe when measuring conductance in the transverse direction.

5.2.2 Nanowire (110)

The (110) nanowire is known to host confined surface states in the energy gap. Since we are interested in these gapless states, we set $k_z = 0.82\ \pi/a$ (unless stated otherwise), which corresponds to the location of the Dirac cone in the band structure. First we will study the transverse conductance properties. Next, we examine the response of the conductance to magnetic flux, to see if there are AB oscillations present. Finally, we calculate the total conductance by integrating over the entire BZ.

Conductance

Again, we begin by examining the conductance through a (110) slab geometry. The system is shown in Figure 5.9 (a), where the case of the slab corresponds to $W = W_{leads}$. Figure 5.9 (b) shows the conductance for both SnTe and metallic leads, for slab thickness $N = 28$ layers in the direction normal to the surface (meaning $W = W_{lead} = L = 54$ atoms). For SnTe leads, surface states are perfectly transmitted without any backscattering. Two channels contribute to transport, resulting in a quantized conductance of $G = 2e^2/h$, which is consistent with the band structure shown in the Appendix A5. When metallic leads are used, reflection occurs at the SnTe–metal interface. While part of the change in the conductance spectrum is due to mode mismatch, the rather sharp conductance peaks suggest a more dominant mechanism: the formation of confined surface states, separated from the leads by an effective tunnel barrier.

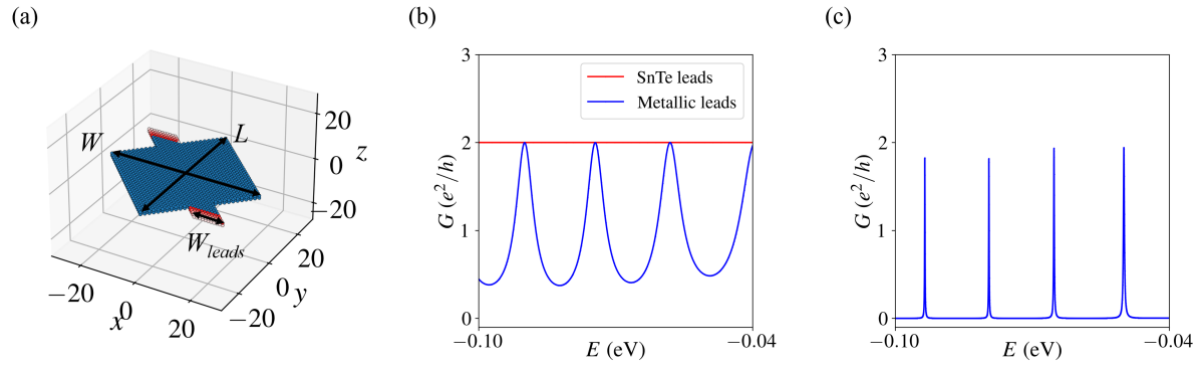

Figure 5.9: (a) Scattering region (blue) with narrow metallic leads (red). (b) Conductance through a (110) slab ($W_{leads} = W = L = 54$) for slab thickness $N = 28$ layers, examined for both SnTe and metallic leads. (c) Conductance through the (110) nanowire with metallic leads of $W_{leads} = 10$.

Deforming the slab into a (110) nanowire means reducing the metallic lead widths. Figure 5.9 (c) shows the resulting conductance for $W_{leads} = 10$ atoms. The conductance spectrum displays narrow resonance peaks arising from confined surface states localized on the nanowire's facets. The corners of the nanowire act as tunnel barriers, allowing transmission only when the energy of an incoming mode aligns with that of a confined surface state.

From this resonant $G(E)$ spectrum, we can define the level spacing ΔE as the distance between neighboring resonance peaks. It can be related to the group velocity v_g of the band structure and the length L of the nanowire by $\Delta E = v_g \cdot 2\pi/L$.
If the resonance peaks are due to confined surface states with a tunnel barrier, we would expect this ΔE relation to hold. To test this hypothesis, we examined the level spacing as a function of both nanowire length L and width W. In all these simulations the metallic lead width is fixed at $W_{leads} = 10$ atoms.

Figure 5.10 (a) plots the level spacing as a function of nanowire length, fitted with group velocity $v_g = 0.126\ \text{eV} \cdot a$, with fixed $W = 60$ atoms. The clear $1/L$ dependence confirms the expected behavior. The extracted value of v_g agrees well with the group velocity from the slab band structure shown in Appendix A5.

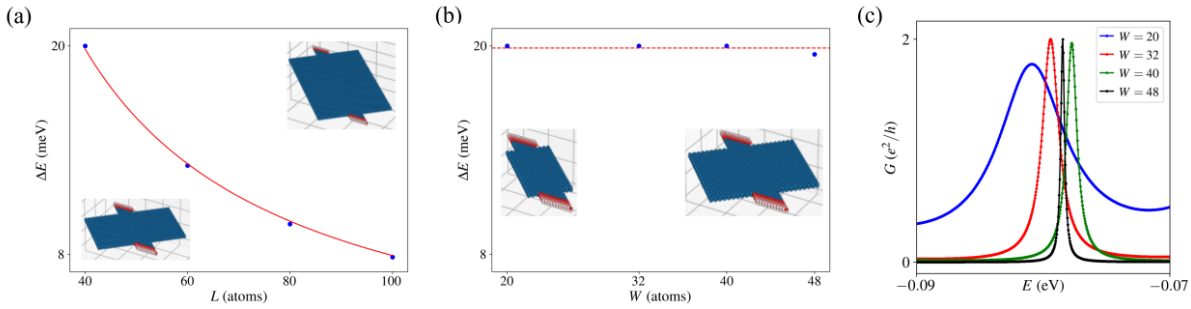

Figure 5.10: (a) Level spacing ΔE as a function of nanowire length L, fitted using $\Delta E = v_g \cdot 2\pi/L$ with $v_g = 0.126$ eV $\cdot\, a$. (b) Level spacing as a function of nanowire width W, fitted with a straight line. (c) Resonance peaks for various nanowire widths, while fixing $L = 40$ and $W_{leads} = 10$ atoms.

Figure 5.10 (b) shows the level spacing as a function of nanowire width, with fixed $L = 40$ atoms. A straight line is fitted to the data points, revealing no significant dependence on width. Figure 5.10 (c) shows the resonance peaks for nanowires of varying width. As the nanowire width decreases, the resonance peaks broaden. This behavior can be attributed to a reduction in the effective tunnel barrier at the corners of the nanowire, which increases the coupling between the confined surface states and the leads.

Flux response

The flux response of the gapless states of the (110) nanowire, for transport along the transverse directions, shows similar behavior as the (100) nanowire. AB oscillation are observed, but its amplitude decays as the lead width W_{leads} increases.

These previous results were obtained at fixed momentum $k_z = 0.82\pi/a$. To assess whether AB oscillations are observable under experimental conditions, we integrate the conductance over the full BZ using eq. 2.18. It is important to note that conductance $G(E, k_z)$ is not a smooth function, as it consists of sharp resonance peaks. Physically, this means that the integration is only meaningful for a specific longitudinal length (in the $z-$direction). For an experimentally realistic estimate, we choose a longitudinal nanowire length of 1 µm. Given the lattice constant of SnTe $a = 6.31$Å, the longitudinal length corresponds to approximately $1600a$, implying a BZ sampling of $\Delta k = 2\pi/1600$.

Figure 5.11 (a) shows the total conductance G integrated over the BZ assuming a 1 µm longitudinal length, at flux values $\phi = 0$ and $\phi = 0.5$. In the energy gap, resonant behavior remains visible. However, it is unlikely that these features would survive at finite temperature (with disorder), except potentially under cryogenic conditions.

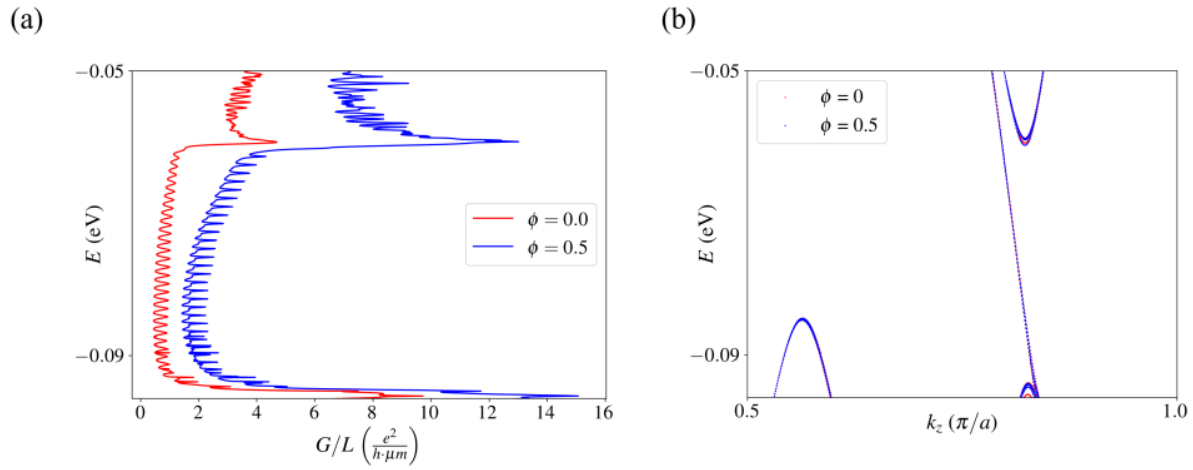

Figure 5.11: (a) Conductance obtained for a 41×41 (110) nanowire with 1 µm longitudinal length and narrow metallic leads $W_{leads} = 3$ atoms, at flux values $\phi = 0$ and $\phi = 0.5$. (b) Band structure of a 41×41 (110) nanowire.

Figure 5.11 (b) shows the band structure of the (110) nanowire around the energy gap region for reference. The average conductance trend can be attributed to the density of states near the gapped surface Dirac cone (around $k_z = 0.82\ \pi/a$). Interestingly, the avoided crossing does not give rise to enhanced conductance, likely because the corresponding surface states are too confined to the facets of the nanowire, to contribute significantly to transport. A more detailed analyses on Figure 5.11 is given in the Appendix A6.

In general, the conductance at $\phi = 0.5$ is approximately twice as large compared to the conductance at $\phi = 0$. For the (100) nanowire this was not a trend due to the band broadening. In this case, contributions from different k_z points remain distinct, producing a clear flux response. However, since increasing the width of the lead suppresses the flux response, observing such effects in an experimental setting will be challenging.

6 Conclusion

In this thesis, we have theoretically simulated SnTe using a tight-binding (TB) model approach. Bulk and slab geometries were used to validate the TB models. We confirmed the topological equivalence between the Lent model and the effective Hsieh model. This was done by studying their equivalent bulk and slab characteristics. The Hsieh TB model was used for all electronic and transport results. As this is an effective model, we noticed that the specific energy and length scales (i.e. penetration depth) do not exactly correspond to those in SnTe.

SnTe nanowires were studied in different configurations with surface terminations (100), (110) and the combination of both, the so called (101) nanowire. We established that the (100) and (110) nanowires are intrinsic higher-order topological insulators. Based on the robustness of their hinge bands to size effects (including step edges and hinge rounding), strain, flux, as well as their spin polarization and corner charge. The (101) nanowire exhibited extrinsic topological behavior.

We continued to study the quantum transport signatures of the gapless states in SnTe nanowires. In the forward direction, the (100) nanowire exhibits Aharonov-Bohm (AB) oscillations, which could be measured using gate voltage control over the chemical potential. Such AB oscillations were not observed for gapless states in the (110) nanowire.

The transverse conductance of the (100) nanowire was smooth, a signature of extended surface states. In contrast, the transverse conductance of the (110) nanowire showed sharp resonance peaks, a signature of confined surface state, where the nanowire's corners act as tunnel barriers. Measuring these resonance peaks will be experimentally challenging, as finite temperature and disorder could smear them out. For both nanowires, transport along the transverse direction showed weak AB oscillation, due to gapless states at different sides decoupling, preventing interference.

These findings demonstrate the relationship between surface terminations, the nature of gapless (surface/hinge) states and their quantum transport signatures.
Although we only investigated SnTe, we believe that these results are valid for $Pb_{1-x}Sn_xTe$ nanowires with $x > 0.38$. More generally, these findings might suggest a deeper connection between surface termination, mirror Chern numbers and the nature of gapless states in topological crystalline insulators. Specifically, the presence of confined surface states on (110) terminations (for which mirror Chern number $C_m = -2$) contrasts the extended surface states on (100) terminations (for which $C_m = 0$). Further research is needed to determine whether these patterns extend to other topological crystalline insulators. Understanding this connection is important for predicting and controlling electronic properties of topological nanostructures, which could impact future electronics.

7 Outlook

This thesis provides a foundational understanding of the electronic and transport properties of SnTe nanowires. Building on these results, several natural directions for future research emerge.

While we briefly explored geometric imperfections such as step edges and hinge rounding, real experimental systems inevitably contain additional sources of disorder, including atomic vacancies, surface roughness, and electrostatic or magnetostatic inhomogeneities. The influence of such disorder on for example the resonance peaks or the Aharonov-Bohm oscillations remains an open question. Our simulations also assumed a magnetic field aligned parallel to the nanowire axis. A logical extension would be to examine the effect of non-parallel magnetic fields.

To investigate transport through the $Pb_{1-x}Sn_xTe$ nanowires, an effective tight-binding model needs to be constructed for PbTe. One approach could be to fit the effective Hsieh model the Lent model for PbTe. The resulting fit parameters could then be used with the virtual crystal approximation to study the electronic and transport properties in $Pb_{1-x}Sn_xTe$ nanowires. Another interesting direction would be studying the transport properties of nanowire's constructed using different surface terminations, as presented in [25].

Lastly, $k \cdot p$ analysis could explain the interplay between surface terminations, mirror Chern numbers and the extended/confined nature of the surface states.
Furthermore, to quantify the topology of the nanowires, topological invariants such as the scattering invariant could be computed.

A Appendix

A1 Lent tight-binding model

The Lent tight-binding (TB) model [9] is a nearest-neighbor model that considers two atoms per unit cell. Its Hamiltonian is given by

$$\begin{aligned} H_0 = & \sum_{\vec{R},\sigma,i} \Big[|a,i,\sigma,\vec{R}\rangle E_{i,a} \langle a,i,\sigma,\vec{R}| + |c,i,\sigma,\vec{R}+\vec{d}\rangle E_{i,c} \langle c,i,\sigma,\vec{R}+\vec{d}| \Big] \\ & + \sum_{\vec{R},\vec{R}',\sigma,i,j} \Big[|a,i,\sigma,\vec{R}\rangle V_{i,j} \langle c,j,\sigma,\vec{R}'+\vec{d}| + \text{h.c.} \Big] + H_{\text{SO}} \end{aligned} \tag{A.1}$$

Here, $\vec{R}$ denotes the lattice positions of the anion (a = Te) in the rock-salt structure. Indices i and j label the orbitals for the cation (c = Sn or Pb) and anion, respectively. Telluride acts as the anion in both SnTe and PbTe due to its higher electronegativity. The spin index σ corresponds to spin-up ($\uparrow$) or spin-down ($\downarrow$) states. Vector $\vec{d}$ represents the position of the cation relative to the anion within the unit cell, which is constant: $\vec{d} = \frac{a_L}{2}(1,0,0)$, where a_L is the lattice constant.

The first line corresponds to the onsite potential, whereas the second line corresponds to the nearest-neighbor hopping with an additional spin–orbit coupling term H_{SO} defined as

$$\begin{aligned} H_{\text{SO}} = & \sum_{\vec{R},\sigma,\sigma',i} \Big[|c,i,\sigma,\vec{R}\rangle \lambda_c \, \vec{L}_c \cdot \vec{\sigma}_c \langle c,i,\sigma',\vec{R}| \Big] \\ & + \sum_{\vec{R},\sigma,\sigma',j} \Big[|a,j,\sigma,\vec{R}\rangle \lambda_a \, \vec{L}_a \cdot \vec{\sigma}_a \langle a,j,\sigma',\vec{R}| \Big] . \end{aligned} \tag{A.2}$$

The operators $\vec{L}$ and $\vec{\sigma}$ correspond to orbital angular momentum and spin (Pauli matrices), respectively. Spin–orbit coupling strengths are given by λ_c and λ_a for the cation and anion.

Table A.1 presents the TB parameters of SnTe and PbTe, in the Slater-Koster sign convention, where $V_{p,s}$ $V_{p,d}$ and $V_{p,d\pi}$ have an opposite sign (see the supplementary materials of Safaei et al. [19]) compared to the original Lent parameters, presented by Lent et al [9]. The results in this thesis were obtained using these parameters for the Lent TB model.

Symbol	SnTe (eV)	PbTe (eV)
$E_{s,c}$	-6.578	-7.612
$E_{s,a}$	-12.067	-11.002
$E_{p,c}$	1.659	3.195
$E_{p,a}$	-0.167	-0.237
$E_{d,c}$	8.38	7.73
$E_{d,a}$	7.73	7.73
λ_c	0.592	1.500
λ_a	0.564	0.428
$V_{s,s}$	-0.510	-0.474
$V_{s,p}$	0.949	0.705
$V_{p,s}$	0.198	-0.633
$V_{p,p}$	2.218	2.066
$V_{p,p\pi}$	-0.446	-0.430
$V_{p,d}$	1.11	1.29
$V_{p,d\pi}$	-0.624	-0.835
$V_{d,p}$	-1.67	-1.59
$V_{d,p\pi}$	0.766	0.531
$V_{d,d}$	-1.72	-1.35
$V_{d,d\delta}$	0.618	0.668

Table A.1: Tight-binding parameters for SnTe and PbTe in the Slater-Koster sign convention.

A2 (110) nanowire flux response

Figure A.1 shows the flux response of the (110) nanowire. As also shown by Skiff et al. [6], the low-energy states near the gap exhibit a weak response to flux, with only slight lifting and restoring of degeneracies (as seen in Fig. 4.15). In contrast, higher-energy states display a stronger flux response, as the confined surface-state character becomes less pronounced.

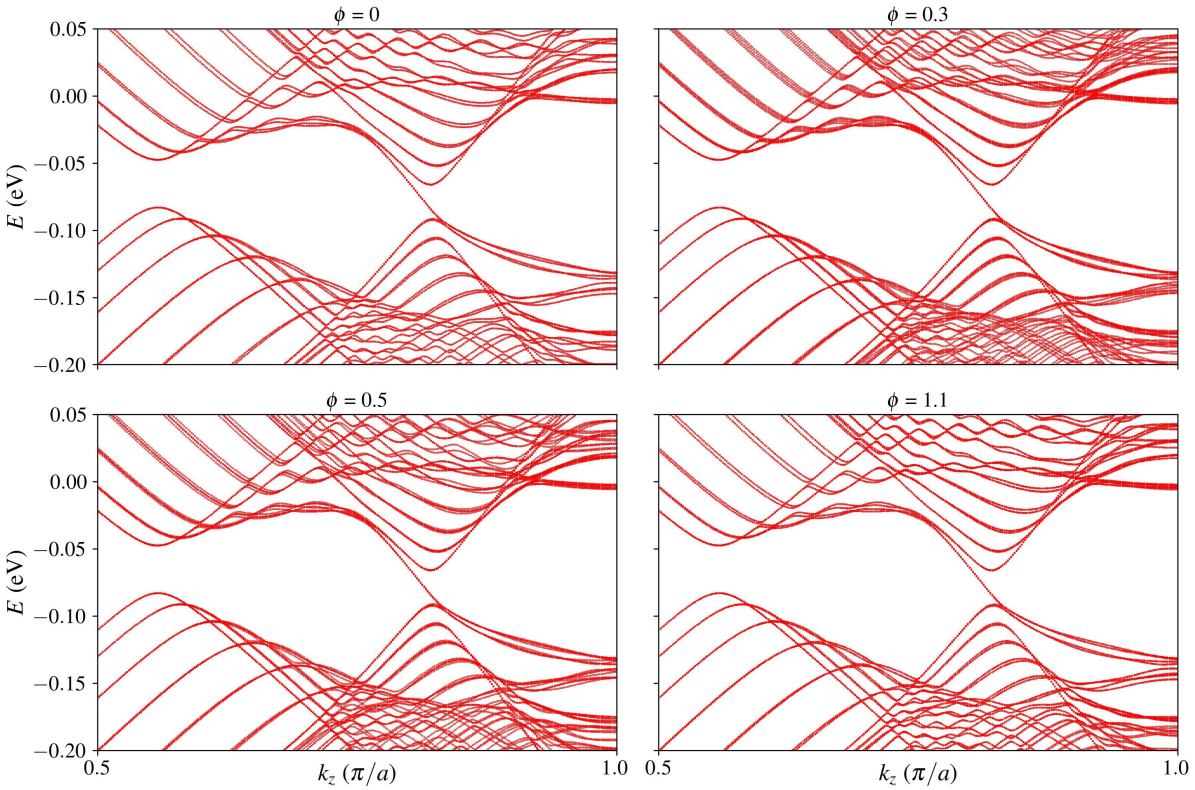

Figure A.1: Flux response around the energy gap of in a 28×28 (110) nanowire.

A3 Corner charge

Figure A.2 (a) shows the probability density summed over all states below the Fermi energy at $k_z = 0$ for a 21×21 (100) nanowire. Since these are bulk energy states, the charge distribution is uniform, with each cell carrying a charge of $Q = 6e$. This is expected as a bulk SnTe unit cell contains 12 orbitals, such that at half filling, 6 of these orbitals are occupied. At $k_z = 0$, there are 2646 occupied states ($= 21 \times 21 \times 6$), resulting in no net excess charge.

At $k_z = \pi/a$, four gapless states cross the Fermi level, increasing the total number of occupied states to 2650. The summed probability density for these states is shown in Figure A.2 (b), where some excess charge is evident. Figure A.2 (c) presents the difference between (b) and the bulk background (a), highlighting the corner charge discussed in the main text (see Fig. 4.11 (a)).

Figure A.2: (a) Probability density of all occupied bulk states at $k_z = 0$ for a 21×21 (100) nanowire. (b) Probability density at $k_z = \pi/a$ including four gapless states crossing the Fermi level. (c) Difference between plot (b) and (a), revealing the corner charge.

A similar procedure was used to compute the corner charge of the (110) nanowire, with 16×16 atoms in its outermost layer. In the full unit cell of the nanowire, there are 962 atoms. At half filling, we therefore expect 2886 occupied states ($= 962 \times 6 \times 0.5$). The summed probability density of these states at $k_z = 0$ is shown in Figure A.3 (a). As before, a uniform charge of $6e$ per cell is expected for the bulk.

The case for $k_z = \pi/a$ is shown in Figure A.3 (b), where four gapless states cross the energy gap, leading to excess charge. Subtracting the bulk background (a) from this distribution yields the corner charge shown in Figure A.3 (c), also given in the main text (Figure 4.18 (a)).

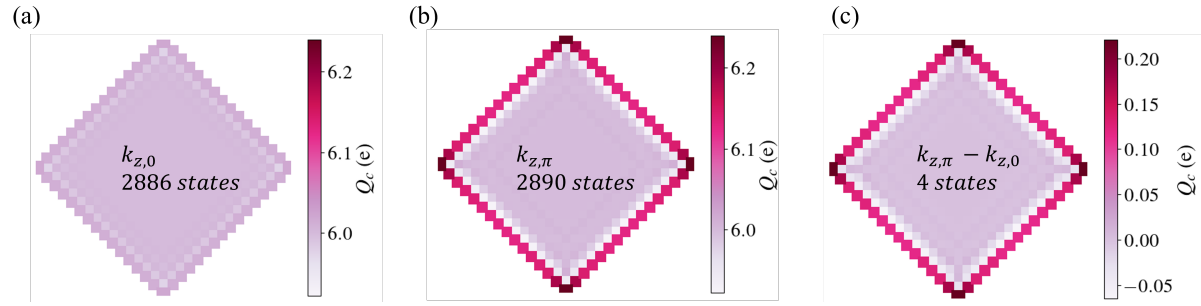

Figure A.3: (a) Probability density of all occupied bulk states at $k_z = 0$ for a 16×16 (110) nanowire. (b) Probability density at $k_z = \pi/a$ including four gapless states crossing the Fermi level. (c) Difference between plots (b) and (a), revealing the corner charge.

A4 Longitudinal Aharonov-Bohm oscillation

Figure A.4 shows the conductance of an (11×11) (100) SnTe nanowire with longitudinal SnTe leads, evaluated at $E = -0.04$ eV. For SnTe leads, modes are perfectly transmitted, resulting in discrete conductance steps. Peaks appear at flux values $\phi \approx 0.5, 1, 2, 4$, indicating a nontrivial interference pattern. This sequence suggests a strong interplay between AB phase, spin and crystalline symmetries. Why peaks emerge at $\phi = 2^n/2$ for $n \in \mathbb{Z}$ remains an open question.

When metallic leads are attached instead, perfect mode matching is lost, yet distinct interference peaks still persist in the conductance spectrum. Showing that AB oscillations are measurable at higher flux values as well.

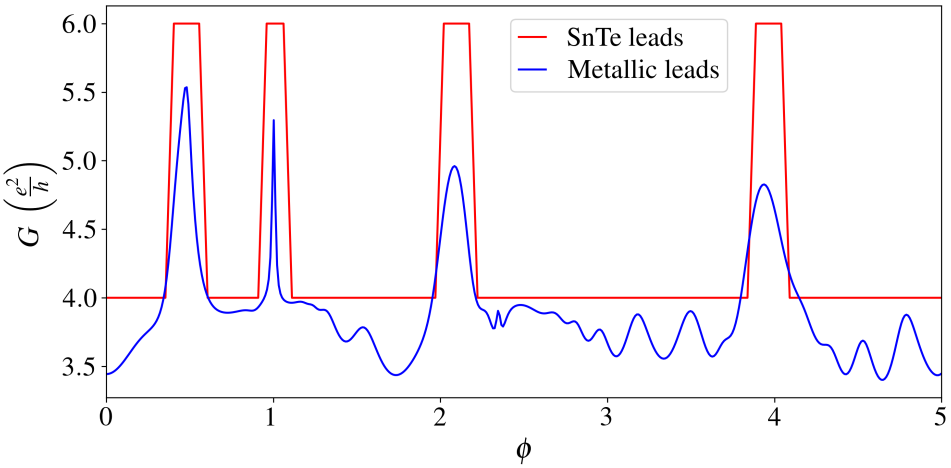

Figure A.4: Conductance at fixed energy $E = -0.04$ eV as a function of magnetic flux ϕ for an 11×11 (100) nanowire with $L = 131$ layers connected to metallic leads. The result for SnTe leads is shown for reference.

A5 Slab projections

Figure A.5 (a) shows the band structure of a (100) slab at fixed $k_z = 0.90\ \pi/a$, corresponding to the location of the Dirac cone. The bands are two-fold degenerate, resulting in four states near the Dirac point. Over the full 1D Brillouin zone ($k_y \in [-\pi/a, \pi/a]$), there are eight states in total, but only four have a positive group velocity ($v_g > 0$). Thus, we expect four forward-propagating conducting channels, consistent with the results shown in the main text (see Fig. 5.5 (b)).

Figure A.5 (b) shows the band structure of a (110) slab at fixed $k_z = 0.82\ \pi/a$, also near the Dirac point. Here, k_1 denotes momentum along the unit vector $\hat{\mathbf{e}}_1 = (\hat{\mathbf{e}}_x - \hat{\mathbf{e}}_y)/\sqrt{2}$. Due to two-fold degeneracy, there are four states across the entire 1DBZ, but only two share the same (positive) group velocity. Therefore, we observe two forward-propagating conducting channels, as discussed in the main text (see Fig. 5.9 (b)).

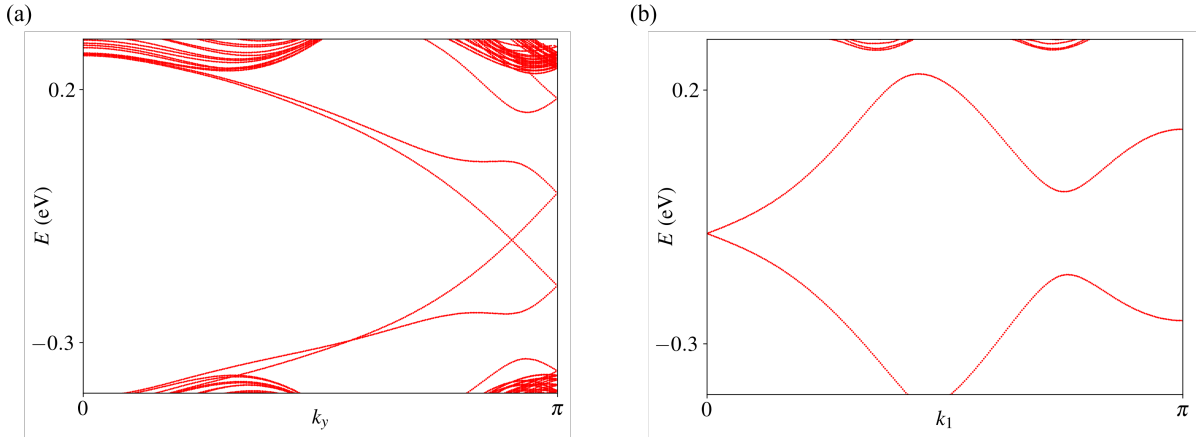

Figure A.5: (a) Band structure of the (100) slab at $k_z = 0.90\ \pi/a$. (b) Band structure of the (110) slab at $k_z = 0.82\ \pi/a$.

Fitting the level spacing relation, $\Delta E = v_g \cdot 2\pi/L$, to the data in Figure 5.10 yields a group velocity of $v_g = 0.126\ \text{eV} \cdot a$. This value is in near-perfect agreement with the group velocity obtained by fitting the Dirac cone in Figure A.5 (b) at $k_1 = 0$. This consistency supports the interpretation that the (110) nanowire corners act as tunnel barriers, hosting discretized bounded states in between them.

A6 Brillouin zone integration

This section discusses the flux response of the total transverse conductance for the (100) (Fig. 5.8) and the (110) nanowire (Fig. 5.11) in more detail, by looking at the conductance curves at each k_z value.

Nanowire (100)

Figure A.6 shows the individual conductance contributions at discrete k_z values for (a) $\phi = 0$ and (b) $\phi = 0.5$. Summing all these conductance contributions (i.e. summing over k_z) generates the the total conductance G/L, shown in the main text (Fig. 5.8 (a)). The curves appear somewhat messy because of the band broadening introduced by coupling the nanowire to leads.

As seen in Figure 5.8 (a), the most noticeable difference between the two flux values is the enhanced conductance for $-0.12 \gtrsim E \gtrsim -0.08$ eV. This change arises from subtle differences in the density of states (DOS) and the spatial character of the wavefunctions at these energies.

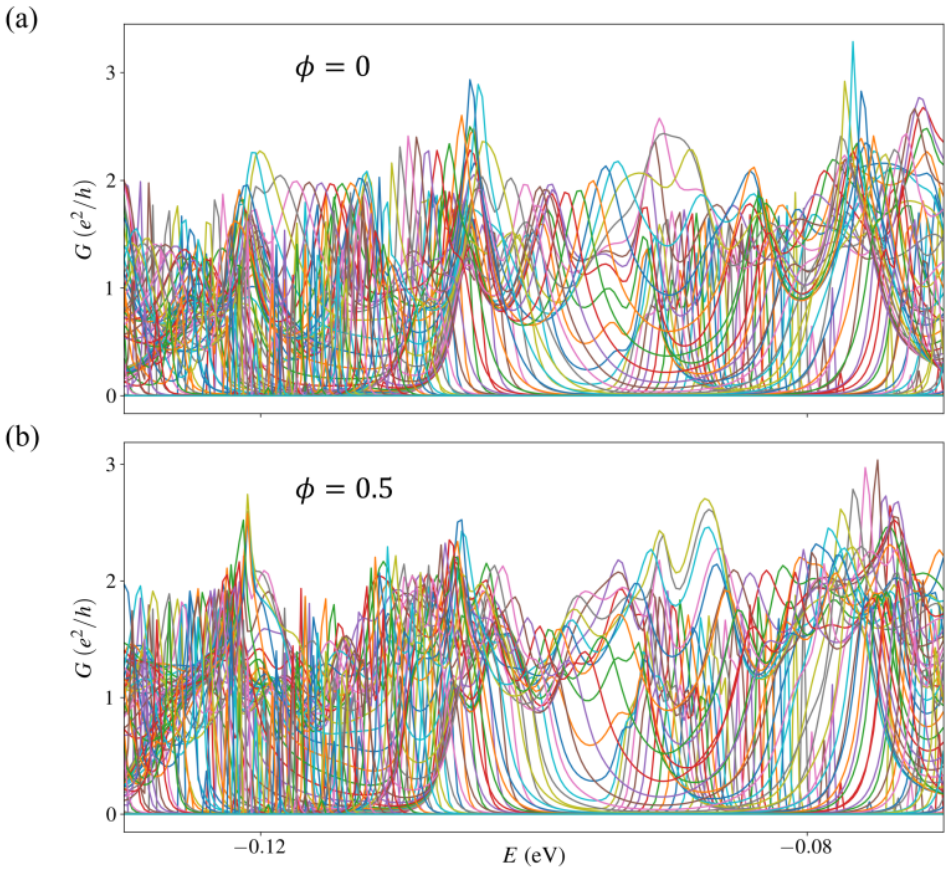

Figure A.6: Individual conductance curves at specific k_z values at (a) $\phi = 0$ and (b) $\phi = 0.5$, for transverse conduction of a (100) nanowire. Summing these curves yields the total conductance G/L, shown in Fig. 5.8 (a).

Extended surface states originating from the gapless hinge bands exhibit a slight increase in localization near the nanowire's hinges, compared to surface states associated with the gapped Dirac cone (i.e. the valence and conduction bands). The more uniform spatial distribution of the latter states appears to enable stronger coherent interference, resulting in more pronounced conductance oscillations.

Furthermore, higher harmonics were observed in the flux response, which could lead to gapless states exhibiting a reduced flux response specifically at $\phi = 0.5$. These higher harmonics stem from the wave function's spatial non-uniformity. For instance, hinge states accumulate the AB phase differently from surface states.

Nanowire (110)

First we want to highlight our choice of system size. As discussed in the main text (see Fig. 5.10 (c)), increasing the size of the scattering region ($W = L >> W_{leads}$) results in narrower resonance peaks in the conductance spectrum $G(E)$. To capture the sharpness of these peaks accurately, a dense energy sampling is needed, leading to computational limitations. On the other hand, a smaller scattering regions (($W = L \sim W_{leads}$)) broadens the peaks, causing resonant features to disappear in the energy gap. To balance peak resolution and computational limitations, we choose a scattering region of 41×41 atoms ($\sim 10 \cdot W_{leads}$).

Figure A.7 shows each individual contribution of a specific k_z value to the total conductance for $\phi = 0$ and $\phi = 0.5$. Summing all these conductance contributions (i.e. summing over k_z) generates the the total conductance G/L, shown in the main text (Fig. 5.11 (a)).

Nearly all non-zero contributions originate from the range $k_z \in [0.79\pi/a, 0.84\pi/a]$, where the gapless states are located. The shifted peaks in the energy interval $E \in [-0.09, -0.06]$ eV originate from the band connecting the valence and conduction band. For energies $E > 0.6$ eV, the density of states (DOS) increases, due to the gapped surface Dirac cone. The resonance peak height increases as well, indicating an increase in the coupling between the leads and scattering region. A clear flux response is seen for $\phi = 0.5$, indicating coherent resonant transport along the wire's perimeter.

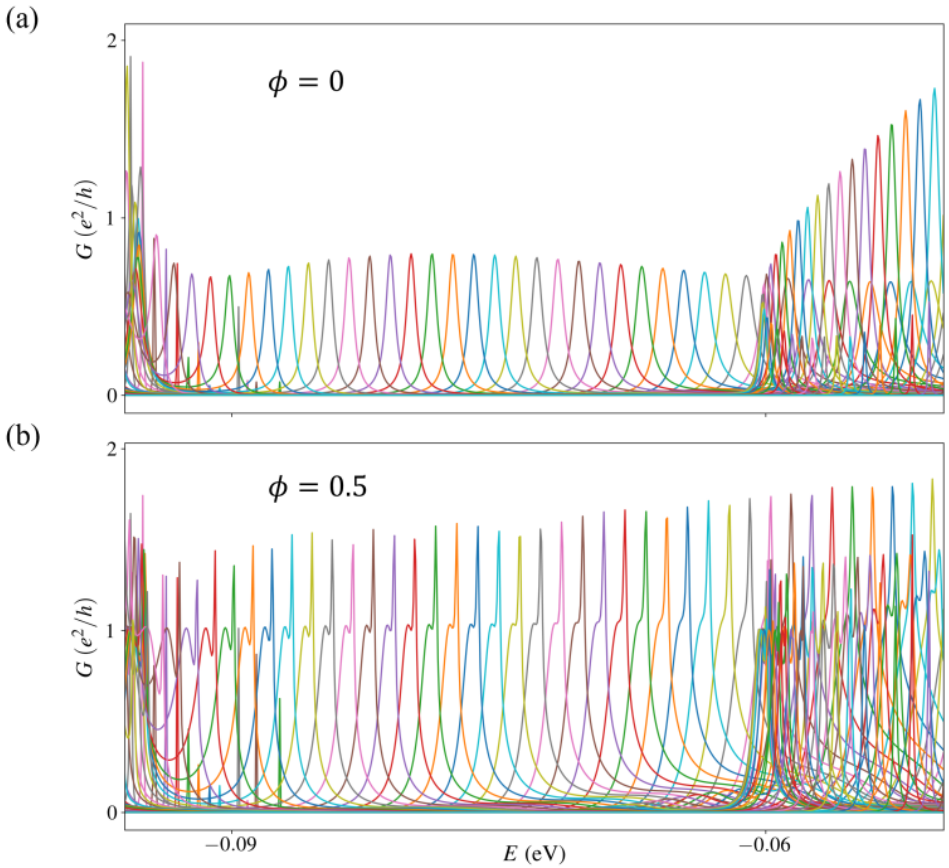

Figure A.7: Individual conductance curves at specific k_z values at $\phi = 0$ and $\phi = 0.5$, for transverse conduction of a (110) nanowire. Summing these curves generates the total conductance G/L, from Fig. 5.11 (a).

Extremely sharp peaks appear around $E \lesssim -0.09$ eV, corresponding to conductance contributions from the avoided crossing at $k_z \approx 0.55\pi/a$. The sharpness of these peaks reflect the stronger confinement of the states, compared to the gapless states. As these peaks are so sharp, our energy sampling may not fully resolve them. However, since these states belong to the valence band, they do not influence the signature of the gapless states of interest.

Bibliography

[1] Junwei Liu, Timothy H. Hsieh, Peng Wei, Wenhui Duan, Jagadeesh Moodera, and Liang Fu. Spin-filtered edge states with an electrically tunable gap in a two-dimensional topological crystalline insulator. *Nature Materials*, 13(2):178–183, February 2014. ISSN 1476-4660. doi: 10.1038/nmat3828. URL https://www.nature.com/articles/nmat3828. Publisher: Nature Publishing Group.

[2] Liang Fu. Topological Crystalline Insulators. *Physical Review Letters*, 106(10):106802, March 2011. ISSN 0031-9007, 1079-7114. doi: 10.1103/PhysRevLett.106.106802. URL https://link.aps.org/doi/10.1103/PhysRevLett.106.106802.

[3] Timothy H. Hsieh, Hsin Lin, Junwei Liu, Wenhui Duan, Arun Bansil, and Liang Fu. Topological crystalline insulators in the SnTe material class. *Nature Communications*, 3(1):982, July 2012. ISSN 2041-1723. doi: 10.1038/ncomms1969. URL https://www.nature.com/articles/ncomms1969. Publisher: Nature Publishing Group.

[4] Y. Tanaka, Zhi Ren, T. Sato, K. Nakayama, S. Souma, T. Takahashi, Kouji Segawa, and Yoichi Ando. Experimental realization of a topological crystalline insulator in SnTe. *Nature Physics*, 8 (11):800–803, November 2012. ISSN 1745-2481. doi: 10.1038/nphys2442. URL https://www.nature.com/articles/nphys2442. Publisher: Nature Publishing Group.

[5] Frank Schindler, Ashley M. Cook, Maia G. Vergniory, Zhijun Wang, Stuart S. P. Parkin, B. Andrei Bernevig, and Titus Neupert. Higher-Order Topological Insulators. *Science Advances*, 4(6): eaat0346, June 2018. ISSN 2375-2548. doi: 10.1126/sciadv.aat0346. URL http://arxiv.org/abs/1708.03636. arXiv:1708.03636 [cond-mat].

[6] Roni Majlin Skiff, Fernando De Juan, Raquel Queiroz, Subramanian Mathimalar, Haim Beidenkopf, and Roni Ilan. Confined vs. extended Dirac surface states in topological crystalline insulator nanowires. *SciPost Physics Core*, 6(1):011, March 2023. ISSN 2666-9366. doi: 10.21468/SciPostPhysCore.6.1.011. URL https://scipost.org/10.21468/SciPostPhysCore.6.1.011.

[7] Nguyen Minh Nguyen, Wojciech Brzezicki, and Timo Hyart. Corner states, hinge states and Majorana modes in SnTe nanowires. *Physical Review B*, 105(7):075310, February 2022. ISSN 2469-9950, 2469-9969. doi: 10.1103/PhysRevB.105.075310. URL http://arxiv.org/abs/2105.11489. arXiv:2105.11489 [cond-mat].

[8] I. C. Fulga, N. Avraham, H. Beidenkopf, and A. Stern. Coupled-layer description of topological crystalline insulators. *Physical Review B*, 94(12):125405, September 2016. ISSN 2469-9950, 2469-9969. doi: 10.1103/PhysRevB.94.125405. URL http://arxiv.org/abs/1605.00652. arXiv:1605.00652 [cond-mat].

[9] Craig S Lent, Marshall A Bowen, John D Dow, Robert S Allgaier, Otto F Sankey, and Eliza S Ho. Relativistic empirical tight-binding theory of the energy bands of GeTe, SnTe, PbTe, PbSe, PbS, and their alloys. *Superlattices and Microstructures*, 2(5):491–499, January 1986. ISSN 07496036. doi: 10.1016/0749-6036(86)90017-0. URL https://linkinghub.elsevier.com/retrieve/pii/0749603686900170.

[10] Yasuhiro Hatsugai. Chern number and edge states in the integer quantum Hall effect. *Physical Review Letters*, 71(22):3697–3700, November 1993. doi: 10.1103/PhysRevLett.71.3697. URL https://link.aps.org/doi/10.1103/PhysRevLett.71.3697. Publisher: American Physical Society.

[11] Yuanyang Deng. The Progress and Potential Applications of Quantum Anomalous Hall Effect. *Journal of Physics: Conference Series*, 2386(1):012058, December 2022. ISSN 1742-6596. doi: 10.1088/1742-6596/2386/1/012058. URL https://dx.doi.org/10.1088/1742-6596/2386/1/012058. Publisher: IOP Publishing.

[12] C. L. Kane and E. J. Mele. $\mathbb{Z}_2$ Topological Order and the Quantum Spin Hall Effect. *Physical Review Letters*, 95(14):146802, September 2005. doi: 10.1103/PhysRevLett.95.146802. URL https://link.aps.org/doi/10.1103/PhysRevLett.95.146802. Publisher: American Physical Society.

[13] Jeffrey C. Y. Teo, Liang Fu, and C. L. Kane. Surface states and topological invariants in three-dimensional topological insulators: Application to $Bi_{1-x}Sb_x$. *Physical Review B*, 78(4):045426, July 2008. doi: 10.1103/PhysRevB.78.045426. URL https://link.aps.org/doi/10.1103/PhysRevB.78.045426. Publisher: American Physical Society.

[14] János K. Asbóth, László Oroszlány, and András Pályi. *A Short Course on Topological Insulators: Band-structure topology and edge states in one and two dimensions*, volume 919. 2016. doi: 10.1007/978-3-319-25607-8. URL http://arxiv.org/abs/1509.02295. arXiv:1509.02295 [cond-mat].

[15] R. Jackiw and C. Rebbi. Solitons with fermion number. *Physical Review D*, 13(12):3398–3409, June 1976. doi: 10.1103/PhysRevD.13.3398. URL https://link.aps.org/doi/10.1103/PhysRevD.13.3398. Publisher: American Physical Society.

[16] Sebastian Huber and Titus Neupert. Week 8 Lecture Notes: Topological Condensed Matter Physics.

[17] Christoph W Groth, Michael Wimmer, Anton R Akhmerov, and Xavier Waintal. Kwant: a software package for quantum transport. *New Journal of Physics*, 16(6):063065, June 2014. ISSN 1367-2630. doi: 10.1088/1367-2630/16/6/063065. URL https://dx.doi.org/10.1088/1367-2630/16/6/063065. Publisher: IOP Publishing.

[18] P. R. Amestoy, I. S. Duff, J. S. Koster, and J. Y. L'Excellent. Siam. j. matrix anal. and appl. *SIAM Journal on Matrix Analysis and Applications*, 23(1):15, 2001.

[19] S Safaei, M Galicka, P Kacman, and R Buczko. Quantum spin Hall effect in IV-VI topological crystalline insulators. *New Journal of Physics*, 17(6):063041, June 2015. ISSN 1367-2630. doi: 10.1088/1367-2630/17/6/063041. URL https://dx.doi.org/10.1088/1367-2630/17/6/063041. Publisher: IOP Publishing.

[20] S. Safaei, P. Kacman, and R. Buczko. Topological crystalline insulator (Pb,Sn)Te: Surface states and their spin polarization. *Physical Review B*, 88(4):045305, July 2013. ISSN 1098-0121, 1550-235X. doi: 10.1103/PhysRevB.88.045305. URL https://link.aps.org/doi/10.1103/PhysRevB.88.045305.

[21] G. E. Volovik. Topological Lifshitz transitions. *Low Temperature Physics*, 43(1):47–55, January 2017. ISSN 1063-777X, 1090-6517. doi: 10.1063/1.4974185. URL https://pubs.aip.org/ltp/article/43/1/47/252437/Topological-Lifshitz-transitions.

[22] Junwei Liu, Wenhui Duan, and Liang Fu. Two types of surface states in topological crystalline insulators. *Physical Review B*, 88(24):241303, December 2013. ISSN 1098-0121, 1550-235X. doi: 10.1103/PhysRevB.88.241303. URL https://link.aps.org/doi/10.1103/PhysRevB.88.241303.

[23] Alexander Lau and Carmine Ortix. Topological Semimetals in the SnTe Material Class: Nodal Lines and Weyl Points. *Physical Review Letters*, 122(18):186801, May 2019. ISSN 0031-9007, 1079-7114. doi: 10.1103/PhysRevLett.122.186801. URL https://link.aps.org/doi/10.1103/PhysRevLett.122.186801.

[24] Hideyuki Ozawa, Ai Yamakage, Masatoshi Sato, and Yukio Tanaka. Finite-size-effect-induced topological phase transition in a topological crystalline insulator. *Physical Review B*, 90(4):045309, July 2014. ISSN 1098-0121, 1550-235X. doi: 10.1103/PhysRevB.90.045309. URL http://arxiv.org/abs/1403.3791. arXiv:1403.3791 [cond-mat].

[25] Sander G. Schellingerhout, Roberto Bergamaschini, Marcel A. Verheijen, Francesco Montalenti, Leo Miglio, and Erik P.A.M. Bakkers. In-Plane Nanowire Growth of Topological Crystalline Insulator $Pb_{1-x}Sn_xTe$. *Advanced Functional Materials*, 33(50):2305542, 2023. ISSN 1616-3028. doi: 10.1002/adfm.202305542. URL https://onlinelibrary.wiley.com/doi/abs/10.1002/adfm.202305542. _eprint: https://onlinelibrary.wiley.com/doi/pdf/10.1002/adfm.202305542.

[26] P. Dziawa, B. J. Kowalski, K. Dybko, R. Buczko, A. Szczerbakow, M. Szot, E. Łusakowska, T. Balasubramanian, B. M. Wojek, M. H. Berntsen, O. Tjernberg, and T. Story. Topological crystalline insulator states in $Pb_{1-x}Sn_xSe$. *Nature Materials*, 11(12):1023–1027, December 2012. ISSN 1476-4660. doi: 10.1038/nmat3449. URL https://www.nature.com/articles/nmat3449. Publisher: Nature Publishing Group.

[27] L. Bellaiche and David Vanderbilt. The virtual crystal approximation revisited: Application to dielectric and piezoelectric properties of perovskites. *Physical Review B*, 61(12):7877–7882, March 2000. ISSN 0163-1829, 1095-3795. doi: 10.1103/PhysRevB.61.7877. URL http://arxiv.org/abs/cond-mat/9908364. arXiv:cond-mat/9908364.

[28] Paolo Sessi, Domenico Di Sante, Andrzej Szczerbakow, Florian Glott, Stefan Wilfert, Henrik Schmidt, Thomas Bathon, Piotr Dziawa, Martin Greiter, Titus Neupert, Giorgio Sangiovanni, Tomasz Story, Ronny Thomale, and Matthias Bode. Robust spin-polarized midgap states at step edges of topological crystalline insulators. *Science*, 354(6317):1269–1273, December 2016. doi: 10.1126/science.aah6233. URL https://www.science.org/doi/10.1126/science.aah6233. Publisher: American Association for the Advancement of Science.

[29] Glenn Wagner, Souvik Das, Johannes Jung, Artem Odobesko, Felix Küster, Florian Keller, Jedrzej Korczak, Andrzej Szczerbakow, Tomasz Story, Stuart S. P. Parkin, Ronny Thomale, Titus Neupert, Matthias Bode, and Paolo Sessi. Interaction Effects in a 1D Flat Band at a Topological Crystalline Step Edge. *Nano Letters*, 23(7):2476–2482, April 2023. ISSN 1530-6984. doi: 10.1021/acs.nanolett.2c03794. URL https://doi.org/10.1021/acs.nanolett.2c03794. Publisher: American Chemical Society.

[30] Wojciech Brzezicki, Marcin Wysokiński, and Timo Hyart. Topological properties of multilayers and surface steps in the SnTe material class. *Physical Review B*, 100(12):121107, September 2019. ISSN 2469-9950, 2469-9969. doi: 10.1103/PhysRevB.100.121107. URL http://arxiv.org/abs/1812.02168. arXiv:1812.02168 [cond-mat].

[31] Chang-An Li, Song-Bo Zhang, Jian Li, and Björn Trauzettel. Higher-Order Fabry-Pèrot Interferometer from Topological Hinge States. *Physical Review Letters*, 127(2):026803, July 2021. doi: 10.1103/PhysRevLett.127.026803. URL https://link.aps.org/doi/10.1103/PhysRevLett.127.026803. Publisher: American Physical Society.

[32] T. X. Zhang, B. Samanta, J. Wang, A. B. Georgescu, H. A. Fertig, and S. X. Zhang. Controlled Vapor–Liquid–Solid Growth of Long and Remarkably Thin $pb_{1-x}sn_xte$ Nanowires with Strain-Tunable Ferroelectric Phase Transition. *ACS Applied Materials & Interfaces*, 16(40):54837–54846, October 2024. ISSN 1944-8244. doi: 10.1021/acsami.4c11537. URL https://doi.org/10.1021/acsami.4c11537. Publisher: American Chemical Society.